The Temperature Dependence of Thermal Conductance at Solid/Solid Interfaces

A Dissertation
Presented to
the faculty of the School of Engineering and Applied Science
University of Virginia

in partial fulfillment
of the requirements for the degree
Doctor of Philosophy (Mechanical and Aerospace Engineering)

by

Nam Q. Le
May 2015

© 2015 Nam Q. Le

Approval Sheet

This dissertation is submitted in partial fulfillment of the requirements for the degree of

Doctor of Philosophy (Mechanical and Aerospace Engineering)

Nam Q. Le

This dissertation has been read and approved by the Examining Committee:

Pamela M. Norris, Advisor

Patrick E. Hopkins, Committee Chairperson

William A. Soffa
Materials Science and Engineering

Leonid V. Zhigilei
Materials Science and Engineering

Alan J. H. McGaughey
Mechanical Engineering, Carnegie Mellon University

Accepted for the School of Engineering and Applied Science:

Dean, School of Engineering and Applied Science

Signatures on file
May 2015

Abstract

Many modern technologies are based on devices with physical features on scales of tens of nanometers. Thermal dissipation is a major challenge in these devices, and at these scales, the interfaces between materials can influence the thermal transport more than the materials themselves. Motivated by these applications, this work investigates the thermal conductance at interfaces between non-metallic, crystalline solids at high temperatures. Existing models accurately predict interfacial conductance at very low temperatures, but at room temperature and above, they can differ from experiments by an order of magnitude or more. I have performed classical molecular dynamics simulations that explicitly connect the behavior of interfacial conductance to underlying phonon transport phenomena, with a focus on the anharmonicity of atomic forces that is thought to be important at high temperature.

First, I used non-equilibrium molecular dynamics (NEMD) simulations to calculate interfacial conductance as a function of temperature in systems with different anharmonicity. The results confirm that anharmonicity is responsible for the high conductance observed in previous simulations and experiments at high temperatures. However, the temperature variation arises not only from anharmonicity at the interface itself, but also the anharmonicity far into the abutting materials. Second, I used the wave packet method to quantify the connection between anharmonicity and inelastic phonon scattering at the interface. The results are consistent with the NEMD simulations, showing that inelastic scattering at the interface is unlikely to explain the increase in conductance with temperature. Finally, I used the wavelet transform to quantify the distributions of energy among normal modes during the

NEMD simulations. To complement those results, I also used normal mode decomposition to calculate the mean free paths of the normal modes in the bulk materials as a function of temperature. Those results support the conclusion that phonon scattering in the bulk materials is responsible for the increase in conductance at high temperatures.

This work was carried out in both one-dimensional systems for simplicity of modeling and in three-dimensional systems for transferability to applications. The insight into interfacial conductance at high temperatures contributes to a long-standing discussion in the field of nanoscale thermal transport. In terms of practical applications, these results will improve the ability to predict and possibly manipulate the interfacial conductance of high-quality interfaces in devices at typical operating temperatures. The understanding of ideal interfaces also helps to lay the foundation necessary for future refinements of models for imperfect interfaces.

Acknowledgments

This is the section that I'm happiest to write.

First: it is my sincere pleasure to acknowledge Pam Norris for taking me under her wing five years ago and for providing me every step of the way with unwavering guidance, support, and trust, even before I deserved it. It boggles my mind to reflect on the tremendous resources and opportunities that she has made available to me, and I can only hope that I've earned some fraction of it.

I thank my advisory committee, all of whom have been very generous with their time and expertise: Patrick Hopkins, Leonid Zhigilei, William Soffa, and Alan McGaughey. I think each of you can identify the huge swaths of this work that I owe directly to classes and conversations I've had with you over the years.

I acknowledge my past and present colleagues in the trenches for many, many hours of company and conversation: Chris Baker, Matt Bauer, John Duda, Steven Easter, Tim English, LeighAnn Larkin, Christina Pappas, Quang Pham, Rouzbeh Rastgar, MacKenzie Redding, Chris Saltonstall, Justin Smoyer. I must also mention our honorary group members: Dom Barone, Ryan Johnson, Yong Yeong. And to all of my friends who I've made in Charlottesville during my time here, including all of you I've already mentioned, plus Game Night, Roy's Place, Clarke Court, and U. Forum. I count myself very, very lucky to have spent time working and playing with such smart, funny, conscientious, down-to-earth people. You've all kept me going.

Finally, I thank Ashleigh for being my partner in everything. I thank my brother for

being an inspiration to me to be a better person, although I don't say it. And most of all, I thank my parents. Bố and Má, you have made many hard decisions so that my road can be easy, and I will be eternally grateful.

This work has been funded by the Air Force Office of Scientific Research, and has been carried out using the computational resources managed by University of Virginia Advanced Computing Services and Engagement. In particular, I acknowledge Dr. Katherine Holcomb for her quite-unbelievable expertise and tireless support of the high performance computing work at this university.

Contents

Contents **vi**
List of Figures . . . ix
List of Tables . . . xi
List of Symbols . . . xii

1 Introduction **1**
1.1 Why thermal conductance at interfaces? . . . 1
1.2 Defining interfacial thermal conductance . . . 4
1.3 Review of the literature . . . 6
1.3.1 Early low-temperature research: 1941–1980s . . . 6
1.3.2 Extension to higher temperatures: 1980s–2000s . . . 9
1.3.3 Mechanisms for reduced conductance . . . 11
1.3.4 Mechanisms for increased conductance . . . 12
1.4 Overview of this work . . . 15

2 Theory and Methods **17**
2.1 Perspective I: Atomic coordinates . . . 17
2.1.1 Molecular dynamics . . . 19
2.2 Perspective II: Normal mode coordinates . . . 21
2.2.1 Lattice dynamics . . . 24
2.2.2 Quantization and phonons . . . 28
2.3 Bulk transport . . . 31
2.3.1 The Boltzmann transport equation . . . 32
2.3.2 Coupling of normal modes . . . 35
2.4 Interfacial transport . . . 36
2.4.1 Models for transmissivity . . . 38
2.4.2 Models for the phonon distribution . . . 41
2.5 Systems modeled in this work . . . 42

3 Effects of Anharmonicity on Thermal Conductance **46**
3.1 Non-equilibrium molecular dynamics . . . 46
3.1.1 Methodology . . . 47
3.1.2 Verification . . . 50
3.2 Results: Thermal conductance . . . 54
3.2.1 In one dimension . . . 55

3.2.2 In three dimensions 57
3.3 Discussion 57

4 Effects of Anharmonicity on Phonon Transmission 60
4.1 The wave packet method 61
4.1.1 Methodology 61
4.1.2 Verification 63
4.2 Results: Phonon transmission spectra 67
4.2.1 In one dimension 67
4.2.2 In three dimensions 71
4.3 Discussion 73

5 Effects of Anharmonicity on Phonon Distribution 76
5.1 The wavelet transform 76
5.1.1 Methodology 77
5.1.2 Verification 79
5.2 Results: Energy distributions 80
5.2.1 In one dimension 80
5.2.2 In three dimensions 82
5.3 Normal mode decomposition 82
5.3.1 Methodology 84
5.3.2 Verification 86
5.4 Results: Relaxation times 87
5.4.1 In one dimension 88
5.4.2 In three dimensions 89
5.5 Discussion 91
5.5.1 Ballistic and diffusive transport 91
5.5.2 The phonon distribution and thermal conductance 93

6 Conclusions 96
6.1 Summary of contributions 96
6.2 Future work 101

A Molecular dynamics code 103
A.1 Getting started 103
A.1.1 Getting the code 104
A.1.2 Compiling it 104
A.1.3 Testing it 105
A.2 Running your own MD simulations 105
A.2.1 Setting up the simulation 105
A.2.2 Running the simulation 107
A.2.3 Simulation output 109
A.3 A closer look 111
A.3.1 Overview 111
A.3.2 Common revisions and how to make them 111

Bibliography **113**

List of Figures

1.1 The layout of a GaN-based high-power transistor, and the temperature profile measured in a device during operation. 2
1.2 A sketch of the temperature distribution resulting from a steady heat current through an interface between two materials. 5

2.1 Phonon dispersion and density of states of the simulated Ar-like system. . . 26
2.2 Phonon dispersion in Ar from experimental measurement, lattice dynamics calculation, and molecular dynamics simulation. 45

3.1 Geometry of the domain for non-equilibrium simulations in three dimensions. 47
3.2 The steady-state temperature profile resulting from a one-dimensional NEMD simulation with Lennard-Jones forces. 51
3.3 Atomic speed distributions and densities of states during NEMD simulations in the 1D LJ system. 51
3.4 The same as Figure 3.3, but in a system with harmonic forces. 52
3.5 The thermal conductance h measured using a range of heat currents $\dot{Q}$ in 1D and 3D. 54
3.6 Steady-state temperature profiles in one-dimensional systems with (a) all LJ bonds, (b) all harmonic bonds, and (c) all harmonic bonds except a single LJ bond at the interface. 56
3.7 The thermal conductance $h(T)$ between one-dimensional Ar and heavy Ar. . 56
3.8 Steady-state temperature profiles in three-dimensional systems with (a) all LJ bonds, (b) all harmonic bonds, and (c) all harmonic bonds except a single LJ bond at the interface. 58
3.9 The thermal conductance $h(T)$ in three-dimensional Ar and heavy Ar. 58

4.1 Snapshots of atomic velocities in two wave packet simulations with all harmonic forces. 64
4.2 Transmissivity of normal modes as a function of their frequency in systems with harmonic forces throughout. 64
4.3 Reflectivity and transmissivity spectra of modes in a system with harmonic forces throughout. 66
4.4 Snapshots of atomic velocities $v(z,t)$ in wave packet simulations with LJ forces at the interface. 68

4.5 Energy reflection and transmission spectra from Ar to heavy Ar with LJ forces at the interface. (a) Reflection and (b) transmission spectra with amplitude corresponding to $T_{\mathrm{equiv}} = 2$ K, (c,d) the same with $T_{\mathrm{equiv}} = 12$ K, and (e) the total reflectivity and (f) total transmissivity at both amplitudes. 69
4.6 Same as Fig. 4.5, but from heavy Ar to Ar. 70
4.7 Atomic velocities during a simulation of wave packets in 3D systems with all harmonic forces vs. LJ bonds at the interface. 72

5.1 The energy distribution from the wavelet tranform in a system at thermal equilibrium. 79
5.2 Energy distributions calculated using the wavelet transform during 1D NEMD simulations at 2 K, 6 K, and 12 K. 81
5.3 Energy distributions calculated using the wavelet transform during 3D NEMD simulations. 83
5.4 NMD results for the system simulated by McGaughey and Landry. 87
5.5 Energy spectra in two arbitrary normal modes sampled from (a) one-dimensional LJ Ar at 8 K and (b) three-dimensional LJ Ar at 35 K. 88
5.6 Relaxation times of normal modes in one-dimensional Ar and heavy Ar. . . . 90
5.7 Mean free paths of normal modes in one-dimensional Ar and heavy Ar. . . . 90
5.8 Relaxation times of normal modes in three-dimensional Ar and heavy Ar. . . 92
5.9 Mean free paths of normal modes along the $\langle 100 \rangle$ and $\langle 111 \rangle$ directions in three-dimensional Ar and heavy Ar. 92

List of Tables

1.1 Properties of Semiconductors Used in Radio-Frequency Devices 2

2.1 Interatomic Potential Parameters Used in This Work 44
2.2 Coefficients for Zero-Pressure Lattice Parameter of LJ Argon 44

4.1 Transmissivity Values from 3D Wave Packet Simulations 73

A.1 List of keywords and their arguments for input scripts. Use them roughly in this order. 108
A.2 List of available interatomic potential styles and their arguments. 109
A.3 List of `routine`s for use in input scripts. 110

List of Symbols

Depending on context, these quantities may be reported in different units that are dimensionally equivalent to the SI units given here. In some cases, I also use the same symbol to refer to total and spectral quantities, which have different dimensions. For example, I use E^{K} to represent kinetic energy, while I use $E^{\mathrm{K}}(\omega)$ to represent a kinetic energy spectrum, which has dimensions of energy per frequency. This convention limits the number of symbols to recognize and aids physical intuition. To reduce ambiguity, then, I generally include the functional dependence of a given quantity.

Latin symbols

a	Lattice parameter	m
A	Cross-sectional area	m^{d-1}
B	Wave packet amplitude	m
d	Number of dimensions	
D	Density of states per angular frequency	$\mathrm{m}^{-d}\ \mathrm{rad}^{-1}\ \mathrm{s}$
e	Normal mode polarization	
E^{P}	Potential energy	J
E^{K}	Kinetic energy	J
f	Phonon frequency	s^{-1}
g	Atomic velocity distribution	$\mathrm{m}^{-1}\ \mathrm{s}$
G	Reciprocal lattice vector	m^{-1}

h	Thermal conductance	W $\mathrm{m}^{-(d-1)}$ K^{-1}
$\hbar$	Planck's constant divided by 2π	J s
k	Harmonic force constant	J m^{-2}
k_B	Boltzmann constant	J K
L	Length	m
m	Atomic mass	kg
n	Number (i.e., distribution) of phonons	
N	Number of atoms	
P	Pressure	N $\mathrm{m}^{-(d-1)}$
q	Angular wavenumber	m^{-1}
$\dot{Q}$	Heat current	W
r	Position	m
s	Sample standard deviation	Sample units
R	Thermal resistance	m^{d-1} K W^{-1}
t	Time	s
T	Temperature	K
u	Atomic displacement from equilibrium position	m
U	Interatomic potential function	J
v	Speed	m s^{-1}
V	Volume	m^d
w	Kinetic energy signal, $w = \sqrt{mv^2/2}$	$\mathrm{J}^{1/2}$
x, y, z	Cartesian coordinate axes	

Greek symbols

α	Phonon energy transmission ratio	
Γ	Phonon relaxation rate or linewidth	Hz

ϵ	Energy scale of Lennard-Jones potential	J
η	Wave packet width	m
θ	Zenith or incidence angle	rad
κ	Thermal conductivity	W $\mathrm{m}^{-(d-2)}$ K^{-1}
Λ	Phonon mean free path	m
ν	Normal mode polarization index	
ξ	Normal mode displacement	rad
ρ	Mass density	kg m^{-d}
σ	Length scale of Lennard-Jones potential	m
τ	Phonon relaxation time	s
ϕ	Azimuthal angle	rad
ψ	Morlet wavelet function	Coordinate-dependent
Ψ	Quantum mechanical wave function	Coordinate-dependent
ω	Phonon angular frequency	rad s^{-1}

Subscripts

α	Coordinate axis index (x,y,z)
B–E	Bose–Einstein
D	Debye
eq	Equilibrium
$i, j, k,$ l, m, n	Integer indices

Chapter 1

Introduction

> The ideas of the most well-informed philosophers are as yet uncertain regarding the exact nature of the motion of heat; but the great point, at present, is to regard it as motion of some kind, leaving its more precise character to be dealt with in future investigations.
>
> — John Tyndall, *Heat: A Mode of Motion*, 1868 [1]

Let us introduce heat transfer at solid/solid interfaces by seeing the problem in a real technology: GaN-based transistors. GaN-based devices are attractive for applications that demand high power at high frequencies, such as base stations for cellular telephone networks and military radar [2, 3]. In this application, engineers seek materials with a wide bandgap and a high electron mobility, both of which GaN exhibits. Table 1.1 lists the relevant properties of GaN along with those of Si and SiC for comparison. Unfortunately, despite its desirable electronic properties, GaN has a low thermal conductivity, so thermal dissipation is a challenge. In fact, prevailing designs of GaN-based devices require the use of a SiC substrate, despite its higher cost than Si, because of its higher thermal conductivity [3].

1.1 Why thermal conductance at interfaces?

Figure 1.1a shows a typical structure of an AlGaN/GaN transistor. During normal device operation, moving electrons lose their kinetic energy into the atomic lattice, dissipating

Table 1.1: Properties of Semiconductors Used in Radio-Frequency Devices [3]

Material	Bandgap (eV)	Mobility ($\mathrm{cm^2\,V^{-1}\,s^{-1}}$)	Thermal conductivity ($\mathrm{W\,m^{-1}\,K^{-1}}$)
Si	1.1	1350	150
4H-SiC	3.3	700	330–450
GaN	3.4	1200–2000	130

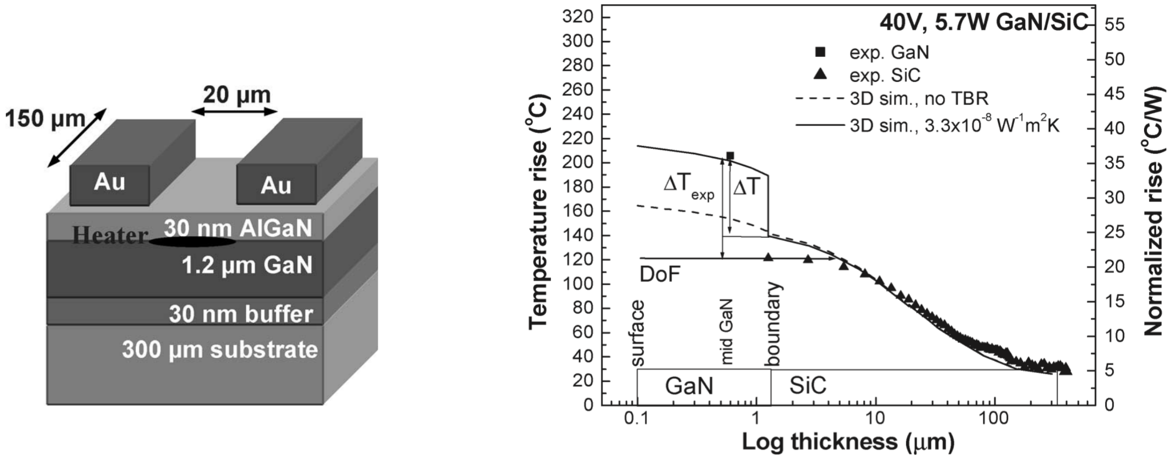

(a) (b)

Figure 1.1: (a) The layout of a GaN-based high-power transistor, and (b) the temperature profile measured in a device during operation. Reproduced with permission from Ref. [4], © 2007 IEEE.

thermal energy in the region labeled “Heater.” The thermal energy then diffuses downward through the structure to the heat sink (not shown) on the far side of the substrate. As it travels this path, the dissipated thermal energy encounters various resistances that determine the temperature rise in the device.

Sarua *et al.* [4] used Raman thermography to measure the temperature profiles during live operation of three such transistors, one of which is shown on the right side of Fig. 1.1b. The peak temperature in the device occurs in the active region, roughly 210 °C above the ambient (room) temperature. Of that temperature rise, 30–40% is due to the resistance of the GaN/SiC interface, 40–50% is due to the SiC substrate, and the rest made up by the heat sink. From the perspective of a thermal engineer, the 30 nm interface is nearly as problematic as the entire 300 μm substrate. To make matters worse, the GaN/SiC interface resistance can vary wildly, indicating that it is extremely sensitive to interface quality. In a nearly identical device, Kuzmík *et al.* [5] measured a GaN/SiC interface resistance roughly *four times* larger than measured by Sarua *et al.*, and they determined that it was responsible for 65% of the temperature rise in their device. Decreasing the interface resistance would therefore allow operation at significantly higher power and lower temperature, meaning greater performance and longer time to failure.

How could one reduce the GaN/SiC interface resistance? To answer this question requires an understanding of the causes of that resistance. Since both materials are non-metallic, thermal energy propagates through them via the vibrational motion of their constituent atoms. Thus, the cause for thermal resistance is conceptually simple: any interruption to the "ideal" propagation of vibrational motion of these atoms. Such interruptions occur both at interfaces and in the bulk materials themselves. At the GaN/SiC interface, the propagation of atomic vibrations is interrupted by the abrupt change of material properties, analogous to an electromagnetic wave encountering a change in refractive index. Other phenomena can cause interruptions as well: impurities, dislocations, strain, and even the passing motion of other propagating vibrations. Unfortunately, researchers have only attained a qualitative understanding of the effects of these mechanisms at interfaces. It has therefore proven extremely difficult to measure their relative importance in even a single material system, let alone to formulate a theory applicable to interfaces in general.

This problem motivates the work presented in this dissertation, and it appears in many technologies besides GaN-based transistors. In some technologies, better thermal dissipation leads to increased performance, in which case interface resistances are detrimental: examples include microprocessors [6] and semiconductor lasers [7], in addition to the high-power devices already discussed. Other technologies have better performance when heat flow is confined, in which case engineers can use interfacial resistance as a useful feature: these include thermoelectrics [8] and phase change memory [9]. Still other technologies contain both kinds of problems: in heat-assisted magnetic recording, for example, engineers need to increase thermal dissipation from the near-field optical transducer, and they need to confine thermal dissipation laterally in the recording medium [10]. To maximize the usefulness of the present work, in the next section I frame this problem of heat transfer at interfaces in a general way.

1.2 Defining interfacial thermal conductance

Consider heat flowing between two solid materials in contact: a steady heat current $\dot{Q}$ (in W), perhaps from Joule heating or a laser interaction, across a cross-sectional area A (in m^2) causes the system to develop a non-uniform temperature profile $T(x, y, z)$ (in K). In bulk materials, the temperature profile is often found to fall linearly with distance, which enables the definition of a constant thermal conductivity in Fourier's empirical law: $\dot{Q}/A = -\kappa \nabla T$. At interfaces, the temperature profile may exhibit an abrupt discontinuity ΔT, which leads to an analogous definition of the thermal conductance, h, at the interface: $\dot{Q}/A = h \Delta T$. In this work, for ease of comparison, values of h in 3D systems will generally be reported in units of $\mathrm{MW\,m^{-2}\,K^{-1}}$. The relationships between these various quantities are sketched in Fig. 1.2. In this work, I will primarily refer to interfacial conductance, but occasionally I find it more clear to discuss interfacial resistance, which is simply its inverse: $R = h^{-1}$. Both quantities are used pervasively in the literature.

In macroscopic systems, a temperature drop often appears due to imperfect contact between the two surfaces. In other words, the true contact area between the two solids is much smaller than the apparent contact area, reducing the interatomic interactions by which heat can conduct directly. As interface quality improves, this *contact* conductance increases. However, the conductance does not increase indefinitely: even materials in "perfect" contact retain a large, but finite, thermal conductance between them. The present work investigates the thermal conductance between materials in perfect contact only. All of the technologies mentioned in Section 1.1 feature these types of interfaces.

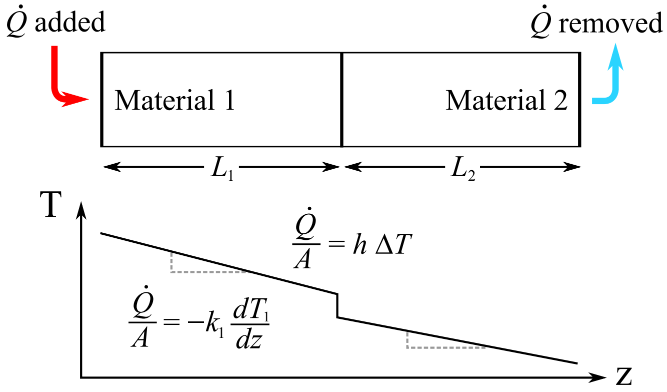

Figure 1.2: A sketch of the temperature distribution resulting from a steady heat current through an interface between two materials. The thermal conductance, h, is the amount of heat flux that can dissipate through an interface per degree of temperature difference.

In many applications, the distances L between interfaces are long, and the temperature drops at interfaces are negligible compared to those in the bulk materials. In those cases, attention should be focused on engineering the thermal properties of the bulk materials. However, in many modern devices, the distances between interfaces can be extremely short (tens of nm), and interfacial conductances become the dominant bottleneck. This can be seen in Fig. 1.2, where shrinking the lengths L_1 and L_2 would increase the relative importance of the temperature drop ΔT at the interface compared to the bulk materials. For context, a carefully-grown aluminum/silicon interface has a conductance of roughly 350 $\mathrm{MW\,m^{-2}\,K^{-1}}$at room temperature [11]. This is the same as the conductance of a thin film of silicon dioxide roughly 10 nm thick [12]. Such a conductance is too large to present a bottleneck in a macroscopic system, but it has a tremendous effect in nanoscale devices. For example, the semiconductor industry is currently manufacturing devices with features at a half-pitch of 14 nm. At these scales, a resistance equivalent to 10 nm of SiO_2 cannot be ignored. Unfortunately, despite over seventy years of research, our understanding of thermal transport at interfaces remains mostly qualitative.

1.3 Review of the literature

The first suggestion that thermal conductance can be finite even between materials in perfect contact came from P. L. Kapitza's experiments in 1941 with superfluid helium and copper [13]. For scale, he measured conductances on the order of $h \sim 10^{-3}$ $\mathrm{MW\,m^{-2}\,K^{-1}}$. The "Kapitza conductance" came to refer to the conductance between liquid helium and a solid. Researchers soon realized, though, that a finite thermal conductance occurs at interfaces between solids as well, with the same underlying physical mechanism. Therefore, researchers use the name *Kapitza conductance* in discussions of both solid/liquid and solid/solid interfaces. Other common names are *thermal boundary conductance* and *interfacial thermal conductance*. In this work, I choose the latter name because (1) the name "Kapitza" lacks physical description and (2) the term "boundary" is also used in the context of apparent thermal resistance due to size effects (as in "boundary scattering").

At room temperature, h at solid/solid interfaces is found empirically to be roughly 10^1–10^3 $\mathrm{MW\,m^{-2}\,K^{-1}}$ if at least one of the materials is non-metallic [12].[1] In this section, I survey the experimental, theoretical, and computational investigations of phonon-mediated thermal conductance from Kapitza's work to the present. The discussion here is largely qualitative; Chapter 2 contains a more quantitative discussion.

1.3.1 Early low-temperature research: 1941–1980s

The research immediately following Kapitza's observations remained focused on the conductance between a solid and liquid He, but it formed the basis for later investigations of the conductance between solids. Researchers developed several theories to explain Kapitza's observations, some explaining the resistance as a consequence of the unique properties of liquid He. However, Khalatnikov suggested a more general explanation in 1952, known now as the "acoustic mismatch model" (AMM): that the heat is primarily carried by acoustic waves

---

[1] The conductance between metals is significantly higher: 10^3–10^4 $\mathrm{MW\,m^{-2}\,K^{-1}}$. The understanding of metal/metal conductance falls outside the scope of this work.

(i.e., long-wavelength phonons), whose specular refraction at the metal/liquid He interface explains the thermal resistance [14]. Experiments vindicated the AMM, at least at extremely low temperatures (below $\sim 10^{-1}$ K). At higher temperatures, however, the data diverged from the model, generally exceeding it by an order of magnitude when temperature increases to just $T \sim 2\,\mathrm{K}$ [15, 16].

The interest in phonon scattering at solid/solid interfaces followed gradually, and at first only as a byproduct of low-temperature research on superfluidity and superconductivity. For example, in the 1950s, Hulm [17] and Goodman [18] reported significant thermal resistance due to phonon scattering at solid/solid boundaries while comparing the thermal conductivities of metals in superconducting and normal states. In 1959, Little adapted Khalatnikov's AMM for solid/liquid He conductance to apply to solid/solid conductance [19]. To my knowledge, the first direct experimental test of the AMM between solids was reported by Neeper and Dillinger [20] in 1964. They measured conductances at In/sapphire interfaces at $T = 1.1$ to 2.1 K in agreement with the theory, at least within the considerable uncertainty arising from the sound speeds in indium. Focused research on solid/solid conductance began in the 1970s, still remaining at low temperatures. Folinsbee and Anderson showed that the "excess" conductance beyond the AMM at metal/liquid He interfaces also occurs at metal/*solid*-He interfaces [21]. Anderson and coworkers also measured the thermal conductance between Mylar and various metals at $T = 0.04$ to 1.0 K [22–24], which also significantly exceeded the AMM, suggesting that the "Kapitza anomaly" is not unique to interfaces involving either liquid or solid helium.

In addition to the experimental and theoretical work to this point, a report by Lumpkin *et al.* [25] in 1978 was, to my knowledge, the first use of molecular dynamics (MD) simulation to calculate thermal conductance at an interface. They simulated a one-dimensional chain of atoms with harmonic forces, using the non-equilibrium method described in Chapter 3. In keeping with the research interests of the time, the simulations were conducted at $T \approx 2\,\mathrm{K}$. Due to computational constraints, they simulated chains of only 30 atoms. The calculated values of h agreed only within an order of magnitude with the AMM (in the classical limit) and with a flux-corrected model following a suggestion by Simons [26]. In retrospect, I believe that the discrepancy arises largely from artifacts of the non-equilibrium simulation method, as discussed in Section 5.5, which are pronounced at low T and small system sizes. The authors also observed that the simulated conductances were much smaller than experimental measurements. They hypothesized that anharmonicity was responsible, and they showed results of preliminary simulations in which anharmonicity did increase the simulated conductance. However, the magnitude of the increase was too small to agree with experiments. A decade later, in 1989, Ge *et al.* reported similar results in MD simulations of 100-atom chains [27].

Given the success of the AMM up to $T \sim 10^{-1}\,\mathrm{K}$, researchers sought corrections to the model that would improve its accuracy at higher temperatures as well. In retrospect, I classify the suggested corrections into three different categories, each incorporating a different type of physical phenomenon:

1. that the transmission coefficient should account for phonon "attenuation"—i.e., thermalization by scattering—in some small region in the bulk materials near the interface, especially by electrons [22, 23];

2. that the distribution of phonons should account for the non-equilibrium induced by a heat current, as a correction to the usual assumption of an equilibrium (Bose–Einstein) distribution [26]; and

3. that the transmission coefficient should account for inelastic phonon transmission (i.e., processes not preserving frequency) enabled by anharmonicity of atomic forces [28, 29].

Among these, the first correction seems most widely accepted, and it satisfactorily explained the "Kapitza anomaly" at temperatures up to 1–2 K, which sufficed for the low-temperature physics applications that motivated the research at the time. The second correction was accepted as an alternate framing of the same physical situation; Katerberg *et al.* [30] showed that the choice between Little's or Simons' model should depend on how temperature is sampled from the phonon population in a given experiment. Finally, the third correction seemed to explain anomalous transmission in experiments with monochromatic phonon sources [31, 32], but it was not shown to quantitatively explain the anomalous conductance under a thermal phonon source. Remarkably, although these three mechanisms were suggested to correct the AMM to describe low temperatures, they are quite similar to corrections that have been suggested for its successor at high temperatures: the diffuse mismatch model.

1.3.2 Extension to higher temperatures: 1980s–2000s

By the late 1980s, the microelectronics industry had managed to shrink feature sizes to roughly 1 μm [33], motivating exploratory research into solid/solid thermal conductance at the operating temperatures of integrated circuits—hundreds of K, compared to previous research at $< 2\,\mathrm{K}$.

The transition to higher temperatures began in earnest with two seminal papers in terms of both experimentation and theory by Swartz and Pohl. In 1987 [34], they reported measurements of $h(T)$ over $T = 1$ to 300 K at the interface between a $\mathrm{Rh}_{99.5}\mathrm{Fe}_{0.05}$ wire "thermometer" and a sapphire substrate, including a thin oxide (SiO_2) interlayer. The measured values of $h(T)$ agreed with the AMM at temperatures up to tens of K. However, upon reaching room temperature, they measured $h \sim 100\ \mathrm{MW\,m^{-2}\,K^{-1}}$, which is several times smaller than the AMM prediction. They reasoned that, at high temperatures, thermal energy propagated in shorter-wavelength modes (see Section 2.2.2) that scatter diffusely, not specularly as assumed in the AMM. They therefore proposed the *diffuse mismatch model* (DMM) in which phonons scatter completely diffusely. However, the measurements were still much lower than the DMM prediction, and they attributed the low measured values to the intermediate oxide layer. The actual details of the DMM are given in their extensive 1989 review article [35], which presents it alongside the AMM and compares the models in a thorough account of the research into both solid/liquid He and solid/solid conductance.

Around the same time, Maris and coworkers also developed both theoretical and experimental methods to investigate conductance at higher temperatures. In terms of theory, previous models had generally used the Debye model (see Section 2.2.1), which accurately describes only very low-frequency phonons and therefore is a poor approximation at higher temperatures (see Section 2.2.2). Therefore, in 1989, Young and Maris [36] proposed a numerical method of calculating $h(T)$ using harmonic lattice dynamics calculations of an interface between two atomic lattices. Their calculations are conceptually akin to the AMM in their assumption that phonons transmit specularly at the interface. However, unlike previous calculations using the AMM, their calculations account for full phonon dispersion and account exactly for the refraction and mode conversion of vibrational waves between three-dimensional, discrete atomic lattices. In the following year, Pettersson and Mahan extended the model to apply to materials with different lattices [37].

To provide experimental comparison, Stoner and Maris [38, 39] developed an optical pump–probe technique to measure $h(T)$ of several interfaces. They selected interfaces to span a wider range of vibrational mismatch than previously measured, from Ti/sapphire to Pb/diamond—i.e., in terms of ratios of Debye temperature T_{D}, from ~ 2.4 to 22.0 [40]. The measured conductances ranged from $h \sim 30$ to 200 $\mathrm{MW\,m^{-2}\,K^{-1}}$ at room temperature. Their primary observation was that, for the well-matched interfaces, their AMM-like "lattice dynamical" calculations predict the experimental data relatively well, within a factor of 2 or better. However, for the poorly-matched interfaces, the measurements are vastly greater than the prediction. In the most severe case of the Pb/diamond interface, they measured a conductance value of $h \sim 30$ $\mathrm{MW\,m^{-2}\,K^{-1}}$ at room temperature, which was 10 times higher than the DMM prediction of $h \sim 2$ $\mathrm{MW\,m^{-2}\,K^{-1}}$ and 100 times higher than their specular model's prediction of $h \sim 0.35\,\mathrm{MW\,m^{-2}\,K^{-1}}$.

In the two decades since the reports by Swartz and Pohl and by Stoner and Maris, further experimental results have generally supported their findings. Even with necessary corrections for phonon dispersion [41, 42], the AMM and the DMM variously under- and over-predict experimental measurements at room temperature by an order of magnitude or more. Some researchers [43, 44] have argued that the assumptions of completely diffuse and completely specular scattering are unrealistic, and they have used a specularity parameter to "interpolate" between the AMM and DMM. Unfortunately, many of the experimental measurements lie outside of the range bounded by the two models, implying that other effects must also be important. The lack of consistency also suggests that more than one mechanism is responsible for the scatter in experimental data. In the following two sections, I discuss separately the prevailing models for mechanisms that may reduce (Section 1.3.3) or increase (Section 1.3.4) the conductance at a given interface.

1.3.3 Mechanisms for reduced conductance

A survey of the experimental literature shows that most measured values of thermal conductance are lower than the DMM would predict for the interface: see Refs. [4, 5, 34, 45–58]. Current consensus is that these low conductances are caused by various non-idealities at the interface, such as roughness, impurities, dislocations, and so on. Since these features are spatially localized, they selectively scatter high-frequency phonons, which explains why the AMM is accurate at low temperature where those modes are not yet occupied (see Section 2.2.2). Prasher and Phelan [59] suggested accounting for these non-idealities by modifying the AMM to include phonon attenuation at the interface, which they applied to explain the low conductances measured in Refs. [34] and [45]. Hopkins and coworkers have also modified the DMM to include a similar attenuation effect, which they used successfully to model the reduction in thermal conductance due to dislocations at semicoherent interfaces [55] and due to controlled geometric roughening without interdiffusion of the materials [56, 57]. To model interfaces with significant interdiffusion, Beechem *et al.* [60, 61] modified the DMM to include scattering in a virtual crystal of equivalent thickness to the interdiffused region, which drastically improved the predicted conductance at Al/Cr interfaces [51, 54].

Although these models for reduced conductance have been relatively successful, there is still reason to be uncertain in their predictive power, since their underlying assumptions have yet to be carefully tested. Given the difficulty of testing the phonon scattering models experimentally, there have been several efforts to test them in MD simulations. For example, a series of investigations has tested the connection between conductance and phonon scattering at high-energy grain boundaries in silicon [62–64]. They showed that (1) the measured phonon transmissivities do qualitatively depend on the interfacial disorder as presumed by the phenomenological models, but that (2) even with knowledge of the precisely correct transmissivities, the prevailing model for conductance predicts a value that differs from the "computational measurement" by 50%. Other MD simulations appear to contradict the presumptions of the models outright. For example, Zhou *et al.* [65] and Merabia *et al.* [66] both reported that, as the geometric roughness of their simulated interfaces increased, the conductance actually increased, which they attributed to the greater surface area between the two materials. In order to obtain a conductance model with predictive power in thermal engineering applications, these questions must be resolved.

1.3.4 Mechanisms for increased conductance

On the other hand, there are relatively few measurements of conductance that exceed the DMM [38, 39, 50, 67, 68]. However, despite uncommon observation, this phenomenon has drawn as much theoretical attention as the cases of decreased conductance. In 2006, Lyeo and Cahill corroborated the findings of Stoner and Maris at highly mismatched Pb/diamond and Bi/diamond interfaces [67], albeit observing a stronger increasing trend in $h(T)$. Very recently, Hohensee *et al.* [68] have investigated this excess conductance as a function of pressure at several other metal/diamond interfaces, corroborating the findings for Pb/diamond and finding an even larger excess for Pt/diamond. Empirically, interfaces that exhibit conductance higher than the models have been highly vibrationally mismatched, with ratios of Debye temperatures greater than five. However, Duda and Hopkins [57] have pointed out an exception: the measurement by Minnich *et al.* [11] of an Al/Si interface that had been prepared carefully to remove the usual oxide layer. The conductance exceeds the DMM by $\sim 40\%$, despite a Debye temperature ratio of only about 1.6 [40].

To explain the excess conductance, researchers have proposed several models that account for roughly the same three types of phenomena as the models proposed to explain the "Kapitza anomaly" at low temperatures:

1. energy coupling between phonons and electrons [69–72];
2. non-equilibrium phonon distributions [26, 73–75]; and
3. inelastic phonon processes [76–81].

The number of plausible models relying on such disparate physical phenomena speaks both to the inherent complexity of the problem and to our own lack of understanding. Researchers have devoted much effort to identifying whether one of the phenomena on this list might explain most of the excess conductance.

1. In analyzing their experimental work, Stoner and Maris [39] considered the possibility that the excess conductance is explained by electron–phonon coupling that provides extra energy transmission channels not modeled in the DMM. However, they found an excess conductance by an order of magnitude at both interfaces of Pb/diamond and Pb/Bi/diamond, despite the Bi interlayer having a much smaller electron density. Lyeo and Cahill [67] saw the same effect when comparing Pb/diamond and Bi/diamond interfaces. They concluded that any electronic contribution is therefore unlikely to be the dominant cause. In addition, similar conductance trends have been observed in MD simulations that contain no electronic behavior [75, 82], suggesting that the explanation could be entirely phononic. Experimental measurement of an interface between poorly-matched non-metals could address this question directly. Unfortunately, I am aware of no such direct measurement at an isolated interfaces, since the primary

techniques for measuring conductance in systems with these small dimensions require a metallic film. In summary, the importance of electron–phonon energy transmission is likely to be small, but the question is not completely resolved.

2. The thermal conductance at an interface also depends on the phonon distribution, which in a transport scenario is not at equilibrium, contrary to the assumptions of the AMM and DMM. Two different causes of non-equilibrium are potentially important. The first cause is a non-zero heat current, as analyzed theoretically by Simons [26] and Chen [73]. The importance of this correction is unclear: in comparisons with MD simulations, Aubry *et al.* [74] concluded that the correction is important, while Landry and McGaughey [75] did not. The second potential cause of non-equilibrium is the boundary condition at the interface caused by the mode-dependent transmissivity. Landry and McGaughey hypothesized that this might better explain their simulation results. This idea is potentially supported by the recent MD results of Wu and Luo [83] and of Murakami *et al.* [84], which suggest a large contribution connected to thermalization in the bulk material near the interface.

3. References [39] and [67] both suggested inelastic transmission as the most likely explanation for their experimental results. Several models have been proposed that account for inelastic processes [76–81], each using a different phenomenological model for the details of the inelastic processes. See Section 2.4 for details on calculations. The models show somewhat improved agreement with experimental and simulated results, but all roughly at the same level, so their relative validity cannot be assessed. Recent MD simulations [85] have shown, however, that the dominant inelastic channels are frequency-halving and frequency-doubling, which lends particular support to the model proposed in Ref. [78].

In summary, many theories have been proposed to explain the anomalously high conductance at poorly-matched interfaces, but it has proven extremely difficult to evaluate their validity. Among them, theories involving inelastic phonon processes are most promising, but they still require much development before they are useful as predictive models.

1.4 Overview of this work

The objective of this work is to advance the understanding of the thermal conductance between solids at high temperature. Given the context of Section 1.3, this means seeking an explanation the large discrepancy between experimental measurements and the AMM and DMM. In particular, I focus on understanding the mechanisms that can cause conductance to exceed those models by an order of magnitude. The rest of this document is organized as follows.

- **Chapter 2: Theory and Methods.** I outline the theory of thermal transport in non-metals, with a focus on predicting the thermal conductance at an ideal interface between perfectly crystalline solids. In doing so, I also describe the tools I use to perform calculations within this theory: molecular dynamics simulations, lattice dynamics calculations, the Boltzmann transport equation, and the models for thermal conductance.

- **Chapter 3: Effects of Anharmonicity on Thermal Conductance.** I use the non-equilibrium molecular dynamics method to determine the thermal conductance as a function of temperature, $h(T)$. By varying the interatomic anharmonicity in different regions of the simulation domain, I control the inelastic processes in the system and observe their effect on $h(T)$.

- **Chapter 4: Effects of Anharmonicity on Phonon Transmission.** I use the wave packet method to determine the transmission of individual normal modes/phonons as a function of their frequency, $\alpha(\omega)$. I vary the interatomic anharmonicity and quantify the effect on inelastic processes at the interface.

- **Chapter 5: Effects of Anharmonicity on Phonon Distribution.** I use the wavelet transform to determine the energy distribution among normal modes during the non-equilibrium simulations of Chapter 3. I vary the interatomic anharmonicity and quantify the deviation of the energy distribution from equilibrium. To help interpret those results, I also use normal mode decomposition to determine the mean free paths of energy in those normal modes.

- **Chapter 6: Impact on Models of Thermal Conductance.** I use the observations of Chapters 3–5 to evaluate the various assumptions of the theories for thermal conductance described in Chapters 1 and 2. Based on these results, I identify inelastic processes in the vicinity of the interface, rather than inelastic transmission *across* the interface, as the most likely cause for the anomalously high conductance at high temperatures.

- **Chapter 7: Conclusions.** I summarize the major findings of this dissertation. In light of those findings, I propose new avenues for investigation.

Chapter 2

Theory and Methods

In this chapter, I outline two complementary perspectives for modeling the physical phenomena encountered in the applications described in Chapter 1. Perspective I tracks a given system using its atomic coordinates (Section 2.1), which is conceptually simple and works for a wide variety of systems. However, energy moves rapidly among the atomic coordinates, which necessitates computations on a timescale of fs. This is the approach of molecular dynamics. Perspective II tracks a system using its normal mode coordinates, which can be obtained by transformation from the atomic coordinates and are more convenient for modeling transport (Section 2.2). Energy moves among the normal mode coordinates in a fashion amenable to modeling by the Boltzmann transport equation, which has led to mature models for predicting thermal conductivity (Section 2.3). At interfaces, analogous models exist for predicting conductance, but have not yet achieved comparable success (Section 2.4). Finally, I outline the systems investigated in this work, which are designed to test those theories of interfacial phonon transport (Section 2.5).

2.1 Perspective I: Atomic coordinates

In the classical atomistic picture, one can model any body of material as a collection of N point masses interacting in a d-dimensional space, where $d = 1$, 2, or 3. To completely describe the solid therefore requires, at any given moment in time, a list of N positions $\mathbf{r}_i$ and a list of N velocities $\dot{\mathbf{r}}_i$, making a total of $2d \times N$ scalars. The coordinates of each atom i evolve in time according to Newton's equation of motion,

$$m_i \ddot{\mathbf{r}}_i(t) = \mathbf{F}_i(\mathbf{r}_1, \mathbf{r}_2, \ldots, \mathbf{r}_N, t). \tag{2.1}$$

$\mathbf{F}_i$ is the total force on the atom, which is itself a function of various atomic positions but typically not their velocities. To model any particular system—solids, liquids, gases, or a combination of them—one supplies the following information:

- the mass m_i of each atom;
- two initial conditions $\mathbf{r}_i(t_{\text{initial}})$ and $\dot{\mathbf{r}}_i(t_{\text{initial}})$ for each atom, since Eq. 2.1 is second-order in time; and
- the manner in which atoms exert forces on each other.

Many options exist for specifying the forces. In reality, those forces arise largely due to the interactions of the electrons surrounding the atomic nuclei, which this model cannot describe. If fidelity to a particular physical system is paramount, one can use a technique based on quantum mechanics to calculate those forces, such as density functional theory [86]. Otherwise, one can approximate the "true" forces by specifying one or more interatomic potential functions $U_n(\mathbf{r}_1, \mathbf{r}_2, \ldots, \mathbf{r}_m)$ accounting for m-body interactions, from which the system potential energy is

$$E^{\mathrm{P}} = \sum_n \sum_{i,j,\ldots,m} U_n(\mathbf{r}_i, \mathbf{r}_j, \ldots, \mathbf{r}_m).$$

Common examples are the Lennard-Jones potential for the noble gases ($m = 2$) [87] and the Stillinger–Weber potential for tetrahedrally-coordinated solids ($m = 3$) [88]. The force on each atom is then

$$\mathbf{F}_i = -\nabla_i E^{\mathrm{P}}.$$

Multiple potential functions U_n may be used in the same simulation to model different types of forces; for example, metallic and covalent interactions in a simulation of a Cu/Si interface [89].

In principle, these rules suffice to fully describe the system.[1] Macroscopic quantities can be calculated as functions of the basic atomic coordinates. For example, the temperature of a system in thermal equilibrium is given by the equipartition theorem:

$$T = \frac{1}{d\,k_{\mathrm{B}}}\frac{1}{N}\sum_i m_i \langle v_i^2(t)\rangle, \tag{2.2}$$

where $\langle v(t)\rangle$ is the temporal average of $v(t)$. The pressure of a system is [90]

$$P = -\left(\frac{dE}{dV}\right)_S = \frac{Nk_{\mathrm{B}}T}{V} + \frac{1}{dV}\left\langle \sum_i^N \mathbf{r}_i \cdot \mathbf{F}_i \right\rangle, \tag{2.3}$$

where V is the volume of the system.[2] Phononic properties, of particular interest in this work, can also be calculated directly from the atomic coordinates by various methods. I provide the details of those methods in the chapters in which I present the corresponding results.

2.1.1 Molecular dynamics

A molecular dynamics (MD) simulation is simply the implementation of the classical atomistic model in a computer program. For a thorough introduction to the practical implementation of MD, I recommend the book by Frenkel and Smit [90]. Here I discuss only general aspects

---

[1] In this work, all systems are closed: the number of atoms, system volume, and total energy are fixed (constant NVE). Modifications can be made to model systems under different conditions (e.g., NVT or NPT), but they are not used in this work.

[2] Calculating pressure in MD simulation has some practical caveats; e.g., Frenkel and Smit [90] discuss the effects of truncated and shifted potentials (F&S Section 3.2.2) and of choice of ensemble (F&S Section 4.5), and Louwerse and Baerends [91] discuss a correction for potentials with $m > 2$ under periodic boundary conditions.

of MD. For details on the particular simulation settings used in this work, see Section 2.5. For details on the actual code used, see Appendix A.

The scalar values corresponding to the per-atom variables $r_{i,\alpha}$ and $\dot{r}_{i,\alpha}$, where α indexes the d vector components, are stored in memory as arrays of size $N \times d$. The simulation-specific information—m_i, $(r_{i,\alpha}(t_{\text{initial}}), \dot{r}_{i,\alpha}(t_{\text{initial}}))$, and U_n—are specified by input from the user and stored in appropriate arrays as well. To integrate the equations of motion numerically in time—that is, to obtain $(\mathbf{r}_i(t+\Delta t), \dot{\mathbf{r}}_i(t+\Delta t))$ based on knowledge of $(\mathbf{r}_i(t), \dot{\mathbf{r}}_i(t))$—the code uses the velocity Verlet algorithm, which is described in Section 4.3.1 of Ref. [90]. The algorithm is simple but robust: it is accurate to second order in the timestep Δt, is reversible in time, and exhibits little long-term energy drift. To select a timestep that preserves energy, the user determine the highest characteristic frequencies of motion f_{max} based on the masses and forces in the system and choose $\Delta t \sim 10^{-2} f_{\text{max}}^{-1}$. The simulation then uses the integration scheme to evolve the system state one timestep at a time, until the simulation finishes.

In principle, this describes a fully functional MD program. To perform a particular "computational experiment" is then quite similar in concept to performing a real experiment. To paraphrase Frenkel and Smit, one needs to

1. prepare a sample: atomic masses, initial conditions, and potential functions;
2. control its environment: apply any system constraints such as temperature or pressure;
3. attach an instrument: e.g., a thermometer (Eq. 2.2) or barometer (Eq. 2.3);
4. process the resulting data.

As a final note, the largest computational expense is typically in the calculation of interatomic forces, which is necessary to integrate the equations of motion. If a system includes only two-body potentials (as in this work), a naïve algorithm that loops over all atoms i and then over potential neighbors $j \neq i$ requires computations of order $\mathcal{O}(N^2)$. However, the use of neighbor lists (or "Verlet lists") and/or cell lists reduces the cost to $\mathcal{O}(N)$. For further details, see Appendix A of this document and Appendix C of Ref. [90].

2.2 Perspective II: Normal mode coordinates

The atomistic perspective is conceptually straightforward, but it is sometimes not the most effective picture for modeling energy transport. One reason is the difficulty in accounting for the divergence from classical behavior at low temperatures due to quantum mechanics (Section 2.2.2). A second, related reason is that the equations of motion are strongly coupled when written in terms of the atomic coordinates. While the system kinetic energy, E^{K}, can be written as a sum of terms that each contain exactly one coordinate (specified per atom i and component $\alpha = x, y, z$),

$$E^{\mathrm{K}} = \sum_i \frac{1}{2} m_i |\dot{\mathbf{r}}_i|^2 = \sum_i \sum_\alpha E^{\mathrm{K}}_{i,\alpha}(\dot{r}_{i,\alpha}), \tag{2.4}$$

the system potential energy, E^{P}, cannot:

$$E^{\mathrm{P}} = \sum_{i,j,\ldots} U(\mathbf{r}_i, \mathbf{r}_j, \ldots) \neq \sum_i \sum_\alpha E^{\mathrm{P}}_{i,\alpha}(r_{i,\alpha}) \tag{2.5}$$

As a consequence, each of the $d \times N$ equations of motion contains coordinates of several different indices (i, α); i.e., they are coupled.[3] Given the complete set of coordinates $\mathbf{r}_i$ at any given moment, calculations are required on a rapid timescale (10^{-16}–10^{-15} s) to accurately determine the future trajectory of the system. Those calculations correspond to the computatonal cost of the MD method.

This suggests seeking a change of coordinates $r_{i,\alpha} \to \xi_{\mathbf{q},\nu}$ such that the system energy can then be written as a sum of decoupled terms, each of which contains only one coordinate $\xi_{\mathbf{q},\nu}$ or its time derivative:

---

[3] One can see this directly, for example, by applying the Hamiltonian formulation of mechanics to obtain the equations of motion from derivatives of the total system energy.

$$E^{\mathrm{K}} = \sum_{\mathbf{q}} \sum_{\nu} E^{\mathrm{K}}_{\mathbf{q},\nu}(\dot{\xi}_{\mathbf{q},\nu}) \text{ and} \tag{2.6}$$

$$E^{\mathrm{P}} = \sum_{\mathbf{q}} \sum_{\nu} E^{\mathrm{P}}_{\mathbf{q},\nu}(\xi_{\mathbf{q},\nu}). \tag{2.7}$$

Such a coordinate system is not guaranteed to exist, but if the transformation is possible, then the $d \times N$ equations of motion governing those coordinates would be completely decoupled. In other words, knowledge of $\xi_{\mathbf{q},\nu}(t_{\text{initial}})$ and $\dot{\xi}_{\mathbf{q},\nu}(t_{\text{initial}})$ at a single moment t_{initial} affords exact knowledge of $\xi_{\mathbf{q},\nu}(t)$ and $\dot{\xi}_{\mathbf{q},\nu}(t)$ forever, without needing to know the behavior of any other mode $(\mathbf{q}', \nu')$. Even if one obtains coordinates that are only *nearly* decoupled (see Section 2.3.2), calculations can be done on a much longer timescale than with the strongly coupled atomic coordinates.

Fortunately, such coordinate systems do exist in special cases. One such case is the simple but powerful model for crystalline solids described by Born and von Kármán in 1912 [92]. In this model, the boundaries of the d-dimensional domain are periodic; i.e., atomic positions satisfy $r_{i,\alpha} = r_{i,\alpha} \pm L_\alpha$, where L_α is the length of the simulation domain in the α direction. The domain is filled with a perfectly crystalline arrangement of N atoms, which interact with their neighbors via a harmonic potential

$$U(\mathbf{r}_i, \mathbf{r}_j) = \frac{1}{2} k (|\mathbf{r}_j - \mathbf{r}_i| - \Delta r_{\mathrm{eq}})^2. \tag{2.8}$$

Each atom has some equilibrium position $\mathbf{r}_{\mathrm{eq},i}$ at which $\nabla_i E^{\mathrm{P}} = 0$. To take advantage of periodicity, each of the N atoms is re-indexed as the j^{th} basis atom in the l^{th} unit cell in the crystal. In this case, there does exist a coordinate system that satisfies Eqs. 2.6 and 2.7, and those coordinates can be obtained from the atomic coordinates according to [93]

$$\xi_{\mathbf{q},\nu}(t) = \frac{1}{\sqrt{N}} \sum_{j,l} \sqrt{m_j} \exp\left(-i\mathbf{q}\cdot\mathbf{r}_{\mathrm{eq}}\right) \, \mathbf{e}^*_{\mathbf{q},\nu,j} \cdot \left[\mathbf{r}_{j,l}(t) - \mathbf{r}_{\mathrm{eq},j,l}\right]. \tag{2.9}$$

These are commonly called "normal mode coordinates", since one interprets the values[4] of $(\xi_{\mathbf{q},\nu}(t), \dot{\xi}_{\mathbf{q},\nu}(t))$ as the collective displacement and collective velocity of atoms in a spatial pattern corresponding to the normal mode $(\mathbf{q}, \nu)$. In crystalline systems, that spatial pattern is described by a plane wave of wavevector $\mathbf{q}$ and polarization vectors $\mathbf{e}_{\mathbf{q},\nu,j}$, one vector for each basis atom j. The wavevector prescribes the relative motion of the unit cells in the crystal, while the polarization vectors prescribe the relative motion of the basis atoms within each unit cell. I use the convention that the wavevector is defined as

$$\mathbf{q} = \sum_{\alpha} \frac{2\pi}{\lambda_\alpha} \vec{\alpha} \tag{2.10}$$

in terms of wavelengths λ_α projected along Cartesian unit vectors $\vec{\alpha}$.

The equations of motion governing the coordinates $\xi_{\mathbf{q},\nu}(t)$ can be derived from Newton's equations for the atomic coordinates (Eq. 2.1), using Eq. 2.8 to define the interatomic forces. The result is a system of $d \times N$ equations that are completely decoupled, each one governing the evolution of a separate normal mode $(\mathbf{q}, \nu)$:

$$\ddot{\xi}_{\mathbf{q},\nu} = -\omega^2_{\mathbf{q},\nu} \xi_{\mathbf{q},\nu}, \tag{2.11}$$

where $\omega_{\mathbf{q},\nu}$ is the natural angular frequency of the mode. In order to use Eqs. 2.9 and 2.11, one must identify the wavevector $\mathbf{q}$, polarization vector $\mathbf{e}_{\mathbf{q},\nu,j}$, and frequency $\omega_{\mathbf{q},\nu}$ corresponding to each of the $d \times N$ normal modes $(\mathbf{q}, \nu)$.

---

[4] Note that the coordinates are complex-valued, and their complex phase stores the information regarding the relative phase of the vibrational motion.

Now, the total system energy is a sum of terms that each depend on exactly one coordinate,

$$E = \sum_{\mathbf{q},\nu} \frac{1}{2}|\dot{\xi}_{\mathbf{q},\nu}|^2 + \sum_{\mathbf{q},\nu} \frac{1}{2}\omega^2_{\mathbf{q},\nu}|\xi_{\mathbf{q},\nu}|^2, \tag{2.12}$$

which satisfies Eqs. 2.6 and 2.7. The velocity at which energy propagates in each mode is given by its group velocity, $\mathbf{v}_{\mathbf{q},\nu}$, which can be calculated from the frequency surface corresponding to the polarization of that mode:

$$\mathbf{v}_{\mathbf{q},\nu} = \nabla_{\mathbf{q}}\omega_{\mathbf{q},\nu}. \tag{2.13}$$

The problem, now, is how to actually identify those special wavevectors and polarization vectors that can be substituted into Eq. 2.9 to successfully transform the atomic equations of motion, Eq. 2.1, into the decoupled equations of motion, Eq. 2.11.

2.2.1 Lattice dynamics

The process of identifying the list of normal modes, the polarization vectors $\mathbf{e}_{\mathbf{q},\nu,j}$, and the frequencies $\omega_{\mathbf{q},\nu}$ is called a lattice dynamics calculation. A general algorithm to solve this problem becomes clear if one writes each system of equations as a matrix equation. For example, Eq. 2.1 for a monatomic 1D chain with nearest-neighbor interactions would look like

$$m \begin{bmatrix} \vdots \\ \ddot{\mathbf{r}}_{i-1} \\ \ddot{\mathbf{r}}_i \\ \ddot{\mathbf{r}}_{i+1} \\ \vdots \end{bmatrix} = \begin{bmatrix} \ddots & k & & & \\ k & -2k & k & & \\ & k & -2k & k & \\ & & k & -2k & k \\ & & & k & \ddots \end{bmatrix} \begin{bmatrix} \vdots \\ \mathbf{r}_{i-1} \\ \mathbf{r}_i \\ \mathbf{r}_{i+1} \\ \vdots \end{bmatrix}, \tag{2.14}$$

while we seek Eq. 2.11 of the form

$$\begin{bmatrix} \vdots \\ \ddot{\xi}_{\mathbf{q},\nu-1} \\ \ddot{\xi}_{\mathbf{q},\nu} \\ \ddot{\xi}_{\mathbf{q},\nu+1} \\ \vdots \end{bmatrix} = \begin{bmatrix} \ddots & & & & \\ & -\omega^2_{\mathbf{q},\nu-1} & & & \\ & & -\omega^2_{\mathbf{q},\nu} & & \\ & & & -\omega^2_{\mathbf{q},\nu+1} & \\ & & & & \ddots \end{bmatrix} \begin{bmatrix} \vdots \\ \xi_{\mathbf{q},\nu-1} \\ \xi_{\mathbf{q},\nu} \\ \xi_{\mathbf{q},\nu+1} \\ \vdots \end{bmatrix} . \tag{2.15}$$

The transformation is therefore equivalent to diagonalizing the matrix in Eq. 2.14. A more complex system than the 1D chain would lead to more entries in the matrix, but as long as it is diagonalizable, the same method applies. This is the general approach of practical lattice dynamics calculations. Each eigenvalue of the matrix in Eq. 2.15 provides a normal mode frequency, and the associated eigenvector performs the same transformation written in Eq. 2.9, thereby providing the wavevector $\mathbf{q}$ and polarization $\mathbf{e}_{\mathbf{q},\nu}$ for that normal mode.

We therefore have the machinery to take any crystalline material and identify a list of coordinates $\xi_{\mathbf{q},\nu}$ and their associated properties $\mathbf{q}$, $\mathbf{e}_{\mathbf{q},\nu}$, and $\omega_{\mathbf{q},\nu}$. Fortunately, this is a sufficiently common task that software is already available to perform these calculations efficiently. In this work, I use the program GULP [94], which is freely available for academic researchers, to calculate the normal modes in the Ar-like materials simulated in this work. The frequencies of normal modes with $\mathbf{q}$ along $\langle 100 \rangle$ directions, for example, are plotted as blue lines in Fig. 2.1a. The dispersion relations along these high-symmetry directions can also be calculated analytically [93] as

$$\omega_\nu(q) = \sqrt{\frac{4k_\nu}{m}} \sin\left(\frac{qa}{4}\right) , \tag{2.16}$$

where k_ν is an effective "interplanar" force constant that depends on polarization. For the $\langle 100 \rangle$ directions, the interplanar force constants for longitudinal and transverse waves are related to the interatomic force constant by $k_\mathrm{L} = 2k$ and $k_\mathrm{T} = k$ (see Chap. 2 of Ref. [93]).

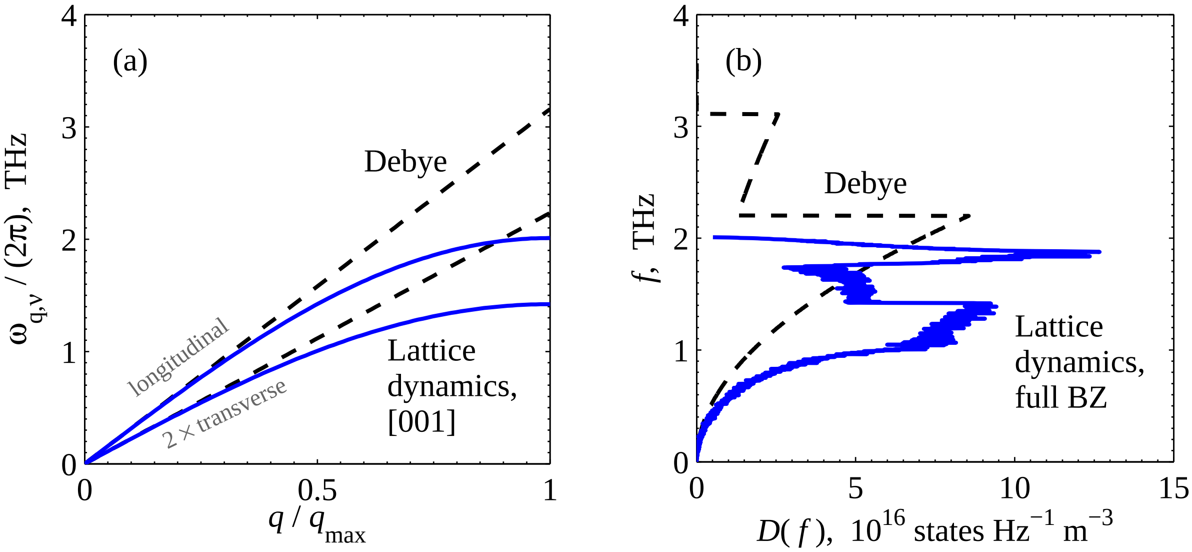

Figure 2.1: Vibrational modes of the simulated Ar-like system, calculated by lattice dynamics (solid blue) and by the Debye model (dashed black). (a) The dispersion relations of modes in the $\langle 100 \rangle$ directions. (b) The density of states per frequency in 3D.

This dispersion relation is only representative of a small fraction of the normal modes in the full three-dimensional Brillouin zone [40], so I also calculate and plot the density of states in frequency, $D(\omega)$, in Fig. 2.1b.[5] The highest densities of normal modes occur near 2 THz and 1.4 THz, where the $\langle 100 \rangle$ dispersion branches are flat, indicating that $\omega_\nu(\mathbf{q})$ throughout $\mathbf{q}$ space generally exhibits flat features near those frequencies. For comparisons with experimental results and with MD-based calculations, see Section 2.5.

For completeness, I would like to mention the Debye model for the normal modes of a crystal, which is still occasionally used in lieu of lattice dynamics calculations to estimate the frequencies $\omega_{\mathbf{q},\nu}$ of the normal modes of a crystal. The Debye model assumes that the frequency of each normal mode is proportional to the magnitude of its wavevector [40]:

$$\omega_{\mathbf{q},\nu} = v_{\mathrm{D}}|\mathbf{q}|. \tag{2.17}$$

---

[5] Throughout this work, I follow the common convention of using angular frequency ω in developing theory but linear frequency f in reporting actual values. The convention is not ideal, but I follow it to facilitate comparison with other work.

The group velocity is a constant, and the modes are said to be "dispersionless." Originally, the model used a single, averaged speed for all three polarization [40]. In order for the "Debye crystal" to have the same number of degrees of freedom as the real crystal it models, the maximum wavenumber is $q_{\mathrm{D}} = (6\pi^2 N/V)^{1/3}$. This corresponds to a maximum frequency $\omega_{\mathrm{D}} = v_{\mathrm{D}} q_{\mathrm{D}}$, which leads to the definition of the Debye temperature

$$T_{\mathrm{D}} = \hbar\omega_{\mathrm{D}}/k_{\mathrm{B}} = \frac{\hbar v_{\mathrm{D}}}{k_{\mathrm{B}}}\left(\frac{6\pi^2 N}{V}\right)^{1/3}. \tag{2.18}$$

The Debye temperature is often used as a fitting parameter to model the specific heat of solids. The resulting temperature is then used to compare the relative "stiffness" of materials [40], as in the literature reviewed in Section 1.3. It is also commonly used to represent the rough boundary between low-temperature quantum behavior and high-temperature classical behavior, as discussed in Section 2.2.2. Using this averaged-speed model, $T_{\mathrm{D}} = 85$ K [40] for solid Ar, and $T_{\mathrm{D}} = 49$ K for the "heavy Ar" simulated in this work, corresponding to a Debye temperature ratio of $\sqrt{3} \approx 1.7$. For more details on the true normal mode frequencies in these systems, see Section 2.5.

To assess the accuracy of the Debye assumption, I have plotted Equation 2.17 in Fig. 2.1a using the corresponding sound speeds for the Ar-like material simulated in this work. Instead of using only one speed for all modes, here I assign a sound speed $v_{\mathrm{D},\nu}$ for each polarization, as Swartz and Pohl did in the DMM [35]. The Debye model assumes that Eq. 2.17 is isotropic in reciprocal space [40], leading to the density of states plotted as the dashed black line in Fig. 2.1b. The model is evidently a good approximation to the true normal modes at low frequencies only. The Debye model is therefore acceptable at low temperatures, where energy only occupies the low-frequency modes. However, the Debye model does not accurately represent the high-frequency modes, and full lattice dynamics calculations should instead be used in predicting transport at high temperature, as shown by Reddy *et al.* at interfaces [41].

Unfortunately, even if one uses lattice dynamics to obtain accurate normal modes of a crystal, the classical physics used until this point predicts the wrong *energy occupancy* of those normal modes at low temperature. To quantitatively delineate these low- and high-temperature regimes requires arguments based on quantum mechanics.

2.2.2 Quantization and phonons

Unfortunately, as Richard Feynman put it, "nature isn't classical, dammit, and if you want to make a simulation of nature, you'd better make it quantum mechanical" [95]. Therefore, in this section, I outline the quantum mechanics relevant to phonon transport, and I identify how its predictions differ from those of classical physics. To be clear, I do not refer to the quantum mechanical behavior of the electrons surrounding the nuclei. That aspect is important for obtaining accurate interatomic forces, as in Section 2.1. Rather, I refer to the quantum mechanical behavior of the normal modes themselves: colloquially, the "freezing out" of the high-frequency modes. Whether these effects are important in a given system depends on the magnitudes of the normal mode frequencies $\omega_{\mathbf{q},\nu}$. For scale, the normal modes of silicon have associated frequencies $\omega_{\mathbf{q},\nu}$ in the range of approximately 0 to 16 THz [96]. One can therefore roughly estimate the temperature above which, at thermal equilibrium, energy occupies all of the normal modes classically:[6]

$$T_{\text{classical,Si}} \approx \frac{\hbar\omega_{\text{max}}}{k_{\text{B}}} \approx 770\text{ K}.$$

The maximum vibrational frequency of GaN is even higher—roughly 22 THz [97]. Therefore, an accurate model of thermal transport in devices at any reasonable temperature should account for quantum mechanical effects.

To determine the equation of motion for the quantum mechanical system—i.e., the Schrödinger equation—one translates the Hamiltonian from the classical picture. The system dynamics are contained in a wavefunction Ψ that lives in $(2d \times N + 1)$-dimensional space, and one can choose to project it onto either the atomic coordinates of Section 2.1 or the

---

[6] Cf. the Debye temperature of silicon, $T_{\text{D}} \sim 625\,\text{K}$ [40].

normal mode coordinates of Section 2.2. The decoupled form of the classical Hamiltonian when written in normal mode coordinates (Eq. 2.12) makes them the natural first choice. In that case, the wavefunction depends on $(d \times N)$ normal mode displacements, $(d \times N)$ normal mode velocities, and time: $\Psi(\xi_1, \ldots, \xi_{d\times N}, \dot{\xi}_1, \ldots, \dot{\xi}_{d\times N}, t)$. The classical normal mode coordinates correspond to quantum mechanical operators $\hat{\xi}_{\mathbf{q},\nu}$ and $\hat{\dot{\xi}}_{\mathbf{q},\nu}$, denoted by a "hat." The Schrödinger equation in these coordinates can be written by direct translation from the classical Hamiltonian (see, e.g., Chap. 11 of Ref. [93]):

$$\hat{\mathcal{H}}\Psi = \left(\sum_{\mathbf{q},\nu}\frac{1}{2}\hat{\dot{\xi}}^2_{\mathbf{q},\nu} + \sum_{\mathbf{q},\nu}\frac{1}{2}\omega^2_{\mathbf{q},\nu}\hat{\xi}^2_{\mathbf{q},\nu}\right)\Psi = i\hbar\frac{\partial\Psi}{\partial t}. \tag{2.19}$$

From here, one exploits the fact that Eq. 2.19, which governs the behavior of the entire N-atom system, is mathematically identical to the equation describing a system of $d \times N$ completely independent harmonic oscillators, each with a natural frequency of $\omega_{\mathbf{q},\nu}$. In other words, since the Hamiltonian is diagonal in these coordinates, we can seek a solution using separation of variables:

$$\Psi = \psi_{\mathbf{q}_1,\nu_1} \cdots \psi_{d\times N}\psi_t. \tag{2.20}$$

Each $\psi_{\mathbf{q},\nu}$ depends only on $\xi_{\mathbf{q},\nu}$ and $\dot{\xi}_{\mathbf{q},\nu}$. By substitution into Eq. 2.19, one obtains an independent equation governing each $\psi_{\mathbf{q},\nu}$:

$$\left(\frac{1}{2}\hat{\xi}^2_{\mathbf{q},\nu} + \frac{1}{2}\omega_{\mathbf{q},\nu}\hat{\dot{\xi}}^2_{\mathbf{q},\nu}\right)\psi_{\mathbf{q},\nu} = E_{\mathbf{q},\nu}\psi_{\mathbf{q},\nu}, \tag{2.21}$$

where the total system energy corresponding to the state Ψ is

$$E = \sum_{\mathbf{q}}\sum_{\nu} E_{\mathbf{q},\nu}. \tag{2.22}$$

As promised, Eq. 2.21 is identical to the time-independent Schrödinger equation governing a quantum harmonic oscillator, and it must bear the same solution.[7] The energy in each oscillator—i.e., in each normal mode—can therefore only take on discrete values of

$$E_{\mathbf{q},\nu} = \hbar\omega_{\mathbf{q},\nu}\left(n_{\mathbf{q},\nu} + \frac{1}{2}\right), \text{ where } n_{\mathbf{q},\nu} = 0, 1, \ldots, \tag{2.23}$$

leading to the familiar result that normal mode $(\mathbf{q}, \nu)$ can exist only in discrete vibrational states $n_{\mathbf{q},\nu}$ that differ in energy by $\hbar\omega_{\mathbf{q},\nu}$.[8] The frequency is the same as that obtained using the (classical) lattice dynamics of Section 2.2.1.

This implies that, in a system at temperature T, only modes $(\mathbf{q}, \nu)$ with sufficiently low frequency $\omega_{\mathbf{q},\nu} < k_\mathrm{B}T/\hbar$ are capable of accepting the ambient thermal energy of order $k_\mathrm{B}T$. Modes of higher frequency are likely to be "frozen" in their ground state $n_{\mathbf{q},\nu} = 0$, and therefore they do not contribute to thermodynamic and transport properties at that temperature. This strange phenomenon explains, for example, the experimental fact that the specific heats of crystals are much lower than the classical Dulong–Petit value at temperatures $T \lesssim \hbar\omega_\mathrm{max}/k_\mathrm{B}$, where ω_max is the highest frequency of any normal mode in the crystal.

This picture finally enables the formal definition of a *phonon*: a single parcel of energy corresponding to $\Delta n_{\mathbf{q},\nu} = 1$. Unlike electrons, phonons are not fundamental particles, but it can be convenient to treat them as such, since they do exhibit particle-like properties: they are discrete (countable) and transport energy in finite amounts $\hbar\omega_{\mathbf{q},\nu}$ at a well-defined velocity given by Eq. 2.13. Therefore, the state of a system Ψ can be specified in terms of the energy distribution of a "population of phonons," which simply means specifying the number $n_{\mathbf{q},\nu}$ of energy quanta in each of the $d \times N$ normal modes of the system. In a system at thermal equilibrium, that number is given by the Bose–Einstein distribution [40]:

$$n_{\mathbf{q},\nu} = n_\mathrm{B\text{–}E}(\omega_{\mathbf{q},\nu}, T) = \frac{1}{\exp\left(\frac{\hbar\omega_{\mathbf{q},\nu}}{k_\mathrm{B}T}\right) - 1}. \tag{2.24}$$

---

[7] The normal mode coordinate operators do satisfy the same commutation relation as the usual position and momentum operators, $[\hat{\xi}_{\mathbf{q},\nu}, \hat{\dot{\xi}}_{\mathbf{q},\nu}] = i\hbar$ [93], which is necessary to make this argument.

[8] The solution for each $n_{\mathbf{q},\nu}$ also specifies the probability distribution $\psi_{\mathbf{q},\nu}$ for the normal mode displacement, but as far as I know, the latter is not used directly in any thermal transport calculations.

In a system in thermal non-equilibrium, the distribution is governed by the Boltzmann transport equation, described in Section 2.3.1.

Finally, I point out that any classical model (e.g., a molecular dynamics simulation) does not contain any notion of phonons in this strict sense. Each normal mode coordinate $\xi_{\mathbf{q},\nu}$, and therefore the energy in that mode, can vary continuously regardless of mode frequency. However, it is ubiquitous usage to interchange "phonon" and "normal mode," and I will often do so in this work. The meaning is clear, I hope, in context. Results of MD simulations are therefore only strictly valid at temperatures significantly greater than $\hbar\omega_{\max}/k_{\mathrm{B}}$. At lower temperatures, MD simulations erroneously allow high-frequency modes to accept arbitrarily small amounts of energy. However, interpreting MD results at low temperatures can be done with caution by identifying the corresponding energy per mode, $E_{\mathbf{q},\nu} = \hbar\omega_{\mathbf{q},\nu}\, n_{\mathbf{q},\nu}$, with the knowledge that in the classical limit, the equilibrium distribution is

$$\lim_{\hbar\to 0} n_{\mathrm{B\text{–}E}}(\omega_{\mathbf{q},\nu}, T) = \frac{k_{\mathrm{B}}T}{\hbar\omega_{\mathbf{q},\nu}} \tag{2.25}$$

such that $E_{\mathbf{q},\nu} = k_{\mathrm{B}}T$. In principle, one can then account for the effect of quantization by correcting the distribution function. For further discussion, see Chapter 5, in which I obtain the energy per mode in non-equilibrium MD simulations.

2.3 Bulk transport

In this section I outline the theory for phonon transport in bulk crystals, since it is also applicable to describe transport in the materials adjacent to an interface. The theory is based on the expression for the heat flux in an arbitrary direction z based on the phonon picture developed in the previous section:

$$\frac{\dot{Q}_z}{A} = \frac{1}{V}\sum_{\mathbf{q}}\sum_{\nu} v_{\mathbf{q},\nu,z}\, \hbar\omega_{\mathbf{q},\nu} n_{\mathbf{q},\nu}, \tag{2.26}$$

where $v_{\mathbf{q},\nu,z}$ is the projection of $\mathbf{v}_{\mathbf{q},\nu}$ onto the z axis and $n_{\mathbf{q},\nu}$ is the number of phonons in each mode. Commonly, the collection of numbers $n_{\mathbf{q},\nu}$ is called the phonon distribution. All of the other quantities on the right hand side—the list of normal modes, with the group velocity and frequency of each mode—can be calculated using the lattice dynamics methods of the previous section. Therefore, all that remains is to model the phonon distribution in the material, which is done using the Boltzmann transport equation.

2.3.1 The Boltzmann transport equation

The Boltzmann transport equation (BTE) is a governing equation for the distribution function of any large system of energy carriers in non-equilibrium [98]. In this work, we are interested in steady, one-dimensional transport, in which case the energy in each normal mode varies along the z axis. Equivalently, the number of phonons in each mode varies with z. In this case, the BTE for each mode $(\mathbf{q},\nu)$ reduces to [99, 100]

$$v_{\mathbf{q},\nu,z}\,\frac{dn_{\mathbf{q},\nu}(z)}{dz} = \left(\frac{\partial n}{\partial t}\right)\bigg|_{\mathrm{c}}, \tag{2.27}$$

where the entire term on the right hand side is a symbol representing the "collision integral." In its exact form, this term represents the extremely complex coupling between the mode $(\mathbf{q},\nu)$ and each other mode. However, in many cases [101] one can make the single-mode relaxation time approximation (SMRTA)

$$\left(\frac{\partial n}{\partial t}\right)\bigg|_{c} \approx -\frac{n_{\mathbf{q},\nu}(z) - n_{\mathrm{B\text{–}E}}(\omega_{\mathbf{q},\nu}, T(z))}{\tau_{\mathbf{q},\nu}}, \tag{2.28}$$

where $n_{\mathrm{B\text{–}E}}$ is the the Bose–Einstein distribution, Eq. 2.24, at the local "temperature" $T(z)$.[9] Phenomenologically, the SMRTA presumes that each normal mode relaxes to thermal equilibrium with the other modes, and that this relaxation occurs exponentially with some time constant $\tau_{\mathbf{q},\nu}$. The relaxation time of each mode is an input to the model and must be

---

[9] This is commonly interpreted as the "equivalent equilibrium temperature" as discussed by Chen [100]. Minnich's review [102] provides the quantitative definition of $T(z)$, which he calls the "local pseudo-temperature."

determined by other means. Several different mechanisms might cause the thermal relaxation: one might consider impurity/defect scattering, electron–phonon scattering, boundary scattering, and phonon–phonon scattering. In the systems I simulate in this work, the only two applicable mechanisms are boundary scattering and phonon–phonon scattering. I discuss the latter in more detail in Section 2.3.2.

For now, I assume that the SMRTA is valid and that one can obtain the corresponding relaxation times $\tau_{\mathbf{q},\nu}$. Equation 2.27 then becomes a first-order differential equation and can be readily solved for $n_{\mathbf{q},\nu}$, subject to boundary conditions. From this point, I discuss two common uses of the equation: (1) calculating the thermal conductivity by approximating the BTE to first order and (2) obtaining exact numerical solutions.

1. One obtains the "linearized BTE" by approximating

   $$\frac{dn}{dz} \approx \frac{dn_{\text{B–E}}}{dz}$$

   in Eq. 2.27 [100]. This is equivalent to assuming that the gradient of n' is negligible compared to the gradient of $n_{\text{B–E}}$, which implicitly varies in space due to $T(z)$. This leads to a simple solution for the number of phonons in each mode:

   $$n_{\mathbf{q},\nu} \approx n_{\text{B–E}} - v_{\mathbf{q},\nu,z}\tau_{\mathbf{q},\nu}\frac{\partial n_{\text{B–E}}}{\partial T}\frac{dT}{dz}. \tag{2.29}$$

   Substituting this expression into the heat flux summation, Eq. 2.26, and comparing it to the Fourier law $\dot{Q}_z = -\kappa\frac{dT}{dz}$ immediately provides an expression for predicting the thermal conductivity κ in terms of phonon properties:

   $$\kappa_z = \frac{1}{V}\sum_{\mathbf{q},\nu} v^2_{\mathbf{q},\nu,z}\tau_{\mathbf{q},\nu}\hbar\omega_{\mathbf{q},\nu}\frac{\partial n_{\text{B–E}}}{\partial T} \tag{2.30}$$

2. If the first-order approximation is insufficient, one can solve Eq. 2.27 directly. In most scenarios, the transport is caused by small departures from equilibrium, such that

$n - n_{\text{B–E}} \ll n_{\text{B–E}}$, in which case it numerically easier to obtain the deviation from equilibrium $n' \equiv n - n_{\text{B–E}}$ rather than n itself. In that case, Eq. 2.27 is rewritten as

$$\frac{n'_{\mathbf{q},\nu}(z)}{dz} + \frac{n'_{\mathbf{q},\nu}(z)}{v_{\mathbf{q},\nu,z}\tau_{\mathbf{q},\nu}} = -\frac{\partial n_{\text{B–E}}}{\partial T}\frac{dT(z)}{dz}, \tag{2.31}$$

where, strictly speaking, the group velocity and relaxation time also vary with the local temperature $T(z)$. The solution is [43]

$$n'_{\mathbf{q},\nu}(z) = \underbrace{n'_{\mathbf{q},\nu}(z_0)\exp\left[\frac{-(z-z_0)}{v_{\mathbf{q},\nu,z}\tau_{\mathbf{q},\nu}}\right]}_{\text{A}} - \underbrace{\int_{z_0}^{z}\frac{\partial n_{\text{B–E}}}{\partial T}\frac{dT(z)}{dz}\exp\left[\frac{z'-z}{v_{\mathbf{q},\nu,z}\tau_{\mathbf{q},\nu}}\right]dz'}_{\text{B}}, \tag{2.32}$$

which requires knowledge of the value $n'_{\mathbf{q},\nu}(z_0)$ on a boundary at z_0. Physically, the solution states that the *excess* number of phonons in a mode, $n'_{\mathbf{q},\nu}$, is the combination of (A) a "ballistic" contribution from the boundary, which decays on the length scale of the mean free path $v\tau$, and (B) an "accumulated" correction to the equilibrium number $n_{\text{B–E}}$ due to changes in $T(z)$.

The first approach has been demonstrated to great effect in recent years by Ward, Broido, and coworkers [103, 104], who use density functional theory to calculate the force constants in bulk materials, from which they obtain the relaxation times of the allowed three-phonon processes. Their predictions of thermal conductivity agree quite convincingly with experimental data, which suggests that the theory outlined until this point in the chapter provides an accurate model for thermal transport in many bulk crystals. The second approach has also been demonstrated very successfully. Equation 2.32 is readily generalized to multi-dimensional and unsteady transport, as detailed in a recent review by Minnich [102]. Those analogues have been used to determine the thermal response of systems that macroscopic heat diffusion models fail to describe, such as short-period superlattices [43], transistor hot spots [105], and recent experiments deliberately designed to probe sub-diffusive phonon transport [106].

However, to date, models for interfacial transport have not yet shown success at a similar level. The prevailing models are described in Section 2.4. In the intervening section, I provide a brief introduction to the calculation of the relaxation times $\tau_{\mathbf{q},\nu}$ in this work.

2.3.2 Coupling of normal modes

The systems simulated in this work are defect-free, so the primary mechanism for thermalization is phonon–phonon scattering. In real crystals, the true interatomic forces are not purely harmonic; Equation 2.8 is only the second-order term in a Taylor expansion of the true interatomic potential. If we include higher-order terms in r, then the operations that diagonalize Eq. 2.14 only *approximately* diagonalize the true force matrix, leaving off-diagonal terms that couple the equations of motion.

This would seem to undermine the entire purpose of using normal mode coordinates, but fortunately the coupling is typically weak enough that one can use the harmonic model in combination with perturbations from a small third-order term. Peierls pioneered this analysis in 1929 [107] in both the classical and quantum mechanical pictures. Essentially, energy propagates in the manner of the harmonic normal modes but can exchange among certain triplets of states $[(\mathbf{q},\nu)$, $(\mathbf{q}',\nu')$, $(\mathbf{q}'',\nu'')]$. To reduce the cumbersome notation, here I refer to each normal mode $(\mathbf{q},\nu)$ by a single index i. In the exchange, the energy in one mode must change in the opposite direction to the energy in the other two modes, so without losing generality I choose the convention

$$\Delta E_i + \Delta E_{i'} \leftrightharpoons \Delta E_{i''}.$$

Coupling is possible among the triplets of states (i, i', i'') that correspond to a non-zero, third-order term in the total system energy. Without performing detailed calculations, note that such terms include the combination $\xi_i \xi_{i'} \xi_{i''}$, which can only be non-zero if the triplet satisfies the spatial resonance condition (see Eq. 2.9)

$$\mathbf{q} + \mathbf{q}' = \mathbf{q}'' + \mathbf{G}, \tag{2.33}$$

where $\mathbf{G}$ is any reciprocal lattice vector (including the zero vector), and the temporal resonance condition (see Eq. 2.11)

$$\omega_i + \omega_{i'} = \omega_{i''}. \tag{2.34}$$

Equation 2.34 is also interpreted in the quantum mechanical picture as the conservation of energy among three discrete jumps $\hbar\omega$, so this is often called a "three-phonon process." Thus, note that extending Eq. 2.8 to include m^{th}-order terms enables "m-phonon processes."

For each triplet satisfying these conditions, one can calculate the characteristic timescale of energy exchange, or relaxation time, $\tau_{i,i',i''}$, directly from knowledge of third-order terms in the system potential energy [98]. In general, each mode i may be involved in many such triplets, and those individual relaxation times can be combined to obtain a total relaxation time τ_i for that mode [103, 108]. As an alternative, one can "empirically" calculate the total relaxation time of each mode from molecular dynamics simulation using the method described in Section 5.3. With the relaxation time obtained using either method, one can multiply it by the group velocity $\mathbf{v}_i$ of that normal mode to obtain a mean free path Λ_i.

Finally, armed with a list of normal modes $(\mathbf{q}, \nu)$, one can use their properties from the harmonic approximation along with their total relaxation times to calculate transport properties using the BTE, as described in Section 2.3.1.

2.4 Interfacial transport

Just as for bulk transport, theories of interfacial transport are generally predicated on the heat flux expression of Eq. 2.26. At an interface between two materials labeled 1 and 2, the expression provides the heat flux incident on the interface from each side, based on the normal modes of each pure material. Although the normal modes of the entire interfacial system do not correspond exactly to the normal modes of the isolated materials, one assumes that they *nearly* diagonalize the force matrix, and that the off-diagonal terms can be captured by modeling the energy exchange among these "nearly-normal" modes. This is similar to the spirit of modeling the dynamics in an anharmonic system using the modes of a harmonic system, as described in Section 2.3.2.[10]

Thus Eq. 2.26 provides the heat flux *incident* on the interface, but only some yet-unknown fraction $\alpha_{\mathbf{q},\nu}$ of the energy in each mode transmits to the other material. Therefore, the total heat flux from material 1 to material 2 is

$$\frac{\dot{Q}_{1\to2}}{A} = \frac{1}{V}\sum_{\mathbf{q}^+}\sum_{\nu} v_{\mathbf{q},\nu,z}\,\hbar\omega_{\mathbf{q},\nu}\,n_{\mathbf{q},\nu}\,\alpha_{\mathbf{q},\nu,1\to2}, \tag{2.35}$$

where the normal modes are those of the pure material 1, and $\mathbf{q}^+$ denotes the modes with wavevectors inclined toward the interface only. The heat flux from material 2 to material 1 is written in the same manner. The thermal conductance of the interface, h, can then be calculated using the empirical macroscopic definition

$$h = \lim_{\dot{Q}_{\text{net}}\to0}\frac{\dot{Q}_{\text{net}}}{A\,\Delta T}, \tag{2.36}$$

where the net heat current is $\dot{Q}_{\text{net}} = \dot{Q}_{1\to2} - \dot{Q}_{2\to1}$ and the temperature jump is $\Delta T = |T_1 - T_2|$. The small-flux limit corresponds to the regime in which the thermal response remains linear, so that h does not vary with $\dot{Q}_{\text{net}}$. If the numbers of incident phonons $n_{\mathbf{q},\nu}$ do not correspond to an equilibrium distribution, then the temperatures T_i are not perfectly well-defined in a thermodynamic sense. In that case, they are "effective" temperatures that correspond to an equilibrium distribution with the same total energy [100, 102].

---

[10] One can also take the approach of determining the true normal modes of the full interfacial system, as in the recent work of Gordiz and Henry [109]. However, the approach requires significantly more calculation, and to my knowledge, no full theories for predicting conductance have yet been demonstrated in those coordinates, so the predictive advantage is unclear.

In the foregoing sections, I have discussed all of the phononic properties that appear in Eq. 2.35 except for the transmissivity, $\alpha_{\mathbf{q},\nu}$. Historically, most conductance modeling has concentrated on determining effective estimates of $\alpha_{\mathbf{q},\nu}$, while assuming that $\omega_{\mathbf{q},\nu}$ and $\mathbf{v}_{\mathbf{q},\nu}$ are well-modeled by those of the harmonic modes (or, more crudely, the Debye model) and that $n_{\mathbf{q},\nu} \approx n_{\text{B–E}}(\omega_{\mathbf{q},\nu}, T)$. The AMM and DMM fall into this category, as well as most of their later modifications. I discuss this approach in Section 2.4.1. Some research, although significantly less, has also investigated the importance of understanding $n_{\mathbf{q},\nu}$ beyond the equilibrium assumption. Those findings are discussed in Section 2.4.2.

2.4.1 Models for transmissivity

As described in Section 1.3, the prevailing models for predicting conductance are the acoustic mismatch model (AMM) and the diffuse mismatch model (DMM). Both models assume that the incident phonon population is well approximated by an equilibrium distribution. They also assume that the system is well approximated by harmonic interactions, in which case energy in a mode $(\mathbf{q}_1, \nu_1)$ in Material 1 can only transmit into modes $(\mathbf{q}_2, \nu_2)$ in Material 2 with the same vibrational frequency, $\omega_{\mathbf{q}_1,\nu_1} = \omega_{\mathbf{q}_2,\nu_2}$. Such processes are commonly known as "elastic." This condition arises from the same reasoning as the condition in Eq. 2.34 for the frequencies in three-phonon processes.

The constraint of elastic transmission makes it convenient to use $\alpha_{i\to j}(\omega)$ rather than $\alpha_{\mathbf{q},\nu,i\to j}$, and therefore the flux expression is often recast from wavevector space, as in Eq. 2.35, to frequency space:

$$\frac{\dot{Q}_{i\to j}}{A} = \sum_{\nu} \int_0^{2\pi} d\phi \int_0^{\pi/2} \sin\theta \, d\theta \int d\omega \; v_\nu(\omega) \cos\theta \; \hbar\omega \; D_\nu(\omega) \; n_{\text{B–E}}(\omega, T_i) \; \alpha_{\nu,i\to j}(\omega), \quad (2.37)$$

where θ is the incidence angle, ϕ is the azimuthal angle, and $D(\omega)$ is the density of normal modes per frequency, per volume. This presumes a change of coordinates $(q_x, q_y, q_z) \to$

(ω, θ, ϕ), which requires caution in cases in which multiple wavevectors $\mathbf{q}$ in the same polarization ν have the same frequency. Therefore, Eq. 2.37 can be used to calculate the conductance in frequency space under the Debye assumption [35] or using an isotropic dispersion with no local minima [42], but calculations using exact dispersion relations [36, 41] are based in the more fundamental formulation in wavevector space. The AMM and DMM then differ only in how the transmissivity $\alpha(\omega)$ is calculated.

- The AMM treats phonon transmission as the specular refraction of elastic waves, governed by equations exactly analogous to Snell's law and the transmission of electromagnetic waves. In the first approximation [19], which is still occasionally used [110], the transmission can be estimated without careful accounting for mode conversion, using dispersionless sound speeds:

  $$\alpha_{\nu,i\to j}(\omega) = 1 - \left(\frac{Z_{\nu,i}\cos\theta_{\nu,i} - Z_{\nu,j}\cos\theta_{\nu,j}}{Z_{\nu,i}\cos\theta_{\nu,i} + Z_{\nu,j}\cos\theta_{\nu,j}}\right)^2, \qquad (2.38)$$

  where $Z_{\nu,i} = \rho_i v_{nu,i}(0)$ is the product of the material density and sound speed, and the angles $\theta_{\nu,i}$ and $\theta_{\nu,j}$ are related by Snell's law. Equation 2.38 is only strictly accurate for transverse waves with polarization vectors in the plane of the interface, which cannot couple to the other polarizations [111]. The model used by Maris and coworkers [36] accounts for both dispersion and mode conversion, while adhering to the assumptions of harmonic forces and specular refraction, providing in my view a faithful test of the assumptions of the AMM. At high temperatures, this calculation grossly underpredicts the experimental conductance at poorly-matched interfaces by as much as two orders of magnitude, as discussed in Section 1.3.

- The DMM treats phonon transmission as the completely diffuse scattering of elastic waves, based on the physical premise that transmitted phonons preserve their frequency but lose any correlation with their orientation or polarization.[11] As a result, the

---

[11] Duda *et al.* [79] discuss variations on the exact details of these constraints.

transmissivity from i to j is a function of frequency only, and the diffuse assumption implies that $\alpha_i(\omega) + \alpha_j(\omega) = 1$ [35]. Using Eq. 2.37 in the limit that $\dot{Q}_{\mathrm{net}} \to 0$ provides the expression

$$\alpha_{i\to j}(\omega) = \frac{\sum_\nu v_{\nu,j}(\omega)\ D_{\nu,i}(\omega)}{\sum_\nu v_{\nu,i}(\omega)\ D_{\nu,j}(\omega) + \sum_\nu v_{\nu,j}(\omega)\ D_{\nu,j}(\omega)}. \tag{2.39}$$

As with the AMM, the original formulation of the DMM used sound speeds. Using the full dispersion leads to a much different prediction at high temperatures than using the Debye approximation [41, 42], providing a better test of the diffuse assumption. At high temperatures, this calculation also underpredicts the experimental conductance at poorly-matched interfaces, but not as severely as the AMM.

The shortcomings of these transmissivity models in terms of predicting experimental data were discussed in Section 1.3. In this work I am interested in models using inelastic processes to explain the anomalously high conductance at poorly-matched interfaces. For example, Hopkins [78] proposed the Higher Harmonic Inelastic Model (HHIM) as an extension to the DMM. In addition to the elastic (i.e., 2-phonon) processes allowed in the DMM, the HHIM defines additional transmissivity terms $\alpha^{(n)}_{\nu,i\to j}$ corresponding to n-phonon processes. The HHIM allows only processes involving combinations of phonons of equal frequency. Hopkins *et al.* [80] also later proposed the Anharmonic Inelastic Model (AIM) which allows combinations of arbitrary frequency, provided that they satisfy the conservation of energy (as in Eq. 2.34). Other conductance models that incorporate inelastic scattering include Refs. [76, 77]. All of these models have been shown to improve conductance predictions to some degree, despite making fundamentally different assumptions about the nature of the inelastic processes. Since little is known empirically about inelastic processes, researchers have been largely unable to determine which models are most valid.

Some distinguishing information has been provided by Sääskilahti *et al.* [85], who used MD simulations to probe in detail the types of phonon transmission events occuring at an interface. While elastic processes $\omega_i = \omega_j$ contribute the majority of the conductance, they observe that the remaining conductance is heavily dominated by frequency-doubling and frequency-halving processes. This lends support to the underlying assumptions of the HHIM. Future work should revisit the HHIM to validate it in more detail, perhaps by relaxing the Debye assumption, and by using simulations such as those in Ref. [85] to compare with the predicted contributions of each n-phonon process.

2.4.2 Models for the phonon distribution

Corrections to the phonon distribution may also contribute to the anomalous conductance at mismatched interfaces. I am aware of two types of corrections that might be made: (1) due to a non-zero heat current, and (2) due to the boundary conditions at the interface, which couple energy among different modes.

1. Based on the linearized BTE (Eq. 2.29), a non-zero heat current causes the number of phonons in each mode to deviate from the equilibrium value by *approximately*

$$n_{\mathbf{q},\nu} - n_{\text{B–E}} \approx -v_{\mathbf{q},\nu,z}\tau_{\mathbf{q},\nu}\frac{\partial n_{\text{B–E}}}{\partial T}\frac{dT}{dz}. \tag{2.40}$$

   While the AMM, DMM, and their derivatives use the “zeroth-order” approximation $n_{\mathbf{q},\nu} \approx n_{\text{B–E}}$ in Eq. 2.35 for the heat flux, Eq. 2.40 provides a first-order correction. Simons [26] and Chen [73] provide analyses of the effect on the predicted conductance, and both Aubry *et al.* [74] and Landry and McGaughey [75] have compared the predictions with MD simulations with mixed results. The conductance h_{NE} predicted using the non-equilibrium correction is indeed significantly greater than the conductance h_{E} based on equilibrium distributions, which is qualitatively consistent as an explanation for the excess conductance.

   However, I note two potential issues with the explanation. First, Katerberg *et al.* [30] observed that, although $h_{\text{NE}} > h_{\text{E}}$, the excess conductance is predicted to be greater at interfaces with *closely* matched properties, in apparent contradiction with experiments. Second, the correction does not predict the continuing increase in $h(T)$ reported in both experiments [67, 68] and MD simulations [75, 82].

2. Alternatively, one can use the full BTE solution in Eq. 2.32 to assemble a system of equations, each governing a separate mode and coupled to one another at the interface via the boundary conditions $n'_{\mathbf{q},\nu}(z_0)$. Solving the system numerically provides exact values for $n'_{\mathbf{q},\nu}(z)$, which can then be used in Eqs. 2.35 and 2.36 to calculate the conductance; for example, see the calculations by Chen [43] for interfaces in Si/Ge and GaAs/AlAs superlattices. However, this method requires the transmissivity α as input, so until the community reaches a consensus on realistic methods for calculating α, the phonon distributions and conductances obtained in this manner can only provide qualitative insight at best.

2.5 Systems modeled in this work

The simulations performed in this work were designed to evaluate the various theories summarized in Section 2.4. In choosing the model system, I am not concerned with reproducing any real material in particular. I seek the simplest possible system in which I can observe the effect of anharmonicity on interfacial thermal conductance and on phonon transport. A system meeting these criteria, similar to systems used in past MD studies of interfacial conductance [82, 85, 112], is the interface is between solid Ar (40 amu) and solid "heavy Ar" (120 amu). The crystalline structure of both materials is given by the face-centered cubic Bravais lattice with one basis atom. The interatomic forces are modeled using the Lennard-Jones potential,

$$U_{\mathrm{LJ}}(\mathbf{r}_i, \mathbf{r}_j) = 4\epsilon \left[\left(\frac{\sigma}{r_{ij}} \right)^{12} - \left(\frac{\sigma}{r_{ij}} \right)^{6} \right], \tag{2.41}$$

where $r_{ij} = |\mathbf{r}_i - \mathbf{r}_j|$. It is computationally inexpensive to use and features extensive literature for validation. In order to isolate the effect of anharmonicity, I also use the harmonic approximation to U_{LJ} about $r_{ij} = \Delta r_{\mathrm{eq}}$:

$$U_{\mathrm{harmonic}}(\mathbf{r}_i, \mathbf{r}_j) = -\epsilon + \frac{1}{2}k(r_{ij} - \Delta r_{\mathrm{eq}})^2, \tag{2.42}$$

where $\Delta r_{\mathrm{eq}} = 2^{1/6}\sigma$ is the equilibrium separation, and the force constant is related to the LJ parameters by $k = 36(2)^{2/3}\,\epsilon\,\sigma^{-2}$. Comparing the thermal transport in systems with forces governed by U_{LJ} and U_{harmonic} elucidates the effect of anharmonicity in Ar-like materials. I also separate the effects of interfacial inelastic scattering (Section 2.4.1) and the incident phonon distribution (Section 2.4.2) by using both harmonic and anharmonic forces in different regions of the same system.

The particular values of the parameters used in this work are listed in Table 2.1. A major difference with most other work is that I allow interactions only between atoms within the distance r_{cut}, which is chosen to include only nearest neighbors. The main reason is that, since U_{harmonic} does not tend to zero as $r_{ij} \to \infty$, it is ill-suited to describing the forces of more distant neighbors. Therefore, I also limit the interaction of the LJ potential to nearest neighbors only, so that U_{harmonic} remains a true approximation to U_{LJ}. Note that, while only pairs of nearest neighbors are allowed to interact, the range of those allowed interactions is not limited by r_{cut}, so that $U_{\mathrm{LJ}} \to 0$ smoothly as $r_{ij} \to \infty$. This differs from the common usage of truncated and/or shifted potentials that define a distance r_{cut} beyond which $U = 0$; for example, see Section 3.2.2 of Ref. [90].

To facilitate comparison between the systems of different dimensionality, the parameters in the 1D chain are chosen to reproduce the interactions among the {100} planes of the fcc lattice, which are spaced apart at half the conventional lattice parameter and exert interplanar forces equivalent to twice the interatomic forces [93]. As a result, both systems have the same effective lattice parameter of $a = 5.313$ Å at $T = 0$ K (compared to the value of 5.311 Å extrapolated from experimental data [113]), and the 1D chain exhibits the same phonon

Table 2.1: Interatomic Potential Parameters Used in This Work

		1D	3D
U_{LJ} (Eq. 2.41)	ϵ (eV)	0.01617	0.01617
	σ (Å)	2.367	3.347
	r_{cut} (Å)	4.0	4.5
U_{harmonic} (Eq. 2.42)	k (eV Å^{-2})	0.1650	0.08249
	Δr_{eq} (Å)	2.657	3.757
	r_{cut} (Å)	4.0	4.5

Table 2.2: Coefficients for Zero-Pressure Lattice Parameter of LJ Argon (Eq. 2.43)

	1D	3D
a_0 (Å)	5.313	5.313
a_1 (Å K^{-1})	4.792×10^{-3}	1.813×10^{-3}
a_2 (Å K^{-2})	-7.171×10^{-5}	4.792×10^{-6}
a_3 (Å K^{-3})	6.101×10^{-6}	1.394×10^{-8}

dispersion as the modes along the $\langle 100 \rangle$ directions of the 3D crystal.

To account for thermal expansion, simulations were performed to determine the zero-pressure lattice constant of the LJ systems as a function of temperature. The simulations produced values of $a(T)$ on the temperature ranges of $T = 1$ to 16 K (1D) and $T = 5$ to 60 K (3D), which fit well to a third-order polynomial function

$$a(T) = a_0 + a_1 T + a_2 T^2 + a_3 T^3. \tag{2.43}$$

The fitted coefficients are provided in Table 2.2.

To assess how well the parameters of Table 2.1 model the atomic dynamics in solid Ar, I have used normal mode decomposition (Section 5.3) to obtain the normal mode frequencies from MD simulations of the 3D crystal at finite temperature. They are plotted in Fig. 2.2 in comparison with experimental neutron scattering measurements in solid Ar by Batchelder *et al.* [114]. The normal modes in the simulated system accurately reproduce the

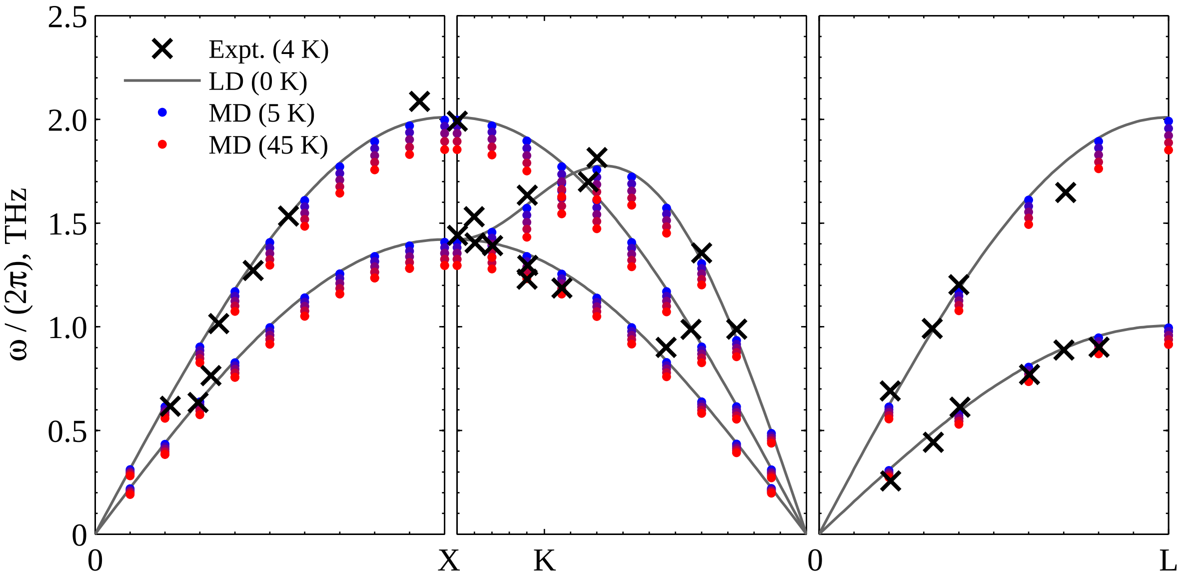

Figure 2.2: Phonon dispersion in Ar from experimental measurement, lattice dynamics calculation, and molecular dynamics simulations at $T = (5, 15, 25, 35, 45)$ K.

real normal modes at low T, and they also show the expected decrease of phonon frequencies due to anharmonicity as T increases. The heavy Ar has the same phonon dispersion with frequencies scaled by a factor of $3^{-1/2}$.

In all simulations, I found that integrating the equations of motion using a discrete timestep of $\Delta t = 2$ fs provided a satisfactory compromise between computational expense and energy conservation. This Δt corresponds to 1/250 of the period of the highest-frequency normal modes seen in Fig. 2.2. In the worst case—the highest-temperature (50 K) non-equilibrium simulations of Section 3.2.2—this discretization caused fluctuations in the total energy on the order of 0.01 eV and an absolute drift of roughly 0.3 eV, corresponding to a rate of $+2.5 \times 10^{-5}$ eV ps^{-1} in the total system energy over the course of the 12 ns simulation. For comparison, the simulations at 50 K have a total kinetic energy of roughly 75 eV among 11 232 atoms and a constant heat current of 0.01 eV ps^{-1}.

The remaining simulation details vary by method, and they are provided in the corresponding chapters.

Chapter 3

Effects of Anharmonicity on Thermal Conductance

In this chapter, I focus on observing the macroscopic heat transfer at the interface, as summarized in the thermal conductance. Specifically, I show how the thermal conductance changes depending on the anharmonicity of the interatomic forces throughout the system—both at the interface and in the bulk materials. I calculate the conductance using the non-equilibrium molecular dynamics method, described in Section 3.1. I present the results of the one-dimensional and three-dimensional simulations in Section 3.2, and I discuss their implications in Section 3.3.

3.1 Non-equilibrium molecular dynamics

The non-equilibrium molecular dynamics (NEMD) method is analogous in format to a steady-state experimental measurement of thermal conductance. Given some sample structure, the simulation adds a steady heat current to one region and removes the same heat current from another region. In response to the heat current between the source and sink, the temperature distribution in the material becomes non-uniform, eventually reaching a steady state. The

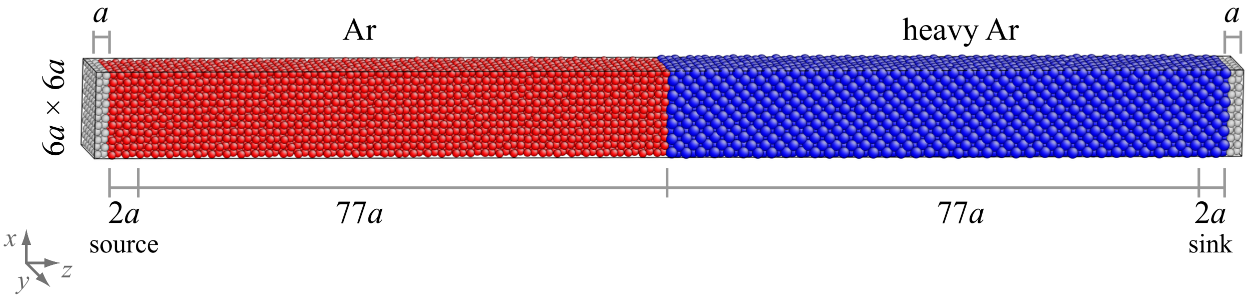

Figure 3.1: Geometry of the domain for non-equilibrium simulations in three dimensions.

relationship between the heat current and resulting temperature distribution provides thermal transport properties such as thermal conductivity and thermal conductance.

3.1.1 Methodology

All of the NEMD simulations in this work use a similar system geometry. The domain is periodic in all directions; i.e., atomic positions satisfy $r_{i,\alpha} = r_{i,\alpha} \pm L_\alpha$, where L_α is the length of the simulation domain in the α direction.

The three-dimensional domain has dimensions of 6 × 6 × 80 conventional unit cells, as sketched in Figure 3.1. For a given system temperature, the length of each cubic cell is specified by Equation 2.43 and Table 2.2. The heat current is oriented along the long dimension of the domain (z axis). On each end, two (002) planes are held fixed as walls (144 atoms), and the velocities of the next four (002) planes are scaled at each timestep to add or remove the steady heat current. The length of each "bulk material"—i.e., the distance from a heat source or sink to the interface—is therefore approximately 20 nm.

The one-dimensional domain has dimensions such that the system has the same total number of atoms, $N = 11520$, and the same number of atoms per region. The length of each bulk material is approximately 1.5 μm. The much longer domain was chosen for two reasons: to allow the same degree of statistical averaging as in the 3D system, and to adjust for the smaller thermal resistance of the 1D system.

Each simulation consists of three stages: (1) equilibration at the overall system temperature T with no heat current, (2) "turning on" the heat current until the temperature distribution reaches a steady state, and (3) data collection.

1. The simulation begins with the atoms in their equilibrium positions, $E^{\mathrm{P}} = 0$, and with kinetic energy equivalent to twice the nominal temperature. For simplicity, the initial atomic velocities are set to the corresponding uniform magnitude of $|\mathbf{v}| = (2dk_{\mathrm{B}}T_{\mathrm{nominal}}/m)^{1/2}$ with random orientation. Any resulting net momentum of the system is subtracted out from the initial condition to prevent drift. The simulation then runs for 20 ps, at which point the system has reached thermal equilibrium at a true temperature slightly less than T_{nominal} due to anharmonicity of the potential energy. Although inelegant, this procedure ensures that simulations at the same T_{nominal} have the same true temperature, which can be difficult to enforce precisely if using a thermostat for initialization and switching to NVE for data collection.

2. After equilibration, the heat source and heat sink are "turned on." Different methods are available for transferring the heat current. They can be grouped into two types: (1) those that maintain a known temperature in the region and (2) those that maintain a known heat current. Whichever quantity is specified, the other is unknown and must be measured during data collection. Both types of methods have been used widely in the literature to calculate thermal transport properties. Unfortunately, I am aware of no algorithm that produces an ideal temperature reservoir, which would absorb all incident phonons without reflection while emitting a perfectly thermalized spectrum—i.e., a phononic black body. The development of such algorithms is a challenge in itself and remains an active field of research; see, for example, Ref. [115] published this year. In the absence of a better algorithm, I fix the heat current using the scheme described by Jund and Jullien [116] for all of the NEMD simulations in this work. In Section 3.1.2 I assess the effect of this algorithm on the phonon spectra in my simulations.

In selecting the magnitude of the heat current, it must be large enough to create a measurable ΔT at the interface, but small enough to remain in the linear regime in which $\dot{Q} \propto \Delta T$ is valid. In addition, the velocity adjustment should correspond to a small ratio of the kinetic energy per atom per timestep. With these constraints in mind, the heat current in each simulation was prescribed proportionally to T_{nominal}, such that $\dot{Q} = 3.2 \times 10^{-12}$ W for each K in the 1D system or 3.2×10^{-11} W for each K in the 3D system. The heat current is applied for 4 ns before data collection to allow the temperature distribution to reach a steady state.

3. Finally, temperature is sampled locally over time to obtain an accurate measurement of the steady-state temperature distribution. I decompose the system into spatial subdomains of M atoms each and calculate the local temperature of each subdomain as

$$T = \frac{1}{d\,k_{\mathrm{B}}} \frac{1}{M} \sum_{i}^{M} m_i \langle v_i^2 \rangle. \tag{3.1}$$

Just as with Equation 2.2, the use of Equation 3.1 is problematic if the M atoms in the subdomain are not in thermal equilibrium. In Section 3.1.2 I present evidence that, in all of the NEMD simulations in this work, the M atoms in each subdomain are very near thermal equilibrium, at least in regard to the atomic picture. The $d \times M$ normal modes of the subdomain, however, may not be near thermal equilibrium, as discussed in Section 5.2, so the local temperature calculated using Equation 3.1 must be interpreted carefully.

In the 3D systems, I define 160 subdomains, each containing one [002] plane ($M = 144$). Since the heat current is directed along the z axis, all of the atoms in each subdomain must have the same average kinetic energy, and averaging their temperatures is justified. In the 1D systems, no atoms share the same average kinetic energy, but I also use $M = 144$ in order to reduce statistical fluctuations. This is equivalent to applying a smoothing procedure to the average kinetic energies, and since I calculate the conductance by fitting linear models to the temperature distributions, the spatial binning does not affect the calculation.

The temperature data are collected for 8 ns. The temperature is sampled in each subdomain in intervals of 1 ps. Running averages and standard deviations are stored in memory and written to disk every 40 ps, which reduces access time and disk requirements.

Each simulation thus provides a one-dimensional temperature distribution $T(z)$. I use the common procedure for extracting the thermal conductance at the interface: I fit a linear model to the temperature profiles in the two "bulk-like" regions and extrapolate them to the interface. I define ΔT as the difference between the extrapolated values, from which I calculate $h = \dot{Q}\Delta T^{-1}$.

3.1.2 Verification

First, I present the results of a single NEMD simulation and, before attempting to calculate the conductance, I assess the details of the transport. The steady-state temperature profile $T(z)$ of a one-dimensional system with Lennard-Jones forces is shown in Figure 3.2. The nominal temperature of the simulation is $T = 10$ K. Each black dot represents the temperature of a single "subdomain," with the shaded area corresponding to one standard deviation in the temperature fluctuations.

To assess the thermalization of energy in the system, I arbitrarily select two regions on each side of the interface. One region contains 1440 Ar atoms in $z \in (-0.765, -0.383)$ µm, and the second region contains 1440 heavy Ar atoms in $z \in (0.383, 0.765)$ µm. These regions are marked in red and blue, respectively, in Figure 3.2, and are labeled with their average temperature. In each region, I assess the extent to which energy has equilibrated among the atomic coordinates (Section 2.1) and among the normal mode coordinates (Section 2.2).

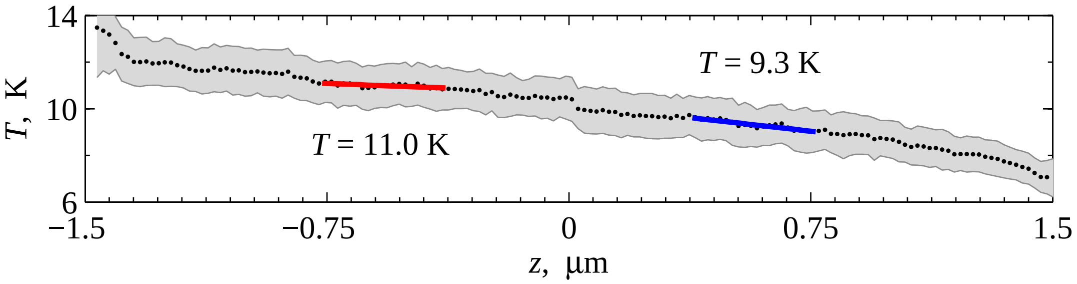

Figure 3.2: The steady-state temperature profile resulting from a one-dimensional NEMD simulation with Lennard-Jones forces at $T = 10$ K.

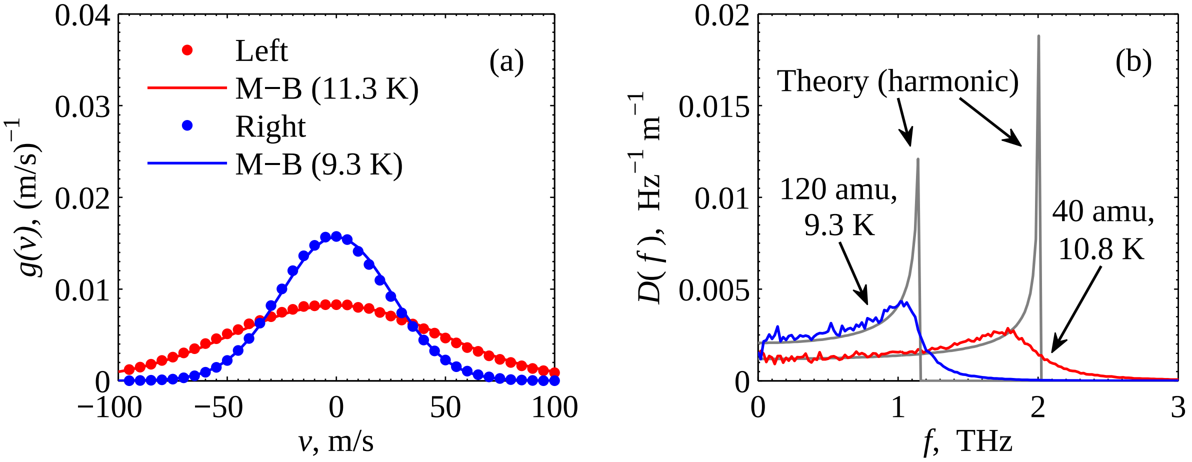

Figure 3.3: Assessing the equilibration of energy during NEMD simulations in the 1D LJ system. (a) Atomic speed distributions sampled during the simulation (dots) and predicted by theory (lines). (b) The density of states sampled from the simulation (colored lines) and predicted (black lines).

In the atomic coordinates, I first calculate the temperature in each region assuming equipartition, finding $T_{\text{atomic,left}} \approx 11.3$ K and $T_{\text{atomic,right}} \approx 9.3$ K. I then compare the Maxwell–Boltzmann distributions at those temperatures,

$$g_{\text{M–B}}(v) = \sqrt{\frac{m}{2\pi k_{\text{B}} T_{\text{atomic}}}} \exp\left(-\frac{mv^2}{2k_{\text{B}} T_{\text{atomic}}}\right), \tag{3.2}$$

to the actual distributions of atomic velocities sampled in each region. Those theoretical and measured distributions are plotted in Fig. 3.3a. The agreement suggests that, in each region, energy has indeed equilibrated among the atomic coordinates.

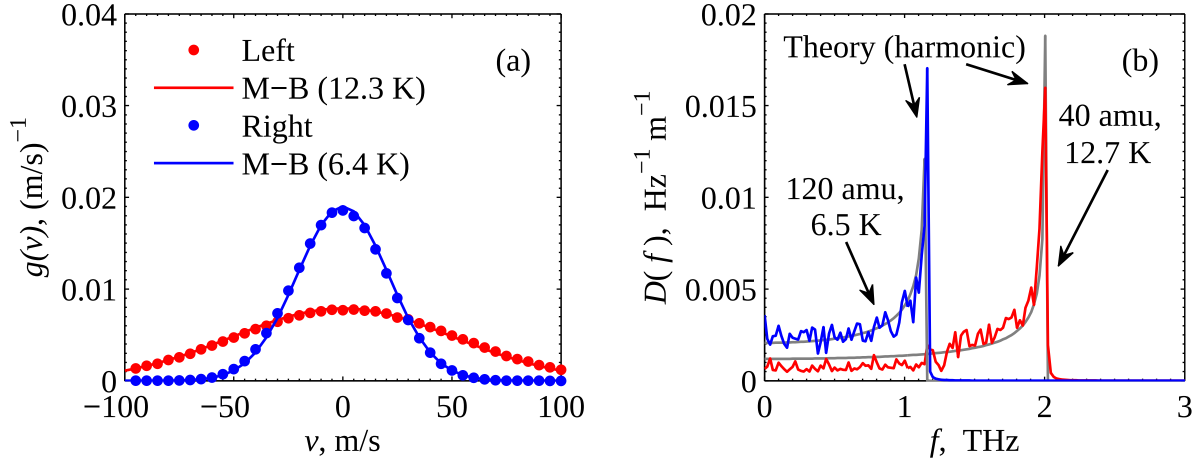

Figure 3.4: The same as Figure 3.3, but in a system with harmonic forces.

I also assess the equilibration of energy among the normal mode coordinates by calculating the density of states in frequency space $D(\omega)$. In each region, the average kinetic energy per frequency per length, $E^{\mathrm{K}}(\omega)$, is equivalent to the Fourier transform of the temporal autocorrelation of the atomic velocities:

$$E^{\mathrm{K}}(\omega) = \mathcal{F}\left\{\sum_i \frac{m_i}{2}\langle \dot{r}_i(t)\cdot \dot{r}_i(0)\rangle\right\}. \tag{3.3}$$

This kinetic energy spectrum is equal to the energy per mode times the density of states: $E^{\mathrm{K}}(\omega) = E^{\mathrm{K}}_{\mathbf{q},\nu}(\omega_{\mathbf{q},\nu})\, D(\omega)$. The system is classical, so if it is in thermal equilibrium, then the energy per mode is simply $k_{\mathrm{B}}T$. However, it is not known beforehand how close the system actually is to equilibrium. In Fig. 3.3b, I plot the quantity

$$D_{\mathrm{equiv}} = \frac{E^{\mathrm{K}}(\omega)}{k_{\mathrm{B}}T_{\mathrm{equiv}}}, \tag{3.4}$$

where D_{equiv} is only equal to the true density of states, $D(\omega)$, if the system is in thermal equilibrium. I define the equivalent temperature, T_{equiv}, as the temperature if the system corresponding to the total kinetic energy in the system:[1]

---

[1] I use Parseval's theorem along with the fact that, even if the precise form of $D(\omega)$ is unknown, its integral must result in the number of states per length, $2/a$, since in 1D, I set a to twice the interatomic spacing.

$$T_{\text{equiv}} = \frac{a}{2k_{\text{B}}} \int E^{\text{K}}(\omega) d\omega, \tag{3.5}$$

where $E^{\text{K}}(\omega)$ is measured from the simulation using Equation 3.3. This is consistent with the concept used, for example, by Chen [43] and by Minnich [102]. I use this equivalent temperature in Eq. 3.4 to plot $D_{\text{equiv}}(\omega)$ in red and blue in Fig. 3.3b. Also plotted in black is the theoretical density of vibrational states in a one-dimensional chain with harmonic forces:

$$D_{\text{harmonic}}(\omega) = \frac{2}{\pi a} \sqrt{\frac{4k_2}{m} - \omega^2}. \tag{3.6}$$

The sampled $D_{\text{equiv}}(\omega)$ in each region closely resembles the theoretical D_{harmonic} except at high frequencies, which I attribute to broadening due to phonon–phonon scattering in the anharmonic system. Note that the cutoff frequencies are correctly reproduced in comparison with the $\langle 100 \rangle$ dispersion relation shown in Figure 2.2. In addition, the calculated values of T_{equiv} agree within a few percent with the calculated T_{atomic}. Overall, I conclude that the energy in the system is well thermalized among both the atomic and normal mode coordinates in the Lennard-Jones system.

For comparison, in Figure 3.4 I have also plotted the same quantities from an NEMD simulation in a harmonic system. Due to the lack of anharmonic phonon–phonon scattering as a mechanism for thermalization, one might suspect that energy would not equilibrate among the coordinates. However, the thermal energy does appear well equilibrated. Note that the lack of broadening from phonon–phonon scattering allows the sampled $D_{\text{equiv}}(\omega)$ to reproduce the ideal $D_{\text{harmonic}}(\omega)$ very closely. Therefore, I conclude that the energy in the system is well thermalized in the harmonic system as well.[2]

At this point, I have shown that the temperature profiles calculated using T_{atomic} also correspond to sensible values of T_{equiv}. The linear fits in Regions 1 and 2 can therefore be

---

[2] Closer inspection of Fig. 3.4b reveals a non-equilibrium in $D_{\text{equiv}}(\omega)$ in the Ar. At frequencies below roughly 1.2 THz, $D(\omega)$ exhibits a deficit, which balances an apparent excess in $D(\omega)$ above 1.2 THz. This effect is investigated further in Chapter 5, and it does not change the present conclusions.

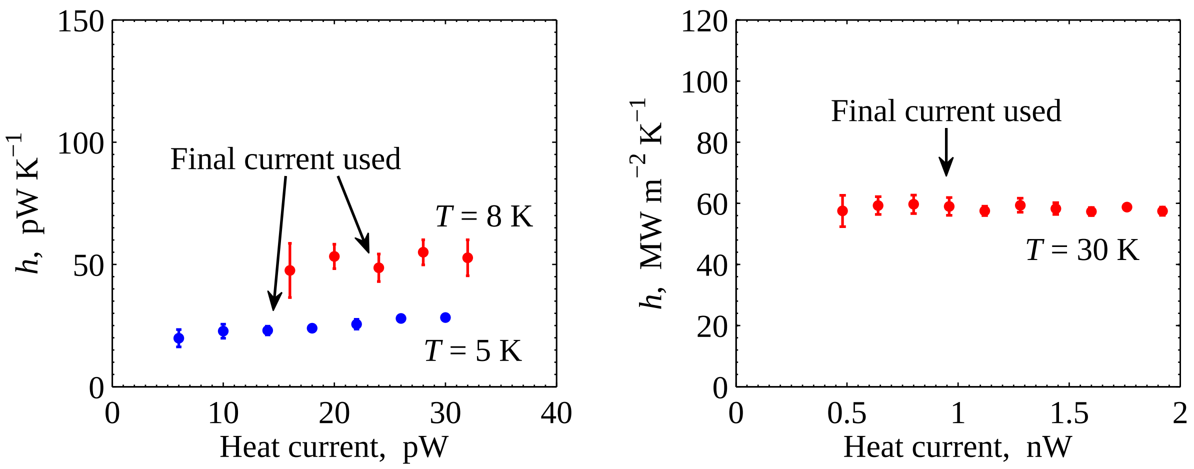

Figure 3.5: The thermal conductance h measured using a range of heat currents $\dot{Q}$ in one-dimensional systems (left) and three-dimensional systems (right).

used to calculate the conductance h as described above. As a final point of verification, I test whether the magnitudes of heat current used in these simulations are small enough so that the linearity of Equation 2.36 is satisfied; i.e., so that h is constant with $\dot{Q}$. Figure 3.5 shows the conductances measured in both one- and three-dimensional systems as a function of the imposed heat current. The error bars denote $\pm 2s/\sqrt{n}$, where s is the standard deviation of $n = 6$ simulations with randomized initial conditions. The heat currents used in the final simulations are marked with arrows. Based on these results, I am satisfied that the heat currents are large enough to resolve h but small enough to remain linear in ΔT.

3.2 Results: Thermal conductance

To test the theories for $h(T)$ described in Section 2.4, I use this simulation scheme to calculate $h(T)$ at Ar/heavy Ar interfaces. In both one- and three-dimensional systems, I report the conductance with three different arrangements of interatomic forces:

a) all Lennard-Jones (anharmonic),

b) all harmonic, and

c) all harmonic except between the two atoms (1D) or atomic planes (3D) immediately adjacent to the interface, which interact through the Lennard-Jones potential.

In presenting the following results, I use the letters (a), (b), and (c) to refer to these arrangements of forces.

3.2.1 In one dimension

Three representative steady-state temperature profiles collected in one-dimensional systems are shown in Figure 3.6. Each corresponds to a different arrangement of forces as described above. The resulting conductance h is inversely proportional to the temperature drop at the interface, and since the same heat current is used in all three simulations at $T_{\text{nominal}} = 6\ K$, the relative magnitudes of ΔT can be directly compared across the three plots. The calculated conductance is therefore highest in (a), and it is smaller in (b) and (c) in which the values ΔT are roughly equal. Aside from the conductance, $T(z)$ in the bulk materials has a significantly greater slope in (a) than in (b) and (c), corresponding to a smaller thermal conductivity. This is consistent with the anharmonic forces in (a) compared to the harmonic forces in the bulk materials in (b) and (c), which exhibit practically horizontal profiles (i.e., $k \ \rightarrow \infty$).

These simulations are repeated across a range of nominal temperatures from $T = 2$ to 12 K, in increments of 2 K, to collect the data displayed in Figure 3.7. Each data point is the mean of $n = 30$ simulations,[3] The relative magnitudes of h resulting from different arrangements of forces are consistent with the comparison among the single simulations. Furthermore, note that the “excess” conductance in the LJ system grows with temperature, while the conductance in the harmonic system is nearly perfectly constant with T. The conductance in the harmonic system with the LJ interface is slightly higher, which is not readily apparent in Figure 3.6, but by a much smaller margin than in the all-LJ system. For comparison, I've also plotted the value of interfacial conductance predicted using Eq. 2.36 under the assumptions

---

[3] This is a much larger number of simulations than typical, which was necessitated by the much wider temperature fluctuations in the 1D profiles than in 3D: compare Figures 3.6 and the error bars denote $\pm 2s/\sqrt{n}$. and 3.8.

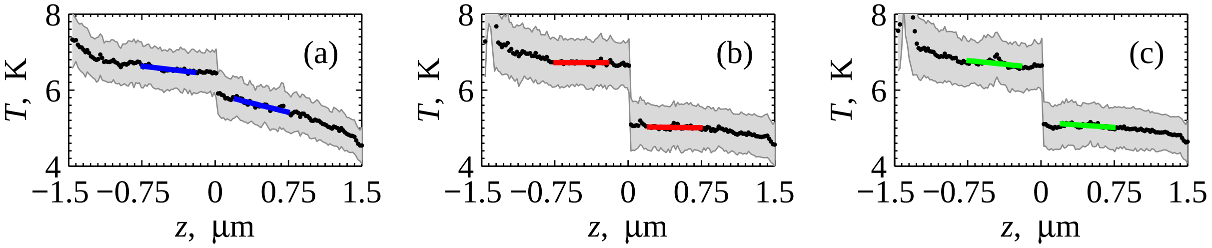

Figure 3.6: Steady-state temperature profiles in one-dimensional systems at $T_{\text{nominal}} = 6$ K with (a) all LJ bonds, (b) all harmonic bonds, and (c) all harmonic bonds except a single LJ bond at the interface.

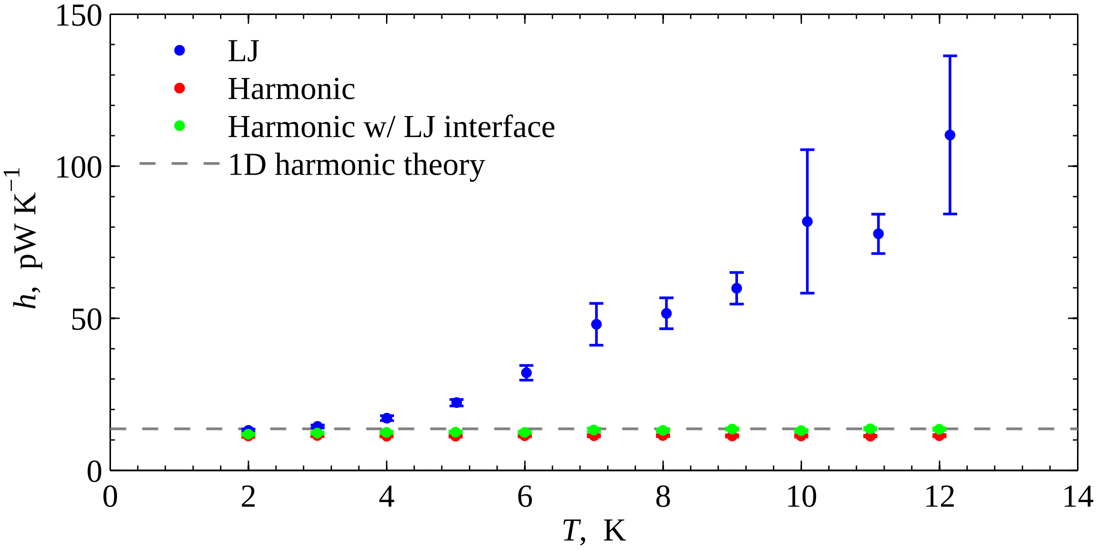

Figure 3.7: The thermal conductance $h(T)$ between one-dimensional Ar and heavy Ar.

that $n_{\mathbf{q},\nu} \to n_{\text{B–E}}(\omega_{\mathbf{q},\nu}, T)$ and that scattering is elastic. In a one-dimesional, classical system, this gives [25]

$$h = \frac{k_{\mathrm{B}}}{2\pi} \int_0^{\infty} \alpha(\omega)\, d\omega, \tag{3.7}$$

where the transmissivity as a function of phonon frequency, $\alpha(\omega)$, is given by Eq. 4.5. Despite the crude assumptions, the model agrees well with the conductance values calculated in the harmonic system, both in magnitude and in the lack of temperature dependence.

3.2.2 In three dimensions

Likewise, three temperature profiles collected in three-dimensional systems at $T_{\text{nominal}} = 30$ K are shown in Figure 3.8. They are qualitatively similar to the one-dimensional temperature profiles, except that the conductance in case (c) is significantly larger than case (b), although still not nearly as large as in case (a).

These simulations are repeated across a range of nominal temperatures from $T = 2$ to 50 K, in increments of 4 K, to collect the data displayed in Figure 3.9. Each data point is the mean of $n = 10$ simulations, and the error bars denote $\pm 2s/\sqrt{n}$. The qualitative results are similar to those of the one-dimensional simulations, although h appears to take a different functional dependence on T.

3.3 Discussion

The results, both in the one- and three-dimensional systems, are consistent with hypotheses that elevated conductance at high temperatures arises due to some type of inelastic phonon processes, as enabled by anharmonic forces. However, they indicate that accounting for inelastic transmission in the phonon transmissivity (Section 2.4.1) is unlikely to explain $h(T)$.

Rather, they suggest that accounting for inelastic effects on the phonon distribution (Section 2.4.2) is likely more important. However, these results do not provide enough

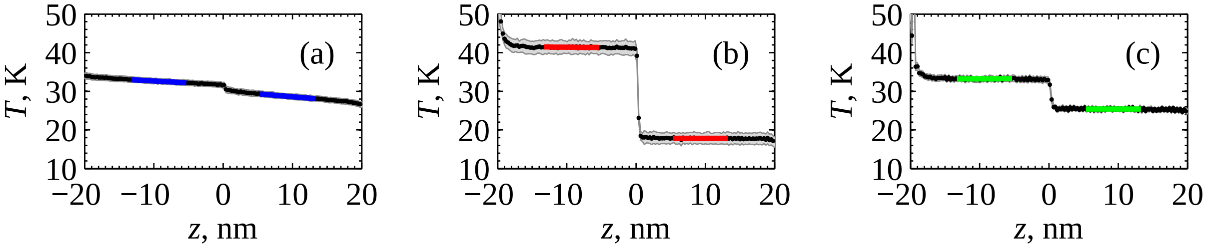

Figure 3.8: Steady-state temperature profiles in three-dimensional systems at $T_{\text{nominal}} = 30$ K with (a) all LJ bonds, (b) all harmonic bonds, and (c) all harmonic bonds except a single LJ bond at the interface.

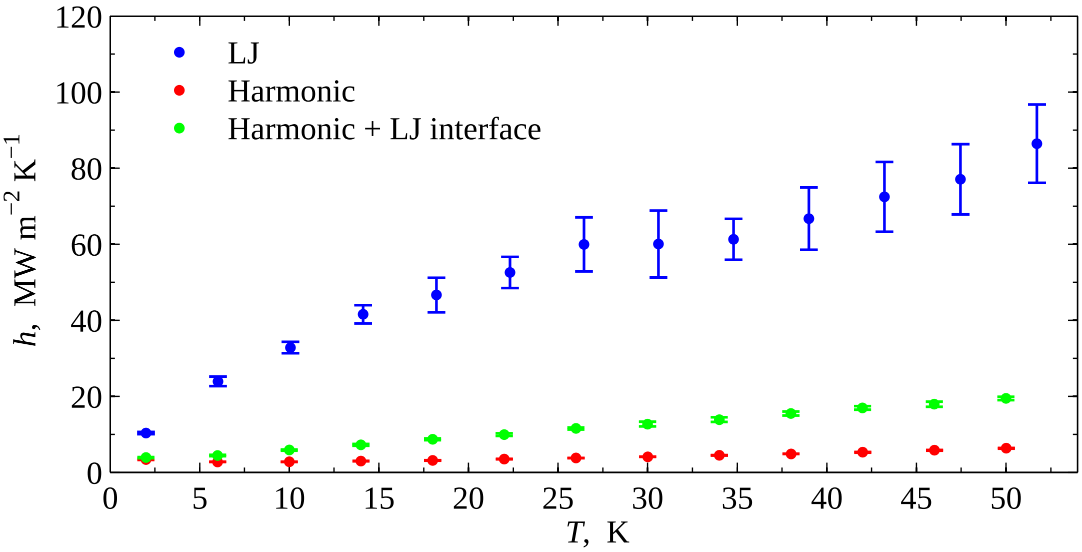

Figure 3.9: The thermal conductance $h(T)$ in three-dimensional Ar and heavy Ar.

information to distinguish between the two types of models presented in that section: (1) the heat flux effect and (2) the interfacial boundary condition effect. These conclusions are based on the following observations:

- Having anharmonicity throughout the system raises the conductance significantly in both one- and three-dimensional systems. Having anharmonicity at only the interface also raises conductance, but only slightly. This lends support to models incorporating inelastic processes not only at the interface itself, but in some nearby region as well.

- Unfortunately, as mentioned in Section 3.1, the algorithm used to enforce the heat current does not produce a known energy spectrum. In addition, the energy spectrum calculated using Equation 3.3 cannot distinguish between left-traveling and right-traveling modes, making it difficult to assess the models for the flux-induced non-equilibrium distribution proposed by Simons [26] and others.

- Figure 3.4 also suggests that an interface-induced non-equilibrium distribution persists into the bulk argon material. This is due to the ballistic transport in the harmonic system, consistent with the slight non-equilibrium energy distribution suggested in Figure 3.4.

In Chapter 4, I present results to assess the first point in more detail, while in Chapter 5 I present results that help to further distinguish between the second and third.

Chapter 4

Effects of Anharmonicity on Phonon Transmission

Chapter 3 presented the effect of anharmonicity on the macroscopic heat transfer at an interface, as captured in the thermal conductance $h(T)$. The macroscopic effects observed in that chapter must be explained by some microscopic phenomena. The theory established in Section 2.4 provides a list of phononic quantities that could be responsible, of which the two likely candidates are the transmissivity $\alpha_{\mathbf{q},\nu}$ and the distribution $n_{\mathbf{q},\nu}$. In this chapter, I present results assessing the effect of anharmonicity on $\alpha_{\mathbf{q},\nu}$, and in doing so I also consider the potential effect on $h(T)$. I calculate $\alpha_{\mathbf{q},\nu}$ using the wave packet method, described in Section 4.1. I present the results in Section 4.2, and I discuss their implications in Section 4.3. The effect of anharmonicity is to enable transmission into modes of different frequency (inelastic processes), but the net transmissivity decreases, contrary to my expectation. Therefore, it appears that an increase in transmission is unlikely to be the sole mechanism by which anharmonicity increases $h(T)$.

4.1 The wave packet method

Wave packet simulations are the computational analogue of "phonon-pulse experiments," which are described in Section III.C.1 of Ref. [35]. Given a sample structure consisting of an interface between two phases, energy is deposited into a narrow band of normal modes in one of the materials and allowed to propagate and refract through the interface. The fraction of energy that successfully passes through the interface provides an aggregate transmissivity of the initial band of normal modes.

4.1.1 Methodology

By convention I orient the systems so that the wave packet originates in the "left" material and transmits into the "right" material. The wave packet simulations are similar in geometry to the NEMD simulations, except with different lengths of each material. In the 1D simulations, the domain consists of 2800 Ar atoms and 2000 heavy Ar atoms, for a total length of about 1.28 μm. In the 3D simulations, the domain consists of 30 × 30 × 40 unit cells of Ar (144 000 atoms) abutting with 30 × 30 × 20 unit cells of heavy Ar (72 000 atoms). The large 3D domain is necessary for simulations of wave packets at non-normal incidence angles, as shown in Section 4.2.2.

I essentially follow the method described by Schelling *et al.* [117] and those who later generalized the method to non-normal incidence [64, 74, 118, 119]. The process can be broken into three parts: (1) system initialization with energy concentrated about a single normal mode, (2) simulation of the partial reflection/transmission event, and (3) data collection.

1. Each simulation begins with energy concentrated about a particular normal mode $(\mathbf{q}_0, \nu_0)$ in reciprocal space and about a spatial location $\mathbf{r}_0$ in the left material. To do so, atoms are given an initial displacement from their equilibrium positions $\mathbf{r}_{\text{eq}}$, such

that the position of the j^{th} basis atom in the l^{th} unit cell is

$$\mathbf{r}_{j,l}(t_{\text{initial}}) = \mathbf{r}_{j,l,\text{eq}} + \text{Re}\left\{ \frac{B}{\omega_{\mathbf{q}_0,\nu_0}} \mathbf{e}_{\mathbf{q}_0,\nu_0,j} \exp\left[i\left(\mathbf{q}_0 \cdot \mathbf{r}_{j,l,\text{eq}} - \omega_{\mathbf{q}_0,\nu_0} t_{\text{initial}}\right)\right] \exp\left(-\frac{|\mathbf{r}_{j,l} - \mathbf{r}_0|^2}{\eta^2}\right)\right\}, \tag{4.1}$$

where the wave packet amplitude is $B\omega^{-1}$, and its characteristic width is η. See Section 2.2 for explanation of the other quantities. The initial velocities are therefore

$$\mathbf{v}_{j,l}(t_{\text{initial}}) = \frac{d\mathbf{r}_{j,l}(t_{\text{initial}})}{dt} = \text{Re}\left\{-i\omega_{\mathbf{q}_0,\nu_0}\left[\mathbf{r}_{j,l}(t_{\text{initial}}) - \mathbf{r}_{j,l,\text{eq}}\right]\right\}. \tag{4.2}$$

2. The molecular dynamics simulation proceeds according to the rules of Section 2.1.1. If the initial conditions were set correctly, the wave packet propagates naturally at its group velocity toward the interface and partially transmits. The simulation should end when the transmitted and reflected packets have completely left the interface.

3. The energy on each side, and therefore the transmissivity, can be calculated directly from the atomic positions and velocities.

Ideally, the initial packet is composed of a narrow band of modes, in which case we assign the resulting transmissivity to the central mode $(\mathbf{q}_0, \nu_0)$. The width of the initial packet in q-space therefore leads to an uncertainty in assigning $\alpha_{\mathbf{q}_0,\nu_0,1\to2}$.

I note that previous works have used a version of Eq. 4.1 where the maximum displacement is not divided by the frequency; i.e., having a prefactor of just B instead of $B\omega^{-1}$. I use the latter because it ensures that packets of equal B correspond to the same energy, and can therefore be associated with normal mode vibrations of the same temperature in a system at thermal equilibrium. This distinction is irrelevant in the harmonic (i.e., small-amplitude) limit, as has been simulated in Refs. [64, 74, 117–119]. In this case, the transmission is linear; i.e., it does not depend on amplitude. However, the distinction is important in this work, since I am interested in anharmonic processes that are inherently non-linear: inelastic transmission that depends on vibrational amplitude.

Therefore, I seek to associate with each value B a (roughly) equivalent temperature T_{equiv}. From Eq. 4.2, the value of B corresponds to the maximum velocity of any atom in the wave packet. A plane wave of that amplitude has a root-mean-square value of $B/\sqrt{2}$, which I equate to the root-mean square velocity of an atom in a system at thermal equilibrium at temperature T:

$$\frac{B}{\sqrt{2}} \sim \sqrt{\frac{dk_{\mathrm{B}}T}{m}}. \tag{4.3}$$

Based on this relation, a reasonable definition of an equivalent temperature is

$$T_{\text{equiv}} \equiv \frac{mB^2}{2dk_{\mathrm{B}}}. \tag{4.4}$$

In interpreting the following results, I use Eq. 4.4 to provide an approximate connection between wave packet amplitudes and the NEMD simulations of Chapter 3.

4.1.2 Verification

I verify the method by first performing simulations in one-dimensional systems with harmonic bonds only. In such systems, the transmissivity can be calculated analytically [120]:

$$\alpha_{1\to 2}(\omega) = \frac{4\Gamma_1\Gamma_2}{(\Gamma_1+\Gamma_2)^2 + \omega^4(m_1-m_2)^2}, \tag{4.5}$$

where

$$\Gamma_i = 2\omega\sqrt{m_i k - \frac{m_i^2\omega^2}{4}}, \tag{4.6}$$

where k is the harmonic force constant. In the following, I show that transmissivities calculated using the wave packet method are consistent with those calculated using Eq. 4.5.

The trajectories of two wave packet simulations in 1D, harmonic systems are shown in Fig. 4.1: (a) one starting in Ar with $q_0 = 0.3\,q_{\max}$ and (b) the second starting in heavy Ar

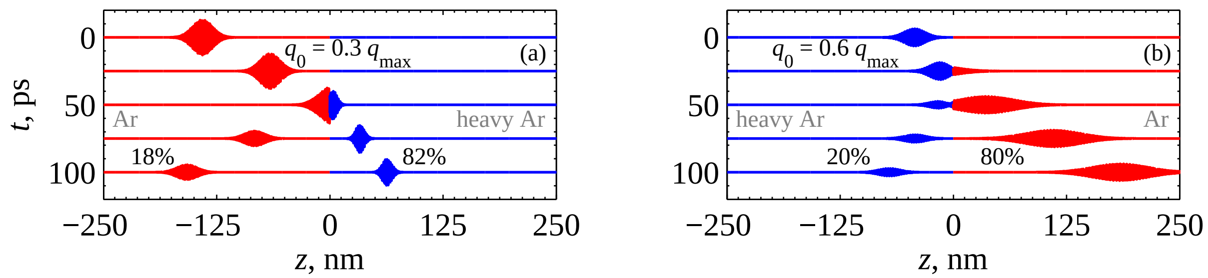

Figure 4.1: Snapshots of atomic velocities $v(z, t)$ in two wave packet simulations with all harmonic forces and the percentages of reflected and transmitted energy. (a) Ar to heavy Ar, $q_0 = 0.3\, q_{\max}$. (b) Heavy Ar to Ar, $q_0 = 0.6\, q_{\max}$. The initial amplitudes are given in the text.

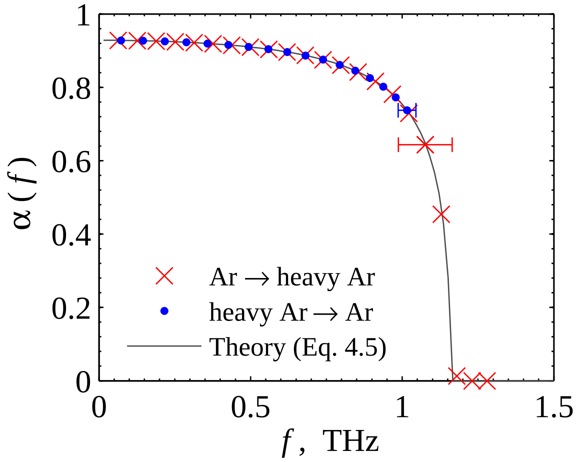

Figure 4.2: Transmissivity of normal modes as a function of their frequency in systems with harmonic forces throughout. For clarity, the uncertainty is only shown for one point in each data series.

with $q_0 = 0.6\, q_{\max}$, where $q_{\max} = \frac{2\pi}{a}$. The width of all packets is $\eta = 30a$, and the amplitudes in both simulations correspond to $T_{\text{equiv}} = 2$ K: (a) $B = 0.288$ Å/ps and (b) $B = 0.166$ Å/ps. Each plot provides five snapshots of the velocities v_i of atoms i within 250 nm of the interface at intervals of 25 ps. After 100 ps, the reflected and transmitted packets have completely left the interface, and the ratios of reflected and transmitted energy are calculated.

To test the methodology, I ran 38 simulations (22 starting in Ar, 16 in heavy Ar) similar to those shown in Fig. 4.1 at different wavenumbers and compiled the transmissivity values. The results are plotted as a function of normal mode frequency, $\alpha_{q,i\to j}(\omega_q)$, in Fig. 4.2, along with the prediction of Eq. 4.5.[1] The dominant uncertainty arises from assigning the transmissivity to the nominal wavenumber q, despite the wavepacket containing components from a band of wavenumbers of characteristic width $2\pi/\eta$. The corresponding frequency range is marked by error bars for two representative points. The data agree very well with Eq. 4.5, and I am satisfied that this implementation of the wave packet method produces correct results.

Finally, I also verify the assertion that only elastic (frequency-preserving) scattering is possible in a system with only harmonic forces. For each simulation from Ar to heavy Ar—i.e., the red crosses in Fig. 4.2—I determine the spectra of energy transmitted, $\alpha(\omega_0, \omega')$, and reflected, $\beta(\omega_0, \omega')$, from an initial frequency ω_0 into a final frequency ω'. The initial frequency in each simulation is known from the initial wavenumber, and the spectrum of final frequencies is obtained by Fourier transform of the final velocities. Specifically, I use the final atomic velocities as a spatial signal $v_i(t_{\text{final}}) = v_{\text{final}}(z)$, which is related to the spectrum of kinetic energy in the final system, $E^{\text{K}}_{q_0}(q') = E^{\text{K}}(q_0, q')$, by a Fourier transform in z:

$$E^{\text{K}}(q_0, q') = \left| \mathcal{F} \left\{ \sqrt{\frac{m(z)}{2}}\, v_{\text{final}}(z) \right\} \right|^2, \tag{4.7}$$

where the atomic masses have also been converted to a spatial signal, $m_i = m(z)$. Parseval's theorem ensures that the total energy in the spectrum is equal to the total kinetic energy in the system:

$$E^{\text{K}}(q_0) = \int E^{\text{K}}(q_0, q')\, dq' = \frac{1}{2} \sum_i^N m_i v_i^2. \tag{4.8}$$

By including only atoms of one material, one can also obtain the spectra of only the energy that has been reflected back into material 1 or transmitted into material 2:

---

[1] Throughout this work, I follow the common convention of using angular frequency ω in developing theory but linear frequency f in reporting actual values.

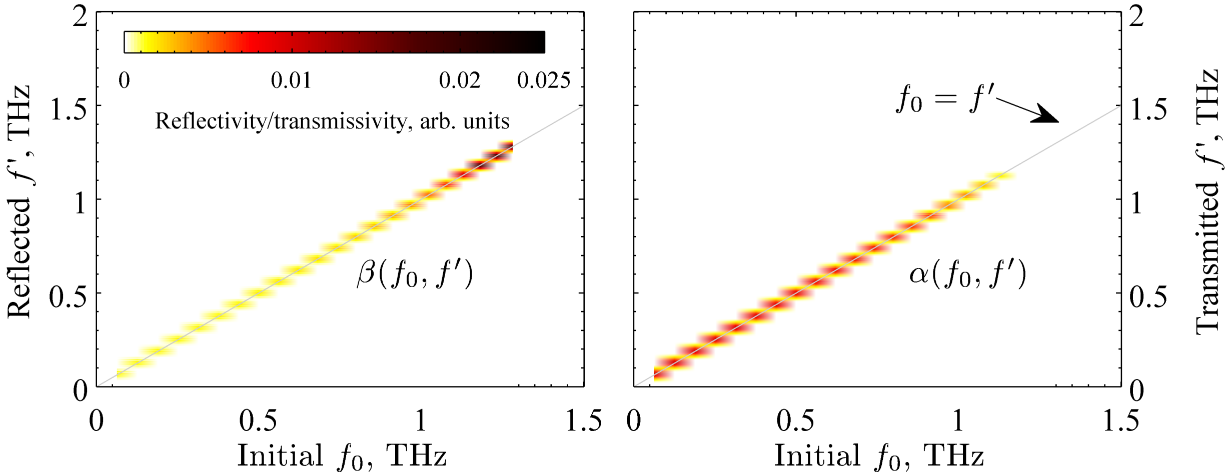

Figure 4.3: Reflectivity and transmissivity of modes from initial frequency f_0 into final frequency f' in the Ar/heavy Ar system with harmonic forces throughout.

$$E_1^{\mathrm{K}}(q_0, q') = \left| \mathcal{F}\left\{ \sqrt{\frac{m(z<0)}{2}}\, v_{\mathrm{final}}(z<0) \right\} \right|^2 \text{ and} \tag{4.9}$$

$$E_2^{\mathrm{K}}(q_0, q') = \left| \mathcal{F}\left\{ \sqrt{\frac{m(z>0)}{2}}\, v_{\mathrm{final}}(z>0) \right\} \right|^2 . \tag{4.10}$$

In terms of these quantities, I define the reflectivity and transmissivity spectra as

$$\beta(q_0, q') = \frac{E_1^{\mathrm{K}}(q_0, q')}{E^{\mathrm{K}}(q_0)} \quad \text{and} \quad \alpha(q_0, q') = \frac{E_2^{\mathrm{K}}(q_0, q')}{E^{\mathrm{K}}(q_0)}, \tag{4.11}$$

respectively. To evaluate the extent of elastic and inelastic processes, these are readily converted to frequency space by using the dispersion relation, Eq. 2.16.

Thus I plot $\beta(\omega_0, \omega')$ and $\alpha(\omega_0, \omega')$ in Fig. 4.3. The plots show that, in each simulation, all of the energy is reflected and transmitted into the same frequency ω' as the initial frequency ω_0 (within the uncertainty due to the finite packet broadness). This confirms the expectation that only elastic transmission occurs in a harmonic system.

4.2 Results: Phonon transmission spectra

To test the hypotheses that thermal conductance increases at high temperature due to additional transmission via inelastic scattering [38, 39, 67, 68], I now use this simulation scheme to calculate $\alpha(\omega_0, \omega')$ at interfaces with anharmonicity. In both one- and three-dimensional systems, I report the transmissivity spectra in systems with all harmonic bonds except between the two atoms (1D) or atomic planes (3D) immediately adjacent to the interface, which interact through the LJ potential. These systems correspond to the systems in which I presented NEMD simulations of conductance in case (c) of Section 3.2. Varying the amplitude of the wave packet provides insight into interfacial transmission in systems at different temperatures, as captured roughly by the equivalent temperature defined in Eq. 4.4.

4.2.1 In one dimension

From the arguments of Chapters 1 and 2, one expects that adding anharmonicity to the forces at the interface should enable inelastic reflection and transmission processes. Therefore I perform simulations in the same 1D, harmonic systems as in Section 4.1.2, except that I use the LJ potential to describe the interactions between the two atoms at the interface. Figure 4.4 shows snapshots of $v_i(t)$ from two $q = 0.3\, q_{\max}$ packets originating in Ar with different amplitudes, corresponding to (a) $B = 0.288$ Å/ps ($T_{\text{equiv}} = 2$ K) and (b) $B = 0.706$ Å/ps (12 K). On each plot, the fraction of energy reflected/transmitted in each mode is noted next to the corresponding packet in the signal at $t = 100$ ps.

I make two observations. First, there is a new reflected packet that was not present in the all-harmonic system (Fig. 4.1a). The packet evidently has a slower group velocity, indicating that it has a higher frequency. This confirms that the anharmonic forces at the interface have enabled an inelastic process. Second, the reflectivity and transmissivity now change with amplitude, consistent with the fact that the inelastic process is non-linear. As expected, the

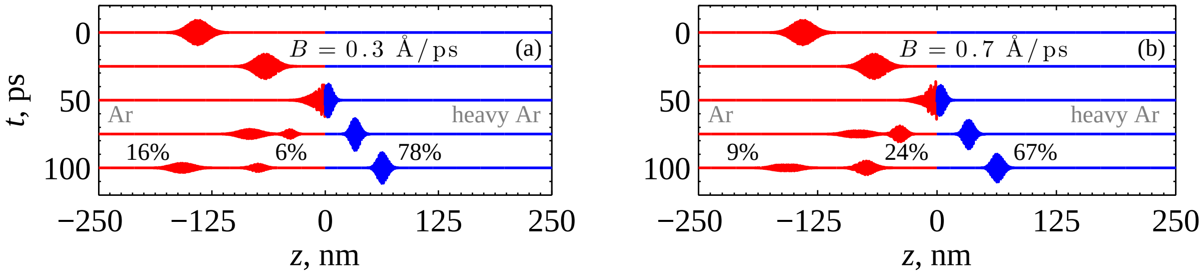

Figure 4.4: Snapshots of atomic velocities $v(z,t)$ in two wave packet simulations with LJ forces at the interface: (a) $T_{\text{equiv}} = 2$ K and (b) $T_{\text{equiv}} = 12$ K.

rate of the inelastic process increases with amplitude. However, somewhat surprisingly, the total transmissivity decreases.

I repeat these simulations across the same range of wavevectors as used in the harmonic system in Section 4.1.2. In each simulation, I associate the initial frequency ω_0 with the final spectra of reflected and transmitted energy in ω', which produces the reflectivity and transmissivity spectra plotted in Fig. 4.5 for Ar → heavy Ar and in Fig. 4.6 for heavy Ar → Ar. For the packets originating in Ar, the anharmonicity at the interface enables energy transfer into *reflected* modes of frequency $\omega' = 2\omega_0$, and even some into modes of frequency $\omega' = 3\omega_0$. However, there is no appreciable energy transfer into *transmitted* modes of different frequency. On the other hand, for packets originating in heavy Ar, I observe negligible energy transfer into any frequencies $\omega' \neq \omega_0$. The only detectable inelastic energy transfer is some faint transmission into modes of frequencies $\omega' = 2\omega_0$ in the range of $\omega' \sim 0.6$–0.8 THz in Fig. 4.6d.

In both cases, the net effect of anharmonicity at the interface is to *decrease* the transmissivity, albeit only slightly in the direction of heavy Ar → Ar. The effect of inelastic scattering is evidently much more pronounced for packets originating in Ar than those originating in heavy Ar. I attribute this to the fact that, for the same equivalent temperature, the heavy Ar atoms experience a smaller displacement, inversely proportional to the square root of their mass [93]. The heavy Ar must therefore be raised to a higher equivalent temperature before the constituent atoms experience the same anharmonicity.

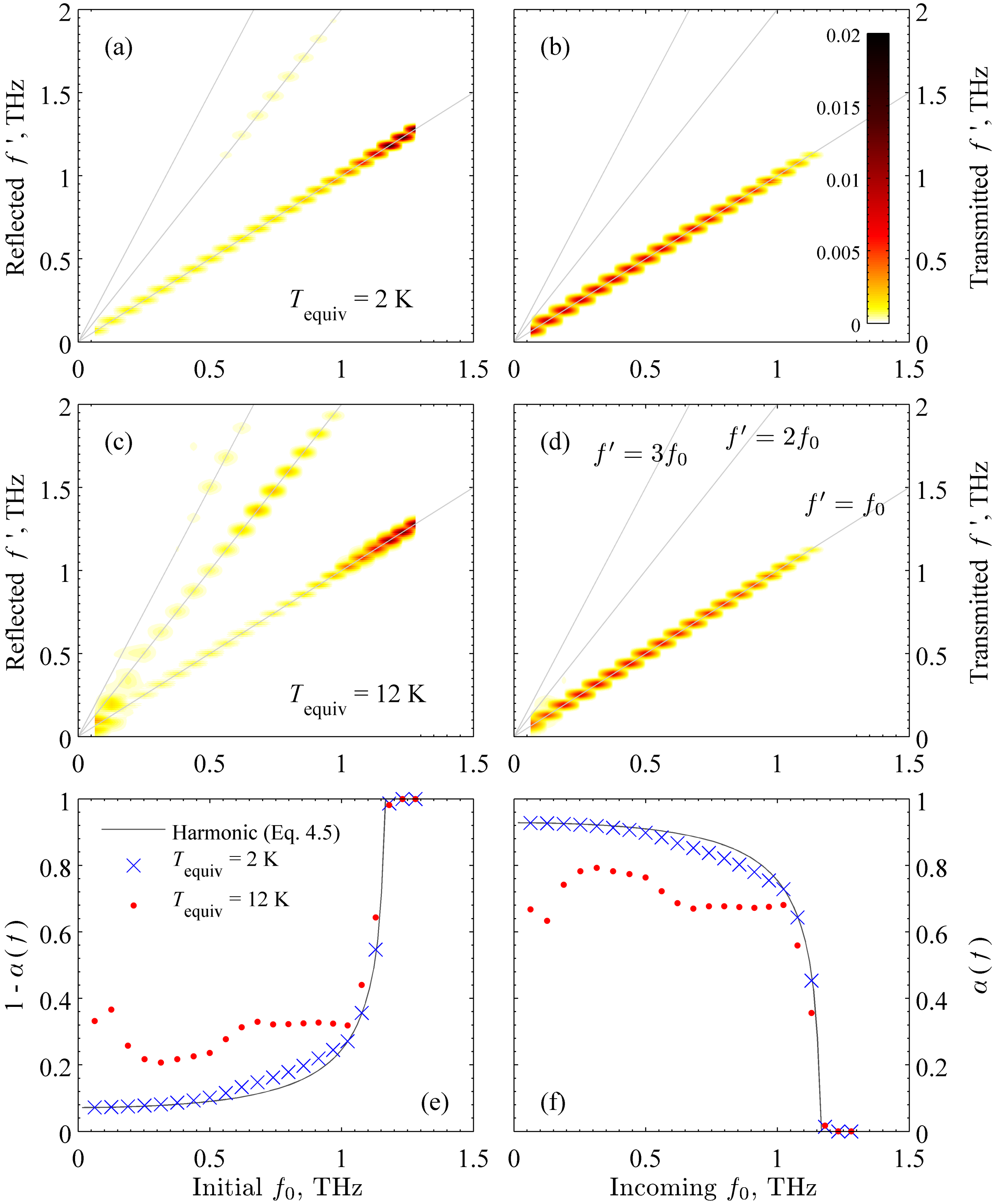

Figure 4.5: Energy reflection and transmission spectra from Ar to heavy Ar with LJ forces at the interface. (a) Reflection and (b) transmission spectra with amplitude corresponding to $T_{\text{equiv}} = 2$ K, (c,d) the same with $T_{\text{equiv}} = 12$ K, and (e) the total reflectivity and (f) total transmissivity at both amplitudes.

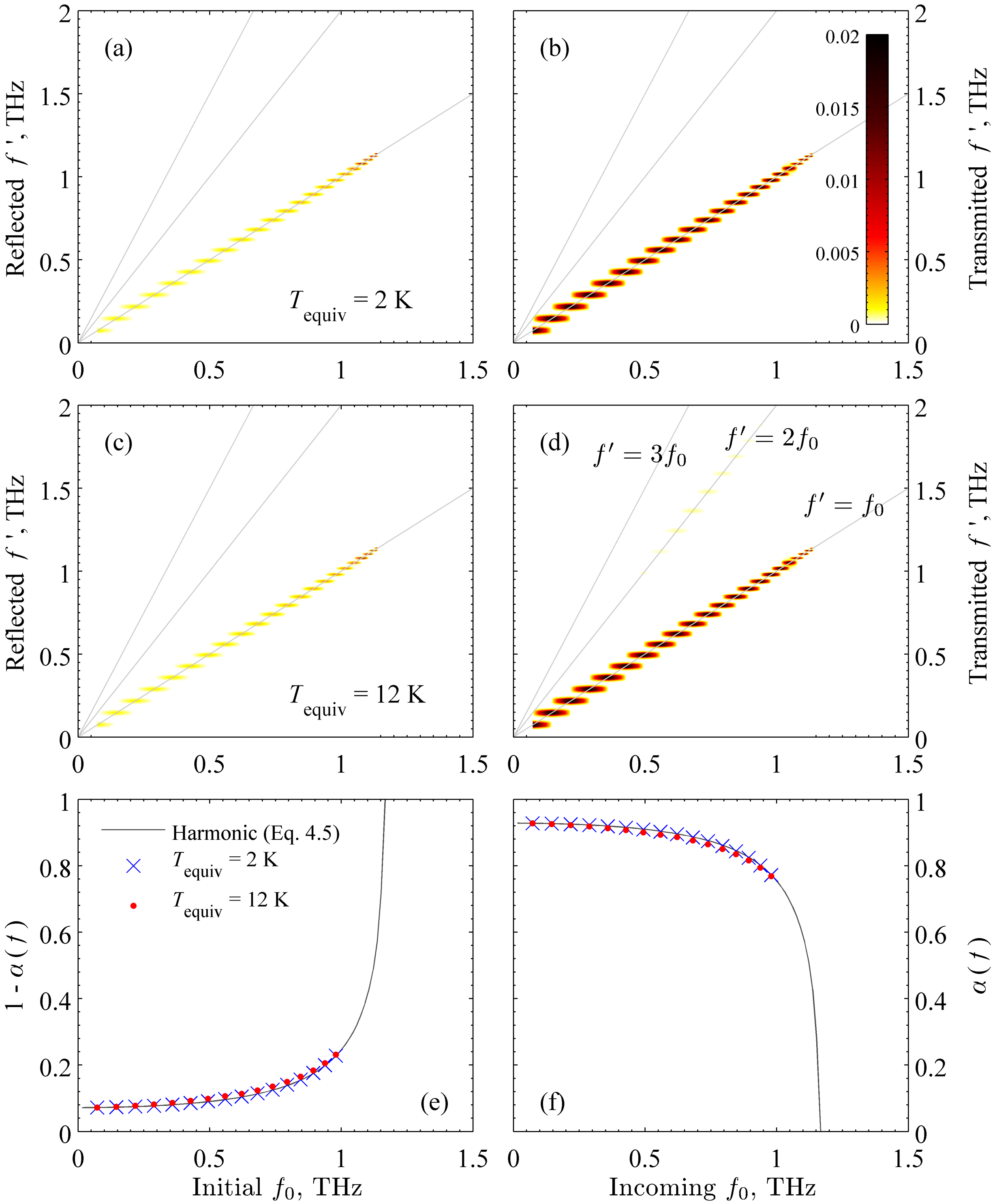

Figure 4.6: Same as Fig. 4.5, but from heavy Ar to Ar.

4.2.2 In three dimensions

The insights from the one-dimensional simulations may not necessarily be transferable to three-dimensional systems. In this section, I present results to help determine whether the observation that interfacial anharmonicity reduces transmissivity in 1D systems also holds in 3D systems, where the additional dimensionality allows more possibilites for mode coupling [111]. To that end, I performed simulations of wave packets at non-normal incidence in three-dimensional systems. In Fig. 4.7, I show the x-components of atomic velocities during simulations of a wave packet with a wavevector of

$$\mathbf{q}_0 = 0.3\,\mathbf{q}_{\text{max},[013]} = 0.3\left(\frac{2\pi}{3a}\mathbf{y} + \frac{2\pi}{a}\mathbf{z}\right), \tag{4.12}$$

where $\mathbf{q}_{\text{max},[013]}$ is the maximum wavevector in the [013] direction. Snapshots (a)–(c) show the transmission event in a system with all harmonic forces, while snapshots (d)–(f) are from a system that is harmonic but with LJ forces at the interface. Only the velocities of atoms in the (200) monolayer bisecting the wave packet are shown. I used GULP to calculate the three polarization vectors, and I chose one of the transverse-like modes:

$$\mathbf{e}_{\mathbf{q}_0,\nu_0} = -0.876608\,\mathbf{x} + 0.481205i\,\mathbf{y}. \tag{4.13}$$

In both packets I used the same maximum velocity of $B = 1.44$ Å/ps, corresponding to $T_{\text{equiv}} = 50$ K. I calculated $\alpha_{\mathbf{q}_0,\nu_0}$ for each simulation, which is marked in plots (c) and (f). As in the 1D simulations, the transmissivity is lower in the system with anharmonic forces at the interface. However, no new mode is identifiable in plot (f).

I repeated these simulations for the range of wavenumbers $\mathbf{q}_0 = [0.1, 0.2, 0.3, 0.35]\,\mathbf{q}_{\text{max},[013]}$ and a range of amplitudes corresponding to $T_{\text{equiv}} = [10, 30, 50]$ K. The resulting transmissivity values are listed in Table 4.1. In general, the behavior of $\alpha_{\mathbf{q}_0,\nu}$ in 3D looks similar to the behavior in 1D. As a function of wavenumber, the transmissivity is high and flat at low q_0, and it decreases sharply and monotonically as $q_0/q_{\text{max},[013]}$ approaches 0.4, at which point the

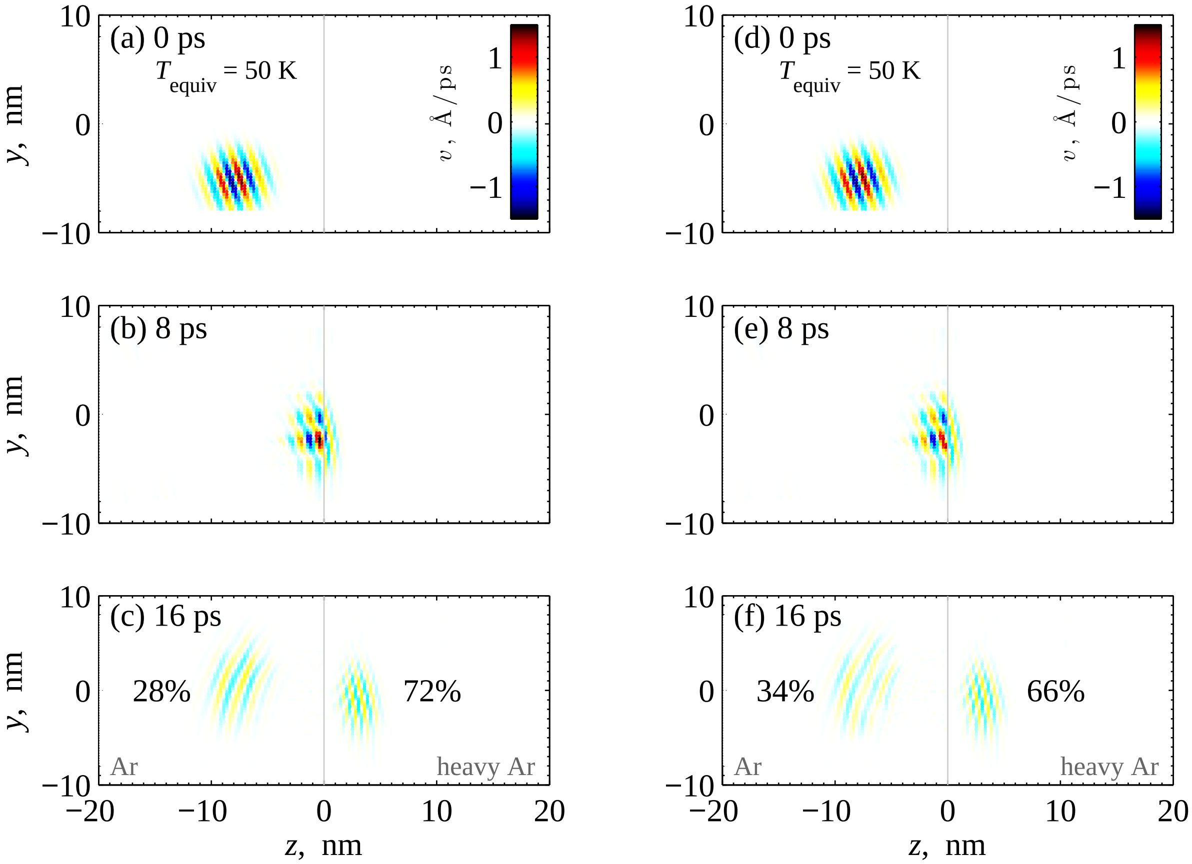

Figure 4.7: x-components of atomic velocities during simulations of wave packets at non-normal incidence. The systems are three-dimensional with (a–c) all harmonic forces and (d–f) LJ bonds at the interface.

Table 4.1: Transmissivity Values from 3D Wave Packet Simulations

	$\alpha_{\mathbf{q_0},\nu}$			
$q_0/q_{\text{max},[013]}$	harmonic	10 K	30 K	50 K
0.10	0.86	0.86	0.86	0.86
0.20	0.86	0.86	0.85	0.85
0.30	0.72	0.71	0.70	0.66
0.35	0.44	0.43	0.42	0.39

frequency in Ar surpasses the maximum frequency in heavy Ar. As a function of amplitude, the transmissivity is practically independent of T_{equiv} for low-q_0 modes, but decreases slightly with T_{equiv} for high-q_0 modes. The preferential effect on high-q_0 modes is consistent with the fact that the anharmonicity is localized spatially to the interface, therefore most strongly affecting vibrations with short wavelengths.

4.3 Discussion

The results in both one- and three-dimensional systems confirm that anharmonicity in the atomic forces enables inelastic scattering processes at an interface. Those processes allow energy coupling among modes of different frequency, and the rate of the energy transfer does increase with the amplitude of the incident vibration. However, in all cases examined here, the inelastic processes increase energy transfer to *reflected* modes, even in cases of inelastic *transmission* (Fig. 4.6), thereby decreasing the total transmissivity with increasing amplitude. Therefore, the results do not support the hypothesis that elevated conductance at high temperature arises due to increased transmissivity via inelastic phonon processes.

These conclusions provide interesting insight in the context of recent literature. As described in Sections 1.3.4 and 2.4.1, the opening of "inelastic channels" at high temperatures is the primary explanation for experimental conductance measurements far in excess of the AMM and DMM [38, 39, 67, 68]. Recently, Sääskilahti *et al.* [85] showed that inelastic processes do indeed occur at the interface during NEMD simulations, and furthermore that frequency-doubling and frequency-halving processes are dominant. This is consistent with the results of Section 4.2. However, they show that inelastic processes *do* significantly enhance conductance, in apparent contradiction with my conclusions. In order to reconcile our findings, a comparison should be made between the single-mode transmission picture in my work and their inelastic conductance spectrum $g^{\text{inel}}(\omega, \omega')$ calculated during an actual NEMD simulation. As shown by the work of Kimmer *et al.* [64] and Aubry *et al.* [74], our existing theories of conductance are not yet mature enough to provide a quantitative connection between the transmission of isolated modes and the conductance of a thermal energy distribution.

In comparing the two pictures, one important difference is that the wave packet simulations of this chapter occur at "zero temperature" aside from the energy in the packet itself: the rest of the crystal is in its equilibrium state. Therefore, the energy propagating in the wave packet does not experience the same environment that it would during a thermal transport scenario. It is possible, then, that there are additional scattering processes which would occur during a full NEMD simulation, but which are suppressed during the wave packet simulation. This is a shortcoming of the wave packet approach. However, I am not aware of an alternative method to obtain the per-mode transmissivities $\alpha_{\mathbf{q}_0,\nu_0}$, as are desired for predictive conductance models, during simulations at (or near) thermal equilibrium. Furthermore, the shortcoming of the wave packet model does not detract from the conductance calculations of Chapter 3, which also suggest the same conclusion: that inelastic processes at the interface itself may not contribute much to the total conductance. In those simulations, energy occupies the normal modes in a near-equilibrium distribution (Section 3.1.2), and would presumably undergo any processes that may not be observable in the present wave packet simulations. However, the resulting conductance values are still much lower that the conductances calculated in the systems with all LJ forces.

That being said, other recent computational work does corroborate the conclusion that inelastic processes at the interface might play a smaller role than expected. Wu and Luo [83] performed NEMD simulations while varying the third-order force constants in the bulk and at the interface. The conductance increased significantly with anharmonicity in the bulk, but did not change measurably with anharmonicity at the interface. Similarly, Murakami *et al.* [84] used both equilibrium MD and NEMD to show that the conductance is dominated by inelastic scattering not at the interface itself, but in a "transition region" near the interface in which scattered phonons rethermalize. This is related to the other commonly-mentioned explanation for excess thermal conductance: the non-equilibrium distribution of phonons, as introduced in Section 2.4.2 and investigated further in Chapter 5.

Chapter 5

Effects of Anharmonicity on Phonon Distribution

Between the transmissivity $\alpha_{\mathbf{q},\nu}$ and the distribution $n_{\mathbf{q},\nu}$, the two phononic quantities suspected to be responsible for the thermal conductance trends calculated in Chapter 3, the results of Chapter 4 suggest that $\alpha_{\mathbf{q},\nu}$ alone is unlikely to explain $h(T)$. In this chapter, I present results assessing the effect of anharmonicity on $n_{\mathbf{q},\nu}$. As the classical proxy for $n_{\mathbf{q},\nu}$, I calculate the spatial variation of the energy per mode, $E_{\mathbf{q},\nu}(z) = \hbar\omega\, n_{\mathbf{q},\nu}$, using the wavelet transform, described in Section 5.1. I present calculations of $E_{\mathbf{q},\nu}(z)$ during 1D and 3D NEMD simulations in Section 5.2. In order to interpret the energy distributions, I also calculate the mode relaxation times $\tau_{\mathbf{q},\nu}$ in Ar and heavy Ar using the method of normal mode decomposition, described in Section 5.3. I present those relaxation times in Section 5.4, along with the corresponding mean free paths. Finally, in Section 5.5, I discuss a hypothesis to explain the conductance at high temperatures that is best supported by the available facts.

5.1 The wavelet transform

There are multiple options for analysis tools with which one can obtain the energy per mode, $E_{\mathbf{q},\nu}$. In particular, I seek to analyze the energy per mode in the NEMD simulations of

Chapter 3, which are not in thermal equilibrium, so it is useful to consider the spatial variation of the energy per mode: $E_{\mathbf{q},\nu}(z)$. Therefore, I choose the wavelet transform as my primary analysis tool, as implemented for MD by Baker *et al.* [121], precisely because the wavelet spectrum $\tilde{w}(z,q)$[1] of a signal $w(z)$ preserves information in both z and q. If, for example, $w(z)$ represents snapshots of atomic velocities during an NEMD simulation, then one can directly convert $\tilde{w}(z,q)$ to $E_{\mathbf{q},\nu}(z)$. In contrast, the spatial Fourier transform $\bar{w}(q)$ of $w(z)$ completely encodes any spatial variation into the amplitudes and phases of the plane-wave basis, making the z-dependence non-transparent. Another option to obtain $E_{\mathbf{q},\nu}(z)$ would be start with the atomic velocities over time, $w(t,z)$, and obtain the temporal Fourier transform, $\bar{w}(\omega,z)$. One could then convert $\bar{w}(\omega,z)$ to the spatial variation of energy per frequency, $E(\omega,z)$. However, extracting $E_{\mathbf{q},\nu}(z)$ from $E(\omega,z)$ is difficult, since the analysis in the time and frequency domains does not distinguish among different normal modes with the same frequency.

5.1.1 Methodology

The wavelet transform $\tilde{w}(q,z)$ of a signal $w(z)$ takes the same form as other integral transforms, such as the Fourier and Laplace transforms:

$$\tilde{w}(z',q') = \mathcal{W}\{w(z)\} = \int_{-\infty}^{\infty} w(z)\,\psi^*_{z',q'}(z)\,dz. \tag{5.1}$$

The difference lies in the kernel functions $\psi_{z',q'}$. Different definitions of wavelet-type kernel functions are possible. I follow the convention of Baker *et al.* [121] in which each "daughter wavelet," corresponding to a specific location z' and wavenumber q', is defined as

$$\psi_{z',q'}(z) = \pi^{-1/4}\left(\frac{q'}{q_0}\right)^{1/2} \exp\left[iq'(z-z')\right]\, \exp\left[-\frac{1}{2}\left(\frac{q'}{q_0}\right)^2 (z-z')^2\right], \tag{5.2}$$

---

[1] Given a signal $w(z)$, I write its wavelet transform with a tilde and its Fourier transform with a bar.

which is a scaled and translated version of a "mother wavelet" ψ_{z',q_0} whose dominant wavenumber is q_0. This definition is normalized so that the energy density per length, per wavenumber is conveniently calculated as

$$E_\psi(z', q') = \frac{1}{Cq_0}|\tilde{w}(z', q')|^2. \tag{5.3}$$

The constant C accounts for the fact that, unlike the plane waves that form the basis functions for the Fourier transform, the wavelets are not orthogonal:

$$C = \int_{-\infty}^{\infty} \frac{|\bar{\psi}_{z',q_0}(q)|^2}{|q|} dq, \tag{5.4}$$

where $\bar{\psi}_{z',q'_0}(q)$ is the Fourier spectrum of the mother wavelet $\psi_{z',q_0}(z)$. Equations 5.1–5.4 suffice to discuss the results of this chapter. For additional details on practical implementation of the transform, refer to Refs. [121, 122].

The results presented in this chapter were obtained from the same NEMD simulations presented in Chapter 3. All atomic velocities were written to disk every 40 ns (20 000 steps) in the same data collection period during which the temperature profiles were collected. Based on the atomic velocities, I then used the combination $w(z) = \sqrt{m(z)/2}\, v(z)$ as the signal to be transformed, so that the wavelet energy density calculated by Eq. 5.3 corresponds to the density of kinetic energy per length, per wavenumber. To reduce noise, each of the energy distributions reported below is the average of distributions calculated from ten independent simulations under the same conditions.

In the 1D systems, the equilibrium site of each atom has a unique value of z, so the atomic velocities can be translated directly into $w(z)$. In the 3D systems, I average together the velocities of atoms in the same (002) plane (i.e., those whose equilibrium positions have the same z coordinate) to form the signal $w(z)$. This is equivalent to sampling only the normal modes with $\mathbf{q}$ parallel to the $\langle 001 \rangle$ direction. The different polarizations ν can be sampled by selecting the corresponding component of atomic velocities in calculating $w(z)$.

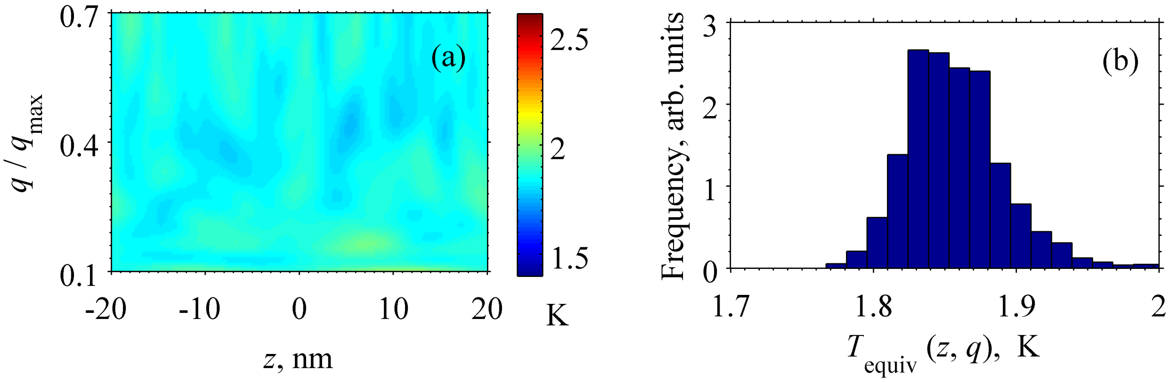

Figure 5.1: (a) The energy distribution in terms of equivalent temperature, T_{equiv}, calculated using the wavelet transform in a system at thermal equilibrium. (b) A histogram of T_{equiv}.

For example, to probe the energy density of a longitudinal mode along $\langle 001 \rangle$, I use the z-component of the atomic velocities to construct $w(z)$. In the practical implementation of the transform, I choose the wavenumber of the mother wavelet as $q_0 = (5a)^{-1}$ and minimum and maximum wavenumbers corresponding to constants $\eta = 0.05$ and $\phi = 1$ as described by Baker *et al.* [121]. These settings produce energy spectra with useful information in the range of wavenumbers between $q/q_{\text{max}} = 0.04$ and 0.7.

To facilitate interpretation, in all of the following results, I use the equipartition principle to convert the energy density at each point, $E^{\text{K}}(z, q)$, to an "equivalent" temperature $T_{\text{equiv}}(z, q)$ in K. This would be the temperature of a system with an equal energy density distributed uniformly; i.e., at thermal equilibrium.

5.1.2 Verification

In order to verify that the method has been correctly implemented, and to establish a basis for comparison, I calculate the energy density in a system at equilibrium. As a test system, I simulate an interface between 3D Ar/heavy Ar with LJ forces at $T_{\text{nominal}} = 2$ K, but with zero heat current applied. The resulting energy distribution is shown in Fig. 5.1a in terms of $T_{\text{equiv}}(z, q)$.

As expected for a system at thermal equilibrium, the energy appears relatively evenly distributed both in space (horizontal axis) and among normal modes, as enumerated by wavenumbers (vertical axis). The true average temperature is $T = 1.86$ K, slightly lower than the nominal temperature of 2 K because of the simple method for setting atomic velocities (Section 3.1.1). To capture the magnitude of fluctuations in the data, I show a histogram of the calculated values of $T_{\mathrm{equiv}}(z, q)$ in Fig. 5.1b. The fluctuations in the measured energy distribution are equivalent to temperature fluctuations of ~ 0.1 K, which are sufficiently small to resolve the non-equilibrium effects presented in the next section, specifically in Figs. 5.2 and 5.3.

5.2 Results: Energy distributions

In the following sections, I present the distributions of kinetic energy calculated by the wavelet transform in one- and three-dimensional NEMD simulations.

5.2.1 In one dimension

The distributions of energy density in six 1D NEMD simulations are shown in Fig. 5.2. Each row was collected at the same T_{nominal}: (a,b) 2 K, (c,d) 6 K, and (e,f) 12 K, corresponding to the temperature range of conductance data presented in Section 3.2.1. Refer to Fig. 3.6 to see the temperature profiles $T(z)$ corresponding to the simulations at $T_{\mathrm{nominal}} = 6$ K. The left column (a,c,e) shows the distributions arising in systems with LJ forces, and the right column (b,d,f) shows the distributions in harmonic systems.

At low temperature (2 K), the LJ and harmonic systems have a similar energy distribution. There is an excess of energy in the Ar side in modes with wavenumbers higher than $\sim 0.4\, q_{\mathrm{max}}$. This can be understood by referring to the dispersion relation (Eq. 2.16), which shows that given the mass ratio of 3 between the two materials, the highest frequency in heavy Ar corresponds to a wavenumber of

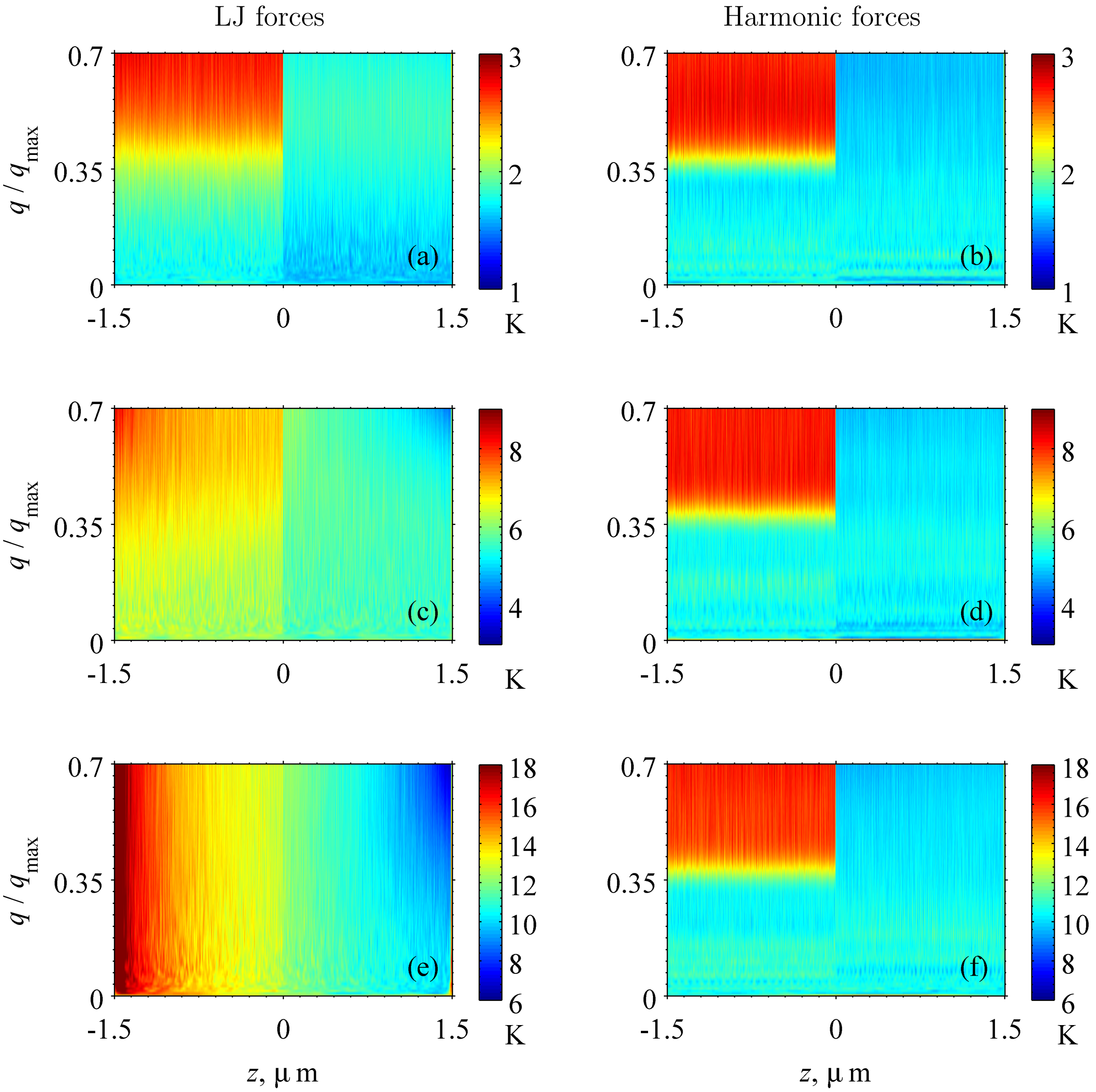

Figure 5.2: Energy distributions, represented in terms of equivalent temperature, calculated using the wavelet transform during 1D NEMD simulations at (a,b) 2 K, (c,d) 6 K, and (e,f) 12 K.

$$\frac{q}{q_{\max}} = \frac{2}{\pi} \arcsin(3^{-1/2}) \approx 0.39$$

in the Ar. As the temperature increases, (c,e) anharmonic phonon scattering in the LJ system allows the energy to redistribute along the q axis, while (d,f) the lack of phonon scattering in the harmonic system prevents the excess energy from thermalizing. Note that in panels (c,e), the energy distribution has not quite completely thermalized among the normal modes in the heavy Ar. This indicates that the mean free paths in the heavy Ar are longer than in the Ar, which is consistent with the lower temperature and the normal mode decomposition calculations presented in Section 5.4.1.

5.2.2 In three dimensions

I have also calculated the energy density in 3D simulations. Although in principle it is possible to calculate the energy density for each mode in the full Brillouin zone, for simplicity and ease of comparison with the 1D simulations, I only present here the energy density in longtitudinal and transverse modes along the $\langle 001 \rangle$ direction. The resolution in both z and q is low, since each signal represents the velocities of only 72 planes, versus 11232 atoms in the 1D systems.[2] However, one can still see that, as in the 1D systems, the LJ and harmonic systems have similar distributions of energy at low temperature, with an excess of energy in Ar above $0.4\,q_{\max}$. As the temperature increases, the energy thermalizes in the LJ system but remains confined to the high-wavenumber modes in the harmonic system.

5.3 Normal mode decomposition

To interpret the energy distributions presented in Section 5.2, it is useful to know the mean free paths of modes in the bulk materials. In this section, I use normal mode decomposition (NMD) to calculate those mean free paths over the ranges of temperatures encountered in

---

[2] The atoms in the immobile walls are excluded from the signals.

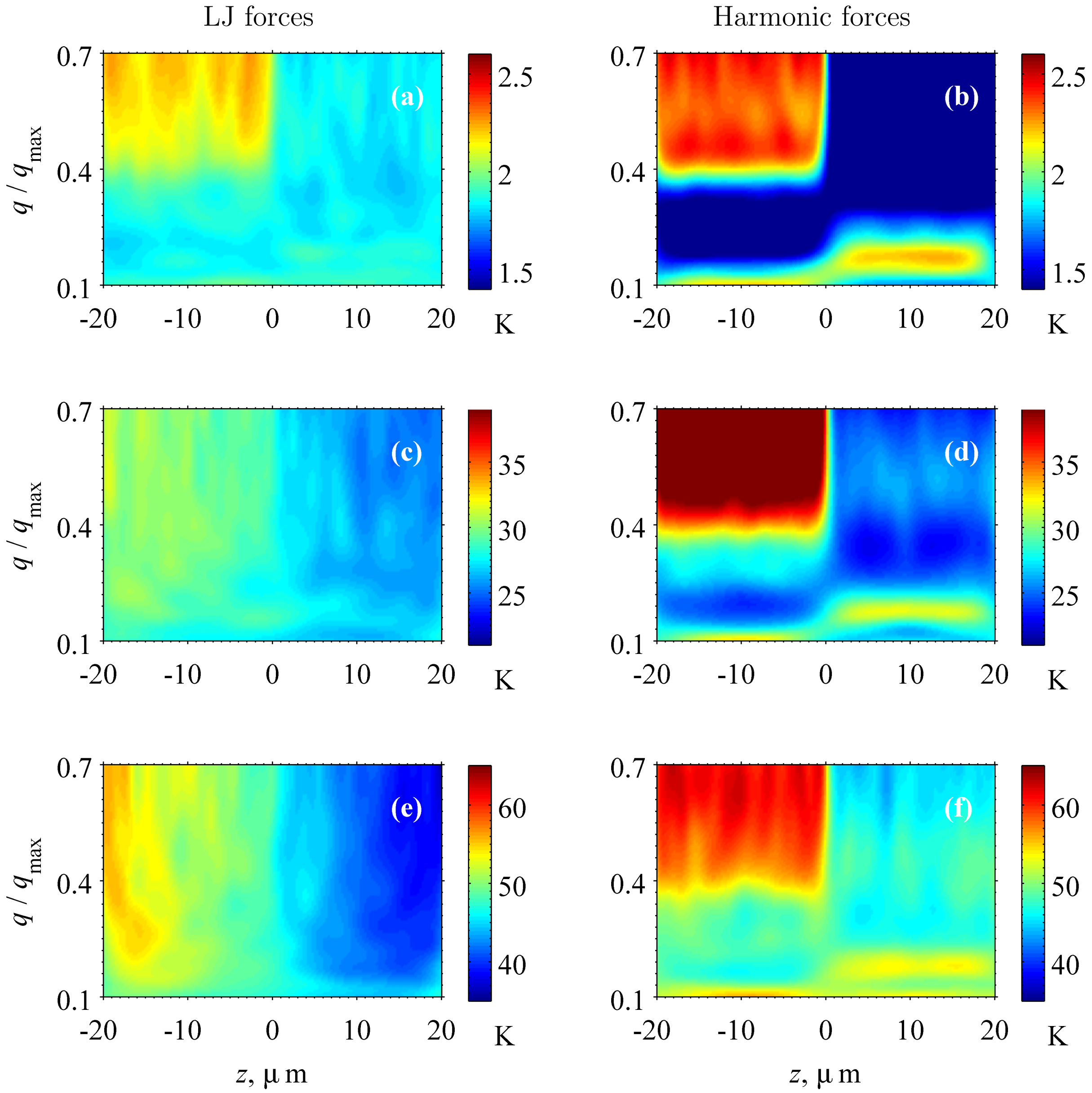

Figure 5.3: Energy distributions, represented in terms of equivalent temperature, calculated using the wavelet transform during 1D NEMD simulations at (a,b) 10 K, (c,d) 30 K, and (e,f) 50 K.

the NEMD simulations. For a thorough discussion of the method, refer to the recent review by McGaughey and Larkin [123]. In the following overview, I survey the concepts necessary to interpret the results presented in Section 5.4.

5.3.1 Methodology

Broadly speaking, the NMD method consists of the following steps:

1. Specify the atomic structure of the material of interest and perform lattice dynamics calculations (Section 2.2.1) to obtain $\omega_{\mathbf{q},\nu}$ and $\mathbf{e}_{\mathbf{q},\nu}$ of each mode in the harmonic system (i.e., the low temperature limit).

2. Perform an MD simulation of the same structure at thermal equilibrium, recording snapshots of $r_{i,\alpha}$ and $\dot{r}_{i,\alpha}$ at a sufficiently high rate to capture the highest-frequency modes and for a sufficiently long duration to reduce statistical noise.

3. Use those data, along with the normal mode properties from Step 1, to calculate $\xi_{\mathbf{q},\nu}(t)$ and $\dot{\xi}_{\mathbf{q},\nu}(t)$.

4. Calculate the autocorrelation of $\xi_{\mathbf{q},\nu}(t)$ and $\dot{\xi}_{\mathbf{q},\nu}(t)$ in time. In cases where the single-mode relaxation time approximation (SMRTA) is accurate (Eq. 2.28), the autocorrelation function will closely resemble an exponentially damped oscillation in the time domain or, equivalently, a Lorentzian peak in the frequency domain (see Appendix A.1 of Ref. [124]). In this work, I use the frequency domain, and the width of the peak is inversely proportional to the total relaxation time $\tau_{\mathbf{q},\nu}$.

The analysis using the normal mode displacements, ξ, is problematic at high temperatures, where their contribution to the system energy is increasingly anharmonic and the equipartition theorem breaks down [123]. Therefore, in this work I only use the normal mode velocities, $\dot{\xi}$, whose contribution to the Hamiltonian is always harmonic. To clarify Step 4: after calculating

$\dot{\xi}_{\mathbf{q},\nu}(t)$ of each mode using Eq. 2.9, I use it to calculate the kinetic energy spectrum in that mode:

$$E^{\mathrm{K}}_{\mathbf{q},\nu}(\omega) = \frac{1}{2\pi t_{\mathrm{f}}} \left| \bar{\dot{\xi}}_{\mathbf{q},\nu}(\omega) \right|^2, \tag{5.5}$$

where t_{f} is the duration of the sampled signal $\dot{\xi}_{\mathbf{q},\nu}(t)$, and the bar denotes the Fourier transform $\bar{\dot{\xi}}_{\mathbf{q},\nu}(\omega) = \int_0^{t_{\mathrm{f}}} \dot{\xi}_{\mathbf{q},\nu}(t) \exp(-i\omega t)\, dt$. Equation 5.5 is normalized so that, given a duration t_{f} much longer than the timescale of oscillations, the average kinetic energy in the mode is

$$\langle E^{\mathrm{K}}_{\mathbf{q},\nu} \rangle = \int_0^{\infty} E^{\mathrm{K}}_{\mathbf{q},\nu}(\omega)\, d\omega. \tag{5.6}$$

If the SMRTA is valid, then the “measured” energy spectrum calculated according to Eq. 5.5 will resemble a Lorentzian function given by

$$E^{\mathrm{K}}_{\mathbf{q},\nu}(\omega) = \frac{1}{2} k_{\mathrm{B}} T \, \frac{\Gamma_{\mathbf{q},\nu}/\pi}{\left(\omega - \omega_{\mathbf{q},\nu}\right)^2 + \Gamma^2_{\mathbf{q},\nu}}, \tag{5.7}$$

where I have used the fact that, in a system at thermal equilibrium, $\langle E^{\mathrm{K}}_{\mathbf{q},\nu} \rangle = \frac{1}{2} k_{\mathrm{B}} T$. The frequency of the normal mode is $\omega_{\mathbf{q},\nu}$, and the total relaxation time is $\tau_{\mathbf{q},\nu} = \left(2\Gamma_{\mathbf{q},\nu}\right)^{-1}$.

I have used Eqs. 5.5 and 5.7 to determine the normal mode frequencies and relaxation times in the simulated Ar and heavy Ar systems whose parameters are given in Section 2.5. Each system is specified by its dimensionality, material, and temperature: e.g., 3D Ar at 20 K. In all calculations, each simulation domain has periodic boundary conditions, and the data are collected at thermal equilibrium. The 1D systems consist of 5000 atoms (~ 1.33 µm), and the 3D systems consist of 4000 atoms ($\sim (5.31\ \mathrm{nm})^3$). Although the size of the 3D system appears small compared to the mean free paths presented in Section 5.4.2, the periodic boundary conditions ensure that no boundary scattering occurs, so it is possible to simulate systems using domains smaller than the mean free path. The results presented in Ref. [123] show that the system size of $(10a)^3$ is sufficiently large to reproduce bulk transport behavior. I chose to analyze 400 modes in the 1D system and 435 modes in the 3D system, all sampled uniformly throughout the first Brillouin zone. In 3D, the modes correspond to the 145 q-points in the irreducible Brillouin zone with spacing $\Delta q_\alpha = 2\pi/L_\alpha = \pi/(5a)$.

For each system, I performed ten simulations under identical conditions except with a different initial configuration of randomized velocities. Each simulation ran for 2^{20} timesteps (~ 2 ns) to equilibrate before data collection, at which point the atomic velocities were sampled once every 32 timesteps, corresponding to a maximum observable frequency of 15.6 THz, for a duration of another 2^{20} timesteps. These are similar to the settings used in Ref. [123]. Finally, for each mode in the system, I obtained $E^{\mathrm{K}}_{\mathbf{q},\nu}(\omega)$ in the ten simulations using Eq. 5.5 and averaged them together to fit to the form of Eq. 5.7.

I found that the following fitting procedure provided good results. The frequencies and linewidths were obtained by fitting $\log\left[E^{\mathrm{K}}_{\mathbf{q},\nu}(\omega)\right]$, which provides better sensitivity than fitting $E^{\mathrm{K}}_{\mathbf{q},\nu}(\omega)$ itself. Then, Eq. 5.7 was fit to the data points within 2 orders of magnitude of the maximum value in a given spectrum. Finally, the points within ±20% of the fitted value of $\omega_{\mathbf{q},\nu}$ were used to re-fit the equation, yielding final values of $\omega_{\mathbf{q},\nu}$ and $\Gamma_{\mathbf{q},\nu}$.

5.3.2 Verification

In order to verify my implementation of the method, I reproduced the calculation in Ref. [123] for the relaxation times in LJ argon at a temperature of 10 K. To facilitate comparison, for this calculation I used a matching cutoff distance of $r_{\mathrm{cut}} = 2.5\sigma = 8.378$ Å in the LJ potential, rather than the value of $r_{\mathrm{cut}} = 4.5$ Å used elsewhere in this work to include only nearest neighbors. All other settings mentioned in the previous section are the same as those of Ref. [123]. Two examples of calculated $|\bar{\dot{\xi}}_{\mathbf{q},\nu}(\omega)|/(2\pi t_{\mathrm{f}})$ (colored dots) and the corresponding fitted Lorentzians (colored lines) are shown in Fig. 5.4a. The spectra are fit well by Eq. 5.7 over four orders of magnitude, indicating that the SMRTA is valid for this system. For each mode, the frequency calculated from harmonic lattice dynamics is also plotted (gray lines). As expected, the actual normal mode frequencies are close to the harmonic values, but slightly lower due to anharmonic softening at elevated temperature. Similar fits were obtained for

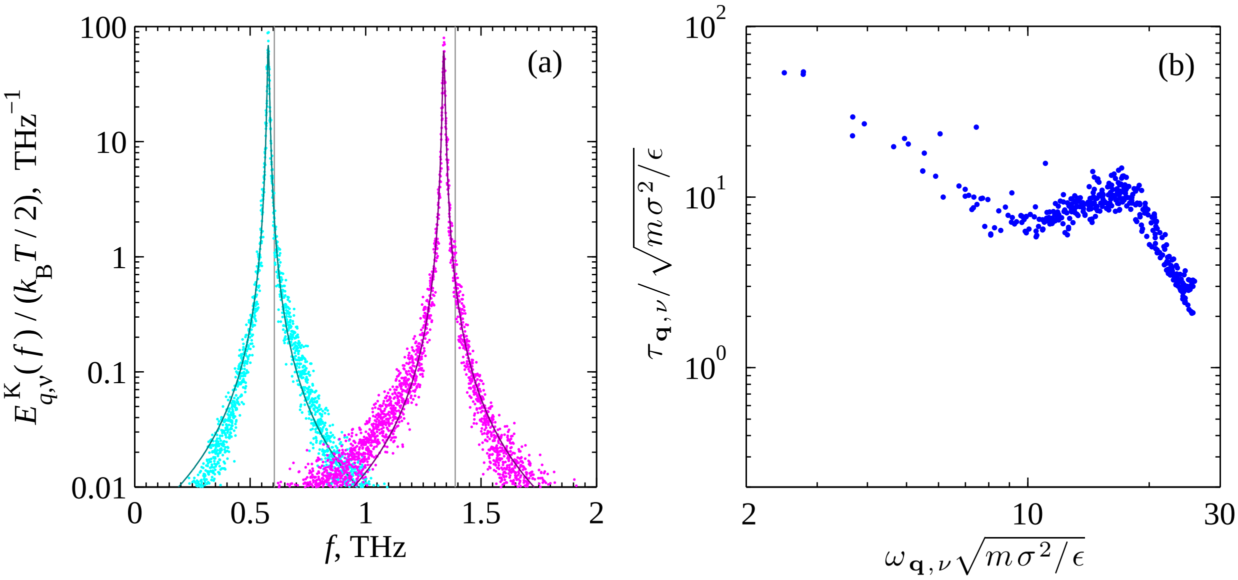

Figure 5.4: NMD results for the same system simulated in Ref. [123]. Compare with their Fig. 3. (a) Calculated and fitted spectra of kinetic energy (dots and lines) in two modes with their harmonic frequencies (vertical lines). (b) The relaxation times of all sampled modes.

all of the sampled modes, and the resulting frequencies and relaxation times are shown in Fig. 5.4b. They are normalized by the LJ time scale, $\sqrt{m\sigma^2/\epsilon}$, for direct comparison with Fig. 3 of Ref. [123]. The data are very closely reproduced.

As a final point, I performed the same calculations in the 3D LJ Ar material with only nearest-neighbor interactions at $T = (5, 15, 25, 35, 45)$ K to obtain the dispersion relations $\omega_{\mathbf{q},\nu}(\mathbf{q})$ as a function of temperature. Those results are plotted in Fig. 2.2 and discussed in Section 2.5. The normal mode frequencies agree remarkably well with experimental measurements of the dispersion in real Ar at 4 K, and they exhibit the expected softening with temperature.

5.4 Results: Relaxation times

With the NMD method established, I use it here to obtain the relaxation times of normal modes in Ar and heavy Ar over the same temperature ranges used in the NEMD simulations of Chapter 3. I present the results separately for the one- and three-dimensional systems.

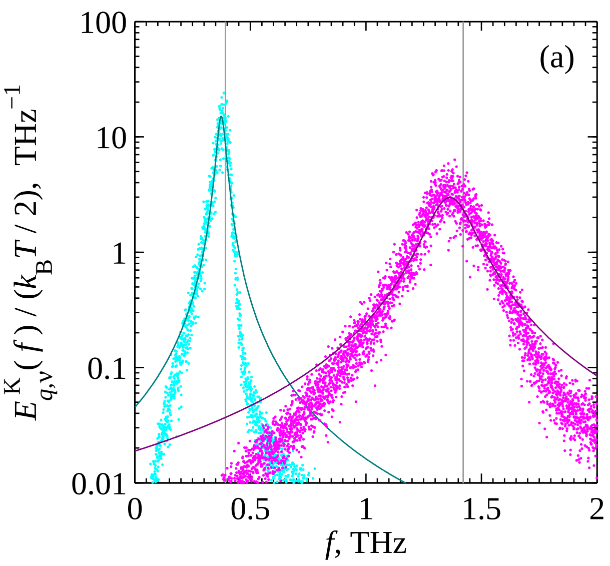

Figure 5.5: Energy spectra in two arbitrary normal modes sampled from (a) one-dimensional LJ Ar at 8 K and (b) three-dimensional LJ Ar at 35 K.

5.4.1 In one dimension

I have fitted the frequencies and relaxation times of 1D Ar and heavy Ar at temperatures ranging from 2 K to 12 K. Two such fits to data at 8 K are shown in Fig. 5.5a. The collected spectra are only well fit by Lorentzian functions over roughly one order of magnitude, which shows that the SMRTA is less valid in 1D systems than in 3D systems. This is not entirely surprising, since researchers have long recognized that thermal transport in one-dimensional chains is poorly behaved and has a deep research field of its own—for example, see Refs. [107, 125–131]—that is well beyond the scope of this work. The main issue relevant here is that phonon–phonon processes are limited in 1D chains due to their low dimensionality, leading to phenomena such as divergent thermal conductivity with system length [107, 131]. For the present purposes, the limitation on possible phonon–phonon scattering processes is a likely explanation for the imperfect fitting of the kinetic energy spectra to Lorentzian peaks.

Nevertheless, in the absence of a better model for the normal mode energy spectra, fitting to Eq. 5.7 provides a reasonable estimate of the timescale of energy relaxation. This is similar in spirit to the estimates in Ref. [123] using the virtual crystal approximation to extract the relaxation times in random alloys. The resulting relaxation times are shown in Figure 5.6. They encompass 3–500 ps in Ar at 2 K and 4–1000 ps in heavy Ar at 2 K. In each system, the relaxation time falls roughly as ω^{-1} at low frequencies and more steeply at high frequencies. Increasing temperature also shortens the relaxation time, roughly as T^{-1}. As the temperature increases past ~ 8 K, the relaxation times in both systems begin to grow shorter than the periods of oscillation of the normal modes, as indicated on the plots by gray lines.

The relaxation time of each mode can then be readily transformed into a mean free path using knowledge of the group velocity: $\Lambda_{\mathbf{q},\nu} = |\mathbf{v}_{\mathbf{q},\nu}|\tau_{\mathbf{q},\nu}$. In the one-dimensional chain, the group velocity can be calculated analytically based on the sinusoidal dispersion relation, Eq. 2.16. The resulting mean free paths are shown in Figure 5.7. Over the range of simulated temperatures, the mean free path of most normal modes decreases by an order of magnitude or more. The mean free paths of the lowest-frequency modes are in the range of hundreds of nm at $T = 2$ K and decrease to tens of nm at $T = 12$ K.

5.4.2 In three dimensions

Likewise, I have fitted the frequencies and relaxation times of 3D Ar and heavy Ar at temperatures ranging from 5 K to 45 K. Two such fits to normal mode spectra at 35 K are shown in Fig. 5.5b. These spectra are better modeled by Eq. 5.7 than the spectra in the 1D system.

The relaxation times of all of the sampled modes are shown in Figure 5.8. They encompass 10–200 ps in Ar at 5 K and 20–400 ps in heavy Ar at 5 K. The relaxation time falls roughly as ω^{-2} at low frequencies, as expected [132, 133], but exhibits a more complicated dependence at higher frequencies. I then convert these relaxation times into mean free paths, plotted in Fig. 5.9. Unfortunately, the group velocities $\mathbf{v}_{\mathbf{q},\nu} = \nabla\omega_\nu(\mathbf{q})$ throughout the 3D Brillouin zone are more difficult to calculate analytically than in 1D (see Section 3.4 of Ref. [123]), and the q-point density in the $V = (10a)^3$ system is too coarse to numerically approximate the gradient by finite difference. Therefore, I only obtain the mean free paths of modes along

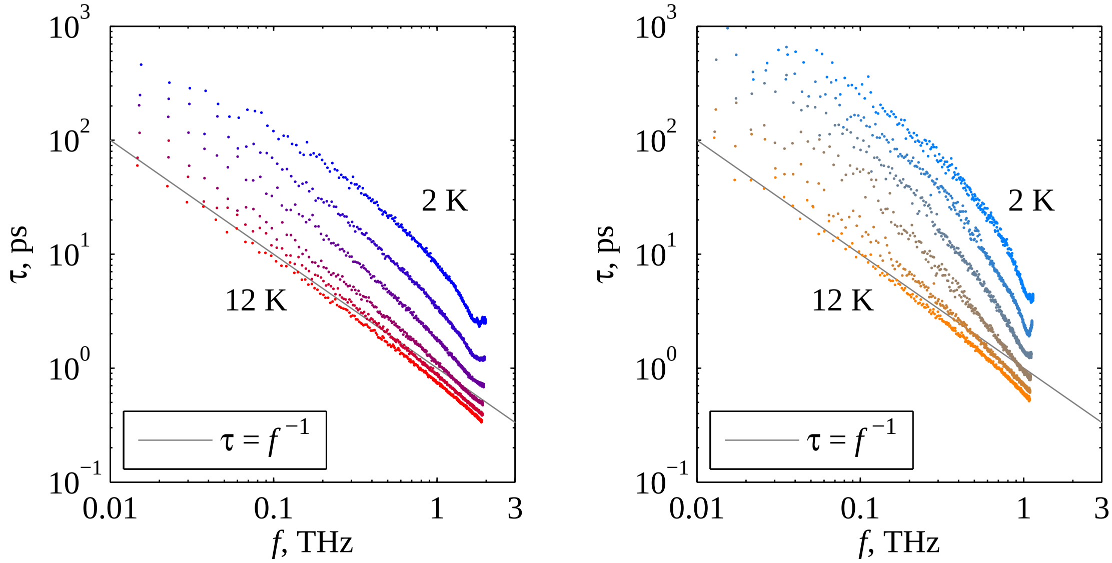

Figure 5.6: Relaxation times for normal modes in one-dimensional Ar (blue to red) and heavy Ar (cyan to orange) at temperatures $T = [2, 4, 6, 10, 12]$ K.

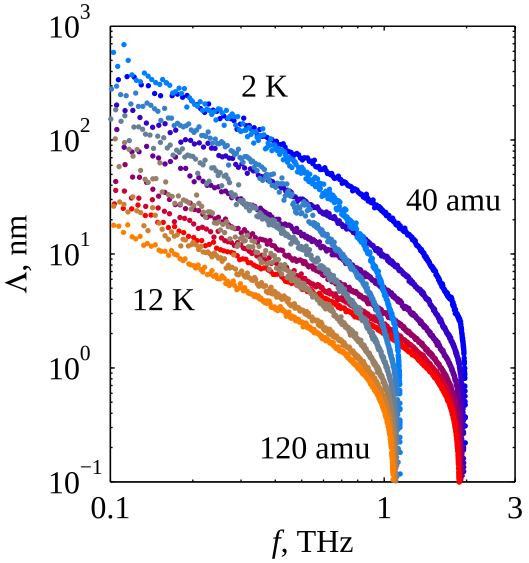

Figure 5.7: Mean free paths for normal modes in one-dimensional Ar (blue to red) and heavy Ar (cyan to orange) at temperatures $T = [2, 4, 6, 10, 12]$ K.

the ⟨100⟩ and ⟨111⟩ directions for which Eq. 2.16 is valid, given the correct interplanar force constants [93]. The mean free paths decrease by an order of magnitude over the range of simulated temperatures, similar to the decrease observed in 1D systems. The mean free paths of the lowest-frequency modes are in the range of 100 nm at $T = 5$ K, and they decrease to tens of nm at $T = 45$ K.

5.5 Discussion

The results presented in this chapter enable further discussion on two issues: (1) the transition from ballistic to diffusive transport with increasing temperature and (2) the role of the phonon distribution in conductance at high temperature.

5.5.1 Ballistic and diffusive transport

First, the energy distributions presented in Section 5.2 show that, in both the 1D and 3D systems, the transport is ballistic in simulations at the lowest T_{nominal} and diffusive at the highest. Some ballistic-to-diffusive transition must occur in the intervening temperatures, and the mean free paths presented in Section 5.4 provide information to elucidate that transition. The temperature trends in the energy distributions are *qualitatively* consistent with those in the mean free paths—as temperature increases in the LJ system, the mean free path decreases and the energy distribution tends to equilibrate among the normal modes.

However, I am not fully confident in the *quantitative* comparison between the two calculations. The calculations appear to be consistent in the 3D system, but not in the 1D system. For example, in the 3D system at $T_{\text{nominal}} = 10$ K, the energy in modes above $q/q_{\text{max}} \sim 0.4$ appears to have relaxed partially, but not completely, indicating that the mean free paths are on the same order of magnitude as the lead length of 20 nm. Indeed, the corresponding mean free paths in Fig. 5.9 are about 10 nm. On the other hand, the 1D system at $T_{\text{nominal}} = 6$ K also exhibits a partially-ballistic, partially-diffuse energy distribution.

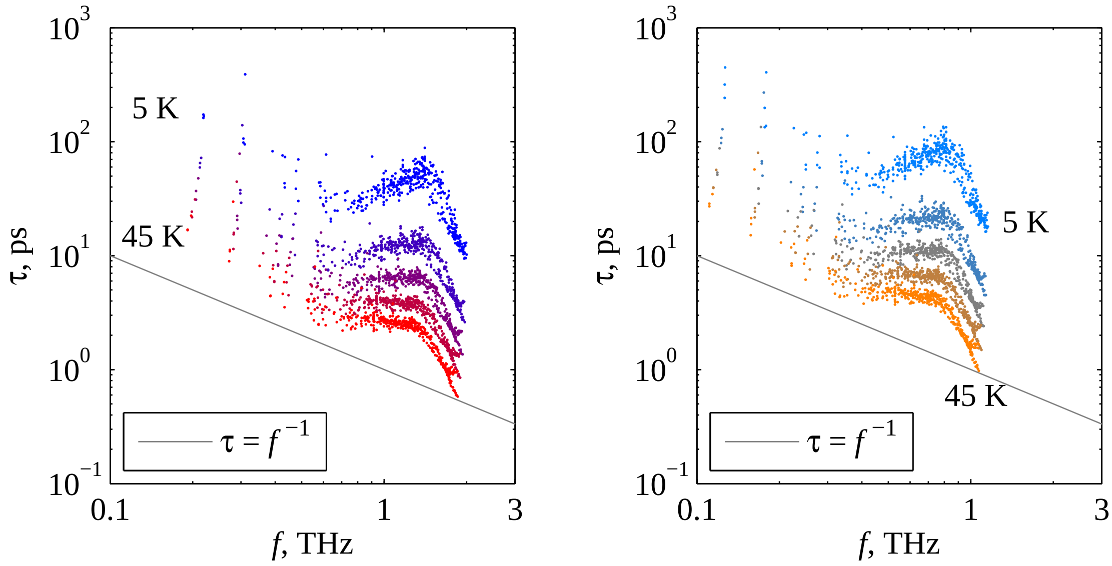

Figure 5.8: Relaxation times for normal modes in three-dimensional Ar (blue to red) and heavy Ar (cyan to orange) at temperatures $T = [5, 15, 25, 35, 45]$ K.

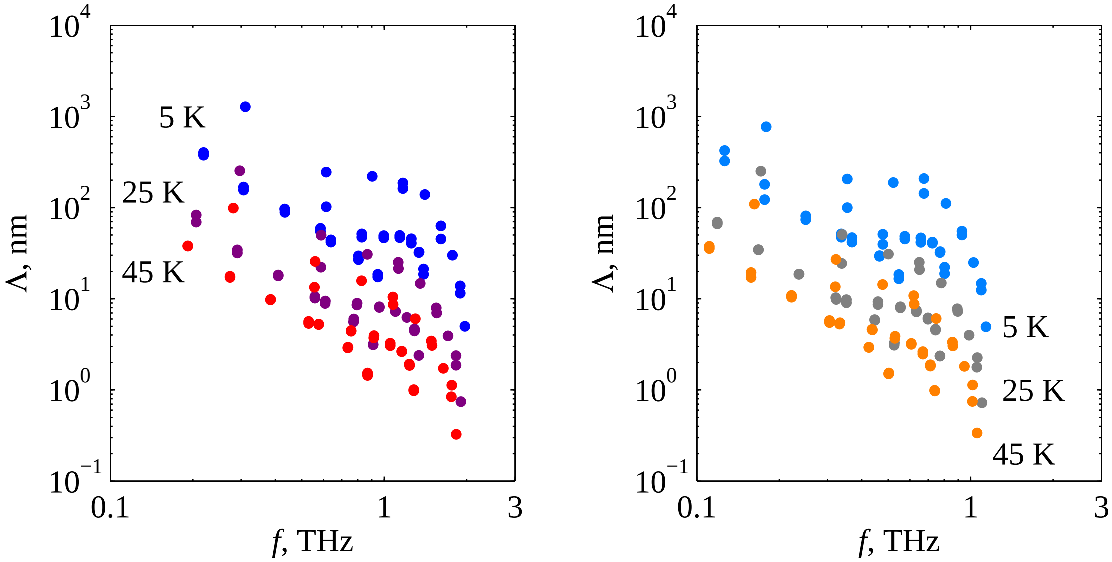

Figure 5.9: Mean free paths for normal modes along the ⟨100⟩ and ⟨111⟩ directions in three-dimensional Ar (blue to red) and heavy Ar (cyan to orange) at temperatures $T = [2, 25, 45]$ K.

However, the corresponding mean free paths in Fig. 5.7 are only a few nm, much shorter than the lead length of 1.5 µm. In principle, it may be possible in the future to make this comparison more rigorously by using the relaxation times as input to iterative solutions of the Boltzmann transport equation (Eq. 2.32) to obtain $n_{\mathbf{q},\nu}$, and hence $E_{\mathbf{q},\nu}$. This approach is not new [102], but as mentioned in Section 2.4.2, applying it to interfaces requires the transmissivity $\alpha_{\mathbf{q},\nu}$ as input, for which there is still little consensus on effective models. Therefore, at present, it is unclear whether solutions to the BTE can provide physically meaningful results in interface-dominated transport.

When compared with the results of Chapter 3, it also appears that the shift from ballistic to diffusive transport may be associated with a change in the trend of $h(T)$. The energy distributions show that the transition occurs around roughly 6 to 8 K in the 1D systems (Fig. 5.2.1) and around 20 K in the 3D systems (Fig. 5.2.2). The trends in $h(T)$ also appear to change behavior near those temperatures. This aligns with the findings of Liang and Keblinski [134, 135], who investigated the effect of ballistic transport on interfacial conductance by inducing diffusive scattering at the far walls.

5.5.2 The phonon distribution and thermal conductance

Although the ballistic effects on interfacial conductance are interesting in certain applications, such as in superlattices [43], they are also often treated as an artifact in determining the "true" conductance under a thermal distribution of phonons. It is therefore preferable to conduct simulations in the diffusive regime, in which scattering mechanisms are strong enough to thermalize the phonon distribution. In that context, the results of this chapter help identify the subset of simulations in which transport is diffusive: evidently, the 1D simulations at $T_{\text{nominal}} \gtrsim 8$ K and the 3D simulations at $T_{\text{nominal}} \gtrsim 20$ K. In those regimes, the values of $h(T)$ calculated in Chapter 3 increase with temperature roughly linearly, which corroborates previous findings in MD [75, 82].

In this section, I seek a qualitative explanation for this behavior in $h(T)$ that is related to $n_{\mathbf{q},\nu}$, since the results of Chapter 4 suggest that the other suspected culprit, $\alpha_{\mathbf{q},\nu}$, is unlikely to be responsible. However, within the noise of the collected data, I observe the apparently uninteresting behavior that $n_{\mathbf{q},\nu} \rightarrow n_{\mathrm{B-E}}(\omega_{\mathbf{q},\nu}, T)$ as T increases in the diffusive regime: see Figs. 5.2e and 5.3e. Therefore, in agreement with Landry and McGaughey [75], I find no support in my simulations for Simons' correction [26] to the distribution to account for disruption by a non-zero heat current. My results do, however, support the idea that the distribution is strongly disrupted by the *interface*, albeit at low temperatures, not high temperatures.

The physical picture most consistent with these results can be seen as a conglomeration of models described by Duda *et al.* [81], Wu and Luo [83], and Murakami *et al.* [84] to explain the results of molecular dynamics simulations. In this picture, the transmissivity remains relatively unchanged as temperature increases. However, the temperature increases the rate of inelastic phonon processes in the *bulk materials*, which are responsible for the anomalous conductance.

The results presented in Chapters 3, 4 , and 5 in the 1D and 3D Ar/heavy Ar system are consistent with this picture. The transmissivity does not change much with increasing vibrational amplitude and therefore "equivalent temperature" (Section 4.2). Notably, the maximum frequency of transmission stays fixed at 1.15 THz, which is the highest frequency of any modes in the heavy Ar. Therefore, the phonons reflected back into the Ar lead have a highly non-equilibrium distribution, with excess energy in modes above $q/q_{\mathrm{max}} = 0.4$ (Section 5.2). That reflected energy must transfer into modes of lower wavenumber/frequency before it can later transmit through the interface. At low temperatures, such processes happen very slowly, and the reflected energy can only contribute at a slow rate to the flux through the interface. As temperature increases through the ranges simulated in this work, the relaxation times decrease by an order of magnitude or more (Section 5.4), which allows the non-equilibrium distribution of phonons to rethermalize more rapidly. This enables the excess high-frequency phonons to transfer energy at a faster rate to lower modes and transmit through the interface, leading to a higher thermal conductance (Section 3.2).

Chapter 6

Conclusions

> "And then came the grandest idea of all! We actually made a map of the country, on the scale of *a mile to the mile!*"
>
> "Have you used it much?" I enquired.
>
> "It has never been spread out, yet," said Mein Herr.
>
> — Lewis Carroll, *Sylvie and Bruno Concluded*, 1893 [136]

In this chapter, I summarize the findings of this work in a concise map that might be more easily spread out, in hopes that it can be judged alongside other work on this topic. I provide this summary in Section 6.1, and based on those conclusions, I suggest new directions for exploration in Section 6.2.

6.1 Summary of contributions

In this work, I have investigated the thermal conductance at interfaces between non-metallic, crystalline solids. At very low temperatures (tens of K or less), the acoustic mismatch model (AMM) and its derivatives accurately predict the interfacial conductance between solids. However, as written by Prof. Gang Chen in his text, "despite intense research, there is no generally accepted way to calculate the thermal boundary resistance at higher temperatures" [100]. In many cases, the diffuse mismatch model (DMM) provides somewhat better agreement than the AMM, but it has still been shown to both underpredict *and* overpredict experimental data by an order of magnitude or more. In Chapters 1 and 2, I identified several reasons that experimental measurements are believed to differ from the DMM, and I put them roughly into two categories: those that tend to decrease conductance below the DMM, and those that tend to enhance it. The mechanisms for reduced conductance are relatively well understood, at least qualitatively, and I do not address them in this work. However, the mechanisms for increased conductance are very poorly understood. Several different physical mechanisms have been proposed to explain the same experimental measurements of conductance far in excess of the DMM and AMM (Sections 1.3.4 and 2.4). The leading hypothesis appears to be that the excess conductance arises from the onset of inelastic phonon transmission across the interface [39, 67, 68, 82]. Several models have been proposed to account for this effect in various ways [76–78, 80], but little has been done to evaluate their relative validity.

Therefore, the main goal of this work was to compare various hypotheses to explain the anomalously high thermal conductance at ideal interfaces at high temperature. The central scientific contribution of this work is to assemble a diverse set of evidence, all collected in the same material systems, based on which I identify the most likely explanation: that the excess thermal conductance is caused by an increased rate of thermalization of phonons near the interface. This main conclusion is based on several basic findings that I have presented in Chapters 3 to 5, which represent contributions in their own right. I summarize them here in a framework leading to the main conclusion. First, here are the findings that address the connection between the trend in $h(T)$ and inelastic phonon processes:

- Anharmonicity of interatomic forces correlates with an increasing trend in $h(T)$ (Section 3.2). In a system with only harmonic forces, $h(T)$ is constant.
- Anharmonicity of interatomic forces also correlates with inelastic phonon processes at an interface (Section 4.2) and in bulk materials (Section 5.4).

Therefore, I infer that the increasing trend in $h(T)$ can indeed be explained by inelastic phonon processes of some kind. I then determine the importance of inelastic processes at the interface alone:

- In systems with anharmonic forces at the interface only, and harmonic forces everywhere else, $h(T)$ is constant in 1D systems (Section 3.2.1) and increases only weakly in 3D systems (Section 3.2.2).
- In the same systems, the transmissivity of individual modes actually *decreases* slightly, despite the anharmonic forces enabling inelastic scattering (Section 4.2).

From these observations, I infer that inelastic processes *at the interface* are not the dominant mechanism for the increasing trend in $h(T)$ at high temperature. This does not support the prevailing explanation. Finally, I consider the importance of inelastic processes elsewhere:

- At low temperatures, the interface acts as a low-pass phonon filter that causes a strong non-equilibrium phonon population in the material with the higher maximum frequency (Section 5.2).
- As temperature increases in an anharmonic system, the phonon relaxation times decrease (Section 5.4) and the phonon distribution approaches an equilibrium distribution (Section 5.2).

The increasing trend in $h(T)$ is therefore correlated with the phonon distribution approaching equilibrium: $n_{\mathbf{q},\nu} \rightarrow n_{\text{B–E}}(\omega_{\mathbf{q},\nu}, T)$. Therefore, I see no evidence that a deviation of $n_{\mathbf{q},\nu}$ from equilibrium, as in the correction proposed by Simons [26], causes increases in $h(T)$ at high temperature. On the contrary: I infer that the excess conductance is actually enabled by the phonon–phonon scattering processes in the bulk material, as described in Section 5.5.2.

Although this conclusion aligns with some previous work [81, 83, 84], it differs from several experimental [38, 39, 67, 68] and theoretical works [29, 76, 78, 80, 85, 137] that explain the excess conductance in terms of inelastic transmission. In particular, the recent work by

Hohensee *et al.* [68] not only supports the explanation based on inelastic transmission, but it also provides some experimental evidence that phonon rethermalization is not the dominant mechanism as proposed here. They observed that the thermal conductance at several metal/diamond interfaces is insensitive to the presence or absence of nitrogen impurities in the diamond, within their experimental uncertainty. If near-interface rethermalization were the dominant cause for the excess in $h(T)$, the rethermalization rates would presumably be different in nitrogen-rich and nitrogen-free diamond, but no such difference was evident in the conductance measurements. In addition, diamond is a very stiff material with relatively small anharmonicity, and it remains to be shown whether the phonon–phonon scattering rates are high enough to explain the high conductance. These are important questions to be addressed in further evaluating the present hypothesis.

Whichever hypothesis proves correct—whether the excess $h(T)$ is driven by inelastic transmission or inelastic rethermalization—future work should further investigate inelastic processes at *non-sharp* interfaces, unlike those used in this work. In other words, the understanding of individual scattering mechanisms (interdiffusion, roughness, etc. in addition to the phonon–phonon scattering examined in this work) is reaching the point where it will be possible to understand their *simultaneous* effect on interfacial transport, which is necessary at real interfaces. Other computational work has generally shown that a "small" departure from a sharp interface can actually enhance conductance, whether by a layer of intermediate vibrational impedance [112], interdiffusion [112, 138], or roughness [65, 66]. In most cases, increasing the degree of the "defect" eventually results in a reduced conductance, so that there is some small, optimum level for enhancing conductance. Most experiments to date appear to be in the latter regime, observing only reduced interfacial thermal conductance due to interdiffusion [51], dislocations [55], and roughening [56, 139]. However, recent experiments by Gorham *et al.* [58] show that ion irradiation can indeed increase the thermal conductance at Al/Si interfaces, both with and without the native oxide interlayer, in support of the computational work. Adding the role of inelastic scattering to this picture will be an important but non-trivial task. Some experimental work does suggest that inelastic processes may be important even at interfaces that are less vibrationally mismatched than the metal/diamond interfaces: for example, see the measurements of $h(T)$ at metal/Al_2O_3, Cr/Si, and Pt/AlN interfaces by Hopkins *et al.* [52, 53]. At several of these interfaces, the measured $h(T)$ falls significantly below the DMM, presumably due to conductance-reducing mechanisms discussed in Section 1.3.3. However, the trend in $h(T)$ rises much more sharply than the DMM prediction, in contrast with the reduced and flattened trend in $h(T)$ observed at roughened Al/Si interfaces [56, 57], for example. These different observed trends suggest that inelastic processes have different levels of relative importance in systems with strong scattering from other mechanisms, which presents the challenge of simultaneously modeling several scattering mechanisms that may not be independent. From another perspective, these systems with different levels of contributions from each scattering mechanism present opportunities for further evaluating the details of the inelastic processes—e.g., elucidating the relative importance of interfacial and bulk inelastic scattering—as Hohensee *et al.* [68] have done in their comparisons of metal/diamond conductance with types 1A and 2A diamond.

The findings of this work represent a contribution to the fundamental science outlined in Sections 1.3 and 2.4. They could also have value, I hope, in the research and development of devices such as those described in Section 1.1. Traditionally, the primary consideration in quickly judging the conductance between two materials has been the matching of elastic (i.e., harmonic) properties. Recently, attention has also turned to interfacial bonding as an important parameter [140], especially at weak interfaces. In light of this work, anharmonic properties may also warrant investigation as an important determinant of interfacial conductance, both in terms of intrinsic material properties (e.g., Grüneisen parameters) or potentially by manipulation through doping or strain engineering.

6.2 Future work

There are many possible avenues to clarify and extend the conclusions of this work. Here, I suggest just a few.

- *Formulating a model.* The true test of the conclusions of Section 6.1 is whether a model accounting for bulk inelastic scattering actually provides agreement with the $h(T)$ trends calculated in Chapter 3. In my view, this is an important intermediate milestone on the road to modeling experimental measurements of $h(T)$, since the complexity of real interfaces far exceeds our current understanding of interfacial transport.

- *Deeper investigation of the same systems.* In the chain of inferences presented in the previous section, some are weaker than others, and further investigations could be warranted. For example, I pointed out in Chapter 4 that, although the wave packet simulations see a decrease in $\alpha_{\mathbf{q},\nu}$ with amplitude, perhaps this is an artifact of the "0 K" system. Simulations would be useful that could identify mode-wise transmissivity under "realistic" conditions with fully occupied populations of phonons, for example using the methods of Sääskilahti *et al.* [85]. As another example, solutions to the BTE (Eq. 2.32) would be an extremely valuable way to check the consistency of all of the quantities calculated in this work: h, α, n, and τ.

- *Different materials.* Most of the experimental observations of excess conductance have been made between highly mismatched materials [38, 39, 50, 67, 68], much more so than the Ar and heavy Ar simulated in this work. It could be interesting to simulate materials whose elastic properties are more highly mismatched. Similarly, one might better reproduce some other aspect of the experimental observations, such as the mismatch in anharmonic properties; the interfaces of greatest excess conductance were formed between diamond and a heavy metal such as Pb or Bi.

- *Non-ideal interfaces.* Although the excess conductance at certain interfaces holds fundamental interest, the transport at the vast majority of real interfaces is dominated by defects and other conductance-reducing effects (Section 1.3.3). In my view, any applications of the findings of this work in real systems would also contend with (or leverage!) those effects. Therefore, it would be valuable to understand the role of inelastic processes in systems with non-ideal interfaces as well.

Appendix A

Molecular dynamics code

I wrote a program in the C programming language to produce the MD results in this work. At the time of writing, the code and its documentation are available in a public repository hosted at `https://bitbucket.org/namqle/nqlmd` and will be maintained there indefinitely. If unavailable there, the code is available to interested readers on request. In this appendix, I reproduce the manual accompanying the code.

A note on tricks for improving computational efficiency: Since in this work I am interested only in solid systems with no diffusion, atoms maintain the same neighbors throughout the simulation, and the simulations would not benefit from the use of cell lists. Therefore only the use of neighbor lists is implemented in my code. In addition, I have implemented shared-memory parallelization using OpenMP, which was especially useful to reduce the wall time during debugging of very large simulations. The parallelized code is available in the public repository under the "parallel" code branch; the main version is not parallelized.

A.1 Getting started

`nqlmd` is code for running classical molecular dynamics (MD) simulations. It's written in C. I wrote it to do my dissertation research, which means (1) it's very bare-bones, and (2) it's geared toward simulations of heat transfer in solid, insulating materials. If you're looking for a general-purpose MD program with good documentation, a large user community, lots of potential functions, and so on, better choices might be LAMMPS or NAMD. However, for very simple simulations, or for situations that require diving into source code, the simplicity of `nqlmd` might be attractive.

Last warning: I've only used this on Linux and OS X computers. So, for example, the `makefile` won't work on a Windows machine. It's all just plain C code though, so there should be no trouble compiling "manually." Famous last words.

A.1.1 Getting the code

The code lives in a public Git repository at `https://bitbucket.org/namqle/nqlmd`. If you like Git, you know what to do. Otherwise, you can also find a link there to download a zip file. As of this writing, Bitbucket says that the package is 20.3 MB, which is a dirty lie—it should just be a couple hundred kB. Either way, you should end up with a directory whose contents are listed on the webpage (and, if all goes well, in `README.md`).

For Git users, note that there are three branches: `master`, `dev`, and `parallel`. `master` should be a (relatively) stable version, while `dev` often has new features, some of which you might find useful. `parallel` was an attempt to parallelize the code, which successfully implemented shared-memory parallelization using OpenMP. Distributed-memory parallelization using MPI would be nice, but has not yet been implemented. (Help would be welcome. . .)

A.1.2 Compiling it

Navigate to the `src/` directory, where you should find a handful of code and header files. There's also a `makefile`, and if you're lucky, you might be able to simply type `make`. The code uses the C99 standard, and the makefile assumes `gcc` as your C compiler.

If that's no good, you can probably compile it yourself. For me, the simplest working command is something like

```
gcc -std=c99 main.c common.c read_script.c md.c forces.c routine.c cleanup.c -o ../bin/nqlmd
```

issued in `src/`. (If you care, Section A.3 has more details about these files and the code itself.)

If all goes well, by hook or by crook there will be an executable in `bin/` called `nqlmd`.

A.1.3 Testing it

Go to `examples/example01/`, where you should find an input script (`example01.script`) along with a few different choices of initial configuration files (`example01_0K.init`, `example01_40K.init`, and `example01_80K.init`). If you peek in the input script, you should see a line that specifies which initial configuration file is actually being used; see Section A.2.1.

In `examples/example01/`, try

```
../../bin/nqlmd example01 &
```

which should set a simulation off running in the background. It takes 14 seconds to finish on my desktop from 2010. The simulation should have written a log file called `example01.log`—check this out.

The input script also specifies a routine called `write_cfg`, which writes the complete atomic configuration at regular specified intervals. Therefore, you should also see that the simulation generated one `*.cfg` file every 500 timesteps. These are written in a format compatible with the visualization program Atomeye (`http://li.mit.edu/Archive/Graphics/A/`).

A.2 Running your own MD simulations

Once you've compiled and tested `nqlmd`, you're ready to run your own simulations!

A.2.1 Setting up the simulation

All you need are two files: (1) an input script to tell `nqlmd` what to do and (2) a file containing the intial configuration of the system.

1. **The input script.** The name of the script must be ⟨`something`⟩`.script`.[1] This is a plain text file with one instruction per line, which `nqlmd` reads sequentially. Each instruction consists of a keyword followed by its corresponding arguments. All recognized keywords are listed in Table A.1. Note that lines beginning with the '#' character are ignored as comments.

   ```
   # Comments begin with the '#' symbol
   <keyword 1>   <argument 1a>
   <keyword 2>   <argument 2a> <argument 2b>

   # You can have multiple comments to remind yourself what's happening
   <keyword 3>   <argument 3a>
   ...
   ```

   Two topics warrant a bit more detail:

   (a) *Potentials:* Two special keywords are `pot_style` and `pot_params`, which specify interatomic potential functions. Available interatomic potentials are listed in Table A.2.

   Say a simulation contains two atomic types, Si and Ge. Si atoms could be assigned type 1, and Ge atoms assigned type 2. Then three `pot_styles` will need to be defined, along with corresponding `pot_params`: for types 1–1, 2–2, and 1–2.

   (b) *Routines:* Another special keyword is `routine`, which establishes "something to be done during the simulation". A `routine` might be executed every timestep (e.g., `integrate`), or at specified intervals of steps. Available `routine`s are listed in Table A.3.

---

[1] *Important:* the ⟨something⟩ part of the filename will be used as the "jobname". Output files will be saved using the same jobname, with different file extensions. See Section A.2.3.

2. **The initial configuration file.** The name of this file is specified in the input script by the keyword `init_file`. This file contains the atomic configuration from which the simulation starts, formatted like this:

   ```
   One header line for comments, which is ignored
   <total number of atoms, N>
   <id1> <type1> <mass1> <x1> <y1> <z1> <vx1> <vy1> <vz1>
   <id2> <type2> <mass2> <x2> <y2> <z2> <vx2> <vy2> <vz2>
   ...
   <idN> <typeN> <massN> <xN> <yN> <zN> <vxN> <vyN> <vzN>
   ```

   You'll need to generate this file using some kind of external script; as an example, see the Python script `gen_crystal.py` provided in `scripts/`.

   The fields are self-explanatory, except perhaps `id` and `type`. The `id` in fact is not used by `nqlmd`, but can be helpful for post-processing. The `type` determines interatomic interactions. In a given simulation, the atom types should count up sequentially starting at 1. For how they're used, see the keyword `pot_style` in Table A.1, with more details in Section A.3.1.

For examples of these two files—well, see the examples. In `examples/`.

A.2.2 Running the simulation

Easy: call the executable with one command line argument, which must be the prefix of your input script's filename. In other words, if your input script is named `conductivity.script`, run it with

```
<path>/<to>/nqlmd conductivity
```

That's it.

Table A.1: List of keywords and their arguments for input scripts. Use them roughly in this order.

keyword	arguments	comments
`sim_units`	⟨unit system⟩	Can either be "`aap`" (Å, amu, ps, eV) or "`si`" (m, kg, s, J). NOTE: pressure is *always* in $\mathrm{N\,m^{-(d-1)}}$; d is # of dimensions.
`sim_dim`	⟨# dimensions⟩	Integer number of dimensions to simulate: "`1`", "`2`", or "`3`". Determines the number of arguments expected for `sim_box` and `sim_pbc`, as well as format of the file specified by `init_file`.
`sim_box`	⟨x_{min}⟩	Lower bound along the x axis of the simulation domain, in length units specified by `sim_units`.
	⟨x_{max}⟩	Corresponding upper bound.
	...	And so on. In total, specify 2 × `sim_dim` numbers.
`sim_pbc`	⟨PBC_x⟩	Can either be "`1`" (on) or "`0`" (off).
	...	Specify a value for each dimension.
`group`	⟨group id⟩	Integer ID for this group of atoms. NOTE: group ID "`0`" (zero) is reserved to encompass "all atoms".
	⟨x_{min}⟩ ⟨x_{max}⟩ ...	Define a region in the same manner as with `sim_box`. All atoms found inside this region *at the beginning of the simulation* are considered in this group.
`init_file`	⟨config file⟩	The name of a file containing the initial atomic configuration.
`pot_style`	⟨atom type 1⟩ ⟨atom type 2⟩ ⟨style⟩	Set the potential ⟨style⟩ to govern interactions between ⟨atom type 1⟩ and ⟨atom type 2⟩. See Table A.2.
`pot_params`	⟨parameter 1⟩ ...	Format depends on the `pot_style`. See Table A.2.
`timestep`	⟨timestep⟩	Time between steps, in units specified by `sim_units`.
`set_routine`	⟨routine ID⟩	Integer ID that determines the routine's "place in line" when the routine list is executed: "`0`", "`1`", "`2`", ...
	⟨routine name⟩	See Table A.3 for a list of available routines, along with their expected parameters.
	⟨parameter 1⟩	First parameter for this routine.
	...	
`unset_routine`	⟨routine ID⟩	ID of a routine to "turn off."
`run_until`	⟨step #⟩	Proceed with MD simulation until the given step #. NOTE: step numbers persist over simulations within the same script.

Table A.2: List of available interatomic potential styles and their arguments.

style	arguments	comments	$U_{i,j}(r_{i,j}) =$
`harmonic`	$\langle k^{(2)} \rangle$	2nd-order force constant, in [energy]/[length]^2	$\begin{cases} \frac{1}{2}k^{(2)}(r_{i,j} - r_{\mathrm{eq}})^2, & r_{i,j} \leq r_{\mathrm{cut}} \\ 0, & r_{i,j} > r_{\mathrm{cut}} \end{cases}$
	$\langle r_{\mathrm{eq}} \rangle$	Equilibrium distance	
	$\langle r_{\mathrm{cut}} \rangle$	Interaction cut off distance	
`anharmonic`	$\langle k^{(2)} \rangle$	In [energy]/[length]^2	$\begin{cases} \frac{1}{2}k^{(2)}(r_{i,j} - r_{\mathrm{eq}})^2 & \\ +\frac{1}{6}k^{(3)}(r_{i,j} - r_{\mathrm{eq}})^3 & \\ +\frac{1}{24}k^{(4)}(r_{i,j} - r_{\mathrm{eq}})^4, & r_{i,j} \leq r_{\mathrm{cut}} \\ 0, & r_{i,j} > r_{\mathrm{cut}} \end{cases}$
	$\langle k^{(3)} \rangle$	In [energy]/[length]^3	
	$\langle k^{(4)} \rangle$	In [energy]/[length]^4	
	$\langle r_{\mathrm{eq}} \rangle$	Equilibrium distance	
	$\langle r_{\mathrm{cut}} \rangle$	Interaction cut off distance	
`lj`	$\langle \epsilon \rangle$	Energy scale	$\begin{cases} 4\epsilon \left[\left(\frac{\sigma}{r_{i,j}} \right)^{12} - \left(\frac{\sigma}{r_{i,j}} \right)^{6} \right], & r_{i,j} \leq r_{\mathrm{cut}} \\ 0, & r_{i,j} > r_{\mathrm{cut}} \end{cases}$
	$\langle \sigma \rangle$	Length scale	
	$\langle r_{\mathrm{cut}} \rangle$	Interaction cut off distance	

A.2.3 Simulation output

In the following, I abbreviate "prefix of your input script's filename" as "jobname". So, if your input script is `conductivity.script`, the jobname is `conductivity`. As you run a simulation, the program will always keep a log written as ⟨`jobname`⟩`.log`. This is the minimum possible output to expect.

Several `routines` will cause additional output. A special one, `write_macro`, causes the program to write thermodynamic data to ⟨`jobname`⟩`.log` during simulations. Other `routine`s cause output to new files. For example, the `routine` called `temp_profile` calculates the temperature profile across a specified dimension of the simulation domain, and it records data in ⟨`jobname`⟩`.profile`.

The descriptions of `routines` in Table A.3 specifies any output files to expect.

Table A.3: List of `routines` for use in input scripts.

routine	arguments	comments
`integrate`	⟨scheme⟩	Can either be "`verlet`" or "vverlet" (velocity Verlet), implemented following Frenkel & Smit [90].
	⟨group id⟩	*Optional.* If not specified, assumes group ID "0" (all atoms). Useful to omit "wall" atoms from integration.
`build_nblist`	⟨interval⟩	# steps between building neighbor lists ("Verlet lists" [90]).
	⟨radius⟩	Distance inside which to track neighbors.
`barostat`	⟨target p⟩	Target pressure for Berendsen barostat [141] in $\mathrm{N\,m}^{-(d-1)}$.
	⟨compressibility⟩	Approximate system compressibility in $\mathrm{N\,m}^{-(d-1)}$.
	⟨time constant⟩	Time constant for pressure control in time units.
`heat_flux`	⟨group id⟩	Group of atoms to affect.
	⟨energy/time⟩	Heat current to add using scheme of Jund and Jullien [116]. Can be negative to remove heat current.
`temp_profile`	⟨dimension⟩	Can be "`1`", "`2`", or "`3`" (x, y, or z): the dimension along which to scan temperatures
	⟨# of bins⟩	Integer # of bins to spatially discretize in the given dimension
	⟨sample interval⟩	# steps between sampling the temperature in each bin
	⟨write interval⟩	# steps between writing the average and standard deviation of temperature in each bin, calculated over past samples. Data are written to ⟨`jobname`⟩`.profile`.
`write_macro`	⟨interval⟩	# steps between writing system-wide data to ⟨`jobname`⟩`.log`.
`write_micro`	⟨interval⟩	# steps between writing atomic data to ⟨`step`⟩`.micro`. Anticipate large file sizes!
`write_lammps`	⟨interval⟩	# steps between writing atomic data to ⟨`step`⟩`.lammpstrj`, readable by VMD (`http://www.ks.uiuc.edu/Research/vmd/`). Anticipate large file sizes!
`write_cfg`	⟨interval⟩	# steps between writing atomic data to ⟨`step`⟩`.cfg`, readable by Atomeye (`http://li.mit.edu/Archive/Graphics/A/`). Anticipate large file sizes!

A.3 A closer look

This section takes a quick glance under the hood, which will hopefully facilitate future revisions by myself and others.

A.3.1 Overview

The code consists of seven parts:

`main`	Main program control.
`common`	Global constants. `Sim` data structure.
`read_script`	Reads ⟨`jobname`⟩`.script`.
`routine`	Initializes `routine`s on setup, and executes them during simulations.
`md`	Runs the actual MD simulations.
`forces`	Calculates interatomic forces.
`cleanup`	Wraps up the job; e.g., prints timing info.

The file `common.h` defines a type of data structure called a `Sim`. At the beginning of a job, `main.c` creates an instance `s` of this structure; at any given moment during execution, `s` contains all of the information about the job. For example, `s->N` is the integer number of atoms in the simulation domain, `s->sim_dim` is the number of dimensions spanned by the domain, and `s->atom_r[i][d]` is the current position of the atom with index `i`, projected onto dimension `d` ($0 \to x$, $1 \to y$, etc.). Likewise, `s->atom_v[][]` contains current velocities.

A.3.2 Common revisions and how to make them

For some common types of features to add, here are some corresponding checklists of necessary changes to the code. Good luck.

If you want to…	Then…
Increase max numbers of things (atoms, types, line length, etc.)	• `common.h`: change corresponding global variables
Add a new potential	• `common.h`: add global constants to define a new `POT_STYLE_NAME_*` and `POT_STYLE_ID_*` • `read_script.c`: in `read_script()`, add appropriate entries for the `pot_style` and `pot_params` keywords • `forces.c`: in `forces()`, add the appropriate case to the switch on `pot_style_id`
Add a new routine	• `routine.h`: add new constant `ROUTINE_ID_*` • `routine.c`: add case to `routine_setup()`, and add case to `routine_run()` • `common.h`: add any necessary variable declarations to `Sim_def` • `common.c`: initialize variables
Add a new unit system	• `common.h`: add any necessary conversion factors and physical constants (see below) • `read_script.c`: add case for the `sim_units` keyword • `read_script.c`: if E units are inconsistent with $M\,L^2\,T^{-2}$, then convert any `pot_params` that include energy units (search for `!strcmp(s->units, "aap")` for an example) • `routine.c`: in `routine_run()`, add conversions/calculations to `BAROSTAT`, `HEAT_FLUX`, `TEMP_PROFILE`, `WRITE_MACRO`, `WRITE_MICRO`, and `WRITE_CFG`

Bibliography

[1] J. Tyndall, *Heat: A Mode of Motion* (Longmans, Green, and Co., London, 1868).

[2] U. K. Mishra, P. Parikh, and Y.-F. Wu, "AlGaN/GaN HEMTs—an overview of device operation and applications", *Proceedings of the IEEE* **90**, 1022 (2002).

[3] U. K. Mishra, L. Shen, T. E. Kazior, and Y.-F. Wu, "GaN-based RF power devices and amplifiers", *Proceedings of the IEEE* **96**, 287 (2008).

[4] A. Sarua, H. Ji, K. P. Hilton, D. J. Wallis, M. J. Uren, T. Martin, and M. Kuball, "Thermal boundary resistance between GaN and substrate in AlGaN/GaN electronic devices", *IEEE Transactions on Electron Devices* **54**, 3152 (2007).

[5] J. Kuzmík, S. Bychikhin, D. Pogany, C. Gaquière, E. Pichonat, and E. Morvan, "Investigation of the thermal boundary resistance at the III-nitride/substrate interface using optical methods", *Journal of Applied Physics* **101**, 054508 (2007).

[6] E. Pop, "Energy dissipation and transport in nanoscale devices", *Nano Research* **3**, 147 (2010).

[7] B. S. Williams, "Terahertz quantum-cascade lasers", *Nature Photonics* **1**, 517 (2007).

[8] C. J. Vineis, A. Shakouri, A. Majumdar, and M. G. Kanatzidis, "Nanostructured thermoelectrics: Big efficiency gains from small features", *Advanced Materials* **22**, 3970 (2010).

[9] H. P. Wong, S. Raoux, S. Kim, J. Liang, J. P. Reifenberg, B. Rajendran, M. Asheghi, and K. E. Goodson, "Phase change memory", *Proceedings of the IEEE* **98**, 2201 (2010).

[10] M. H. Kryder, E. C. Gage, T. W. McDaniel, W. A. Challener, R. E. Rottmayer, G. Ju, Y.-T. Hsia, and M. F. Erden, "Heat assisted magnetic recording", *Proceedings of the IEEE* **96**, 1810 (2008).

[11] A. J. Minnich, J. A. Johnson, A. J. Schmidt, K. Esfarjani, M. S. Dresselhaus, K. A. Nelson, and G. Chen, "Thermal conductivity spectroscopy technique to measure phonon mean free paths", *Physical Review Letters* **107**, 095901 (2011).

[12] P. E. Hopkins, "Thermal transport across solid interfaces with nanoscale imperfections", *ISRN Mechanical Engineering* **2013**, 682586 (2013).

[13] P. L. Kapitza, in *Collected Papers of Kapitza*, edited by D. Haar (Pergamon Press, London, 1965), vol. 2, pp. 581–624, originally published in *J. Phys. USSR* **1**, 181 (1941) and *Zhurnal Eksperimental'noi i Teoreticheskoi Fiziki* **11**, 581 (1941).

[14] I. M. Khalatnikov, "Teploobmen meždu tverdym telom i geliem II (heat transfer between a solid and helium II)", *Zhurnal Eksperimental'noi i Teoreticheskoi Fiziki* **22**, 687 (1952).

[15] G. L. Pollack, "Kapitza resistance", *Reviews of Modern Physics* **41**, 48 (1969).

[16] N. S. Snyder, "Heat transport through helium II: Kapitza conductance", *Cryogenics* **10**, 89 (1970).

[17] J. K. Hulm, "The thermal conductivity of tin, mercury, indium and tantalum at liquid helium temperatures", *Proceedings of the Royal Society of London A* **471**, 98 (1950).

[18] B. B. Goodman, "The thermal conductivity of superconducting tin below 1° K", *Proceedings of the Physical Society A* **66**, 217 (1953).

[19] W. A. Little, "The transport of heat between dissimilar solids at low temperatures", *Canadian Journal of Physics* **37**, 334 (1959).

[20] D. A. Neeper and J. R. Dillinger, "Thermal resistance at indium–sapphire boundaries between 1.1 and 2.1 °K", *Physical Review* **135**, A1028 (1964).

[21] J. T. Folinsbee and A. C. Anderson, "Anomalous Kapitza resistance to solid helium", *Physical Review Letters* **31**, 1580 (1973).

[22] R. E. Peterson and A. C. Anderson, "The transport of heat between solids at low temperature", *Solid State Communications* **10**, 891 (1972).

[23] R. E. Peterson and A. C. Anderson, "The Kapitza thermal boundary resistance", *Journal of Low Temperature Physics* **11**, 639 (1973).

[24] S. G. O'Hara and A. C. Anderson, "Thermal impedance across metallic and superconducting foils below 1 K", *Journal of Physics and Chemistry of Solids* **35**, 1677 (1974).

[25] M. E. Lumpkin, W. M. Saslow, and W. M. Visscher, "One-dimensional Kapitza conductance: Comparison of the phonon mismatch theory with computer experiments", *Physical Review B* **17**, 4295 (1978).

[26] S. Simons, "On the thermal contact resistance between insulators", *Journal of Physics C: Solid State Physics* **7**, 4048 (1974).

[27] Y. Ge, S. Chen, and W. Kuan, "Effect of anharmonicity on Kapitza resistance", *Journal of Low Temperature Physics* **75**, 59 (1989).

[28] W. M. Saslow and M. E. Lumpkin, “Interfacial three-phonon processes and anomalous interfacial energy transport”, *Solid State Communications* **29**, 395 (1979).

[29] M. E. Lumpkin and W. M. Saslow, “Interfacial three-phonon processes: Application to pulse experiments and the Kapitza conductance”, *Physical Review B* **20**, 1035 (1979).

[30] J. A. Katerberg, C. L. Reynolds, Jr., and A. C. Anderson, “Calculations of the thermal boundary resistance”, *Physical Review B* **16**, 673 (1977).

[31] C.-J. Guo and H. J. Maris, “Reflection of phonons at an interface between a solid and liquid helium”, *Physical Review Letters* **29**, 855 (1972).

[32] J. S. Buechner and H. J. Maris, “Reflection of phonons at interfaces between silicon and solid hydrogen and deuterium”, *Physical Review Letters* **34**, 316 (1975).

[33] A. Danowitz, K. Kelley, J. Mao, J. P. Stevenson, and M. Horowitz, “CPU DB: recording microprocessor history”, *Communications of the ACM* **55**, 55 (2012).

[34] E. T. Swartz and R. O. Pohl, “Thermal resistance at interfaces”, *Applied Physics Letters* **51**, 2200 (1987).

[35] E. T. Swartz and R. O. Pohl, “Thermal boundary resistance”, *Reviews of Modern Physics* **61**, 605 (1989).

[36] D. A. Young and H. J. Maris, “Lattice-dynamical calculation of the Kapitza resistance between fcc lattices”, *Physical Review B* **40**, 3685 (1989).

[37] S. Pettersson and G. D. Mahan, “Theory of the thermal boundary resistance between dissimilar lattices”, *Physical Review B* **42**, 7386 (1990).

[38] R. J. Stoner, H. J. Maris, T. R. Anthony, and W. F. Banholzer, “Measurements of the Kapitza conductance between diamond and several metals”, *Physical Review Letters* **68**, 1563 (1992).

[39] R. J. Stoner and H. J. Maris, “Kapitza conductance and heat flow between solids at temperatures from 50 to 300 K”, *Physical Review B* **48**, 16373 (1993).

[40] N. W. Ashcroft and N. D. Mermin, *Solid State Physics* (Brooks/Cole, Belmont, CA, 1976).

[41] P. Reddy, K. Castelino, and A. Majumdar, “Diffuse mismatch model of thermal boundary conductance using exact phonon dispersion”, *Applied Physics Letters* **87**, 211908 (2005).

[42] J. C. Duda, T. E. Beechem, J. L. Smoyer, P. M. Norris, and P. E. Hopkins, “Role of dispersion on phononic thermal boundary conductance”, *Journal of Applied Physics* **108**, 073515 (2010).

[43] G. Chen, “Thermal conductivity and ballistic-phonon transport in the cross-plane direction of superlattices”, *Physical Review B* **57**, 14958 (1998).

[44] M. Kazan, “Interpolation between the acoustic mismatch model and the diffuse mismatch model for the interface thermal conductance: Application to InN/GaN superlattices”, *Journal of Heat Transfer* **133**, 112401 (2011).

[45] P. E. Phelan, Y. Song, O. Nakabeppu, K. Ito, K. Hijikata, T. Ohmori, and K. Torikoshi, “Film/substrate thermal boundary resistance for an Er–Ba–Cu–O high-T_c thin film”, *Journal of Heat Transfer* **116**, 1038 (1994).

[46] K. E. Goodson, O. W. Käding, M. Rösler, and R. Zachai, “Experimental investigation of thermal conduction normal to diamond–silicon boundaries”, *Journal of Applied Physics* **77**, 1385 (1995).

[47] S.-M. Lee and D. G. Cahill, “Influence of interface thermal conductance on the apparent thermal conductivity of thin films”, *Microscale Thermophysical Engineering* **1**, 47 (1997).

[48] D. Cahill, A. Bullen, and S.-M. Lee, “Interface thermal conductance and the thermal conductivity of multilayer thin films”, *High Temperatures - High Pressures* **32**, 135 (2000).

[49] R. M. Costescu, M. A. Wall, and D. G. Cahill, “Thermal conductance of epitaxial interfaces”, *Physical Review B* **67**, 054302 (2003).

[50] R. J. Stevens, A. N. Smith, and P. M. Norris, “Measurement of thermal boundary conductance of a series of metal–dielectric interfaces by the transient thermoreflectance technique”, *Journal of Heat Transfer* **127**, 315 (2005).

[51] P. E. Hopkins and P. M. Norris, “Thermal boundary conductance response to a change in Cr/Si interfacial properties”, *Applied Physics Letters* **89**, 131909 (2006).

[52] P. E. Hopkins, R. N. Salaway, R. J. Stevens, and P. M. Norris, “Temperature-dependent thermal boundary conductance at Al/Al_2O_3 and Pt/Al_2O_3 interfaces”, *International Journal of Thermophysics* **28**, 947 (2007).

[53] P. E. Hopkins, P. M. Norris, and R. J. Stevens, “Influence of inelastic scattering at metal-dielectric interfaces”, *Journal of Heat Transfer* **130**, 022401 (2008).

[54] P. E. Hopkins, P. M. Norris, R. J. Stevens, T. E. Beechem, and S. Graham, “Influence of interfacial mixing on thermal boundary conductance across a chromium/silicon interface”, *Journal of Heat Transfer* **130**, 062402 (2008).

[55] P. E. Hopkins, J. C. Duda, S. P. Clark, C. P. Hains, T. J. Rotter, L. M. Phinney, and G. Balakrishnan, “Effect of dislocation density on thermal boundary conductance across GaSb/GaAs interfaces”, *Applied Physics Letters* **98**, 161913 (2011).

[56] P. E. Hopkins, J. C. Duda, C. W. Petz, and J. A. Floro, "Controlling thermal conductance through quantum dot roughening at interfaces", *Physical Review B* **84**, 035438 (2011).

[57] J. C. Duda and P. E. Hopkins, "Systematically controlling Kapitza conductance via chemical etching", *Applied Physics Letters* **100**, 111602 (2012).

[58] C. S. Gorham, K. Hattar, R. Cheaito, J. C. Duda, J. T. Gaskins, T. E. Beechem, J. F. Ihlefeld, L. B. Biedermann, E. S. Piekos, D. L. Medlin, et al., "Ion irradiation of the native oxide/silicon surface increases the thermal boundary conductance across aluminum/silicon interfaces", *Physical Review B* **90**, 024301 (2014).

[59] R. S. Prasher and P. E. Phelan, "A scattering-mediated acoustic mismatch model for the prediction of thermal boundary resistance", *Journal of Heat Transfer* **123**, 105 (2001).

[60] T. Beechem, S. Graham, P. E. Hopkins, and P. M. Norris, "Role of interface disorder on thermal boundary conductance using a virtual crystal approach", *Applied Physics Letters* **90**, 054104 (2007).

[61] T. Beechem and P. E. Hopkins, "Predictions of thermal boundary conductance for systems of disordered solids and interfaces", *Journal of Applied Physics* **106**, 124301 (2009).

[62] A. Maiti, G. D. Mahan, and S. T. Pantelides, "Dynamical simulations of nonequilibrium processes — Heat flow and the Kapitza resistance across grain boundaries", *Solid State Communications* **102**, 517 (1997).

[63] P. K. Schelling, S. R. Phillpot, and P. Keblinski, "Kapitza conductance and phonon scattering at grain boundaries by simulation", *Journal of Applied Physics* **95**, 6082 (2004).

[64] C. Kimmer, S. Aubry, A. Skye, and P. K. Schelling, "Scattering of phonons from a high-energy grain boundary in silicon: Dependence on angle of incidence", *Physical Review B* **75**, 144105 (2007).

[65] X. W. Zhou, R. E. Jones, C. J. Kimmer, J. C. Duda, and P. E. Hopkins, "Relationship of thermal boundary conductance to structure from an analytical model plus molecular dynamics simulations", *Physical Review B* **87**, 094303 (2013).

[66] S. Merabia and K. Termentzidis, "Thermal boundary conductance across rough interfaces probed by molecular dynamics", *Physical Review B* **89**, 054309 (2014).

[67] H. K. Lyeo and D. G. Cahill, "Thermal conductance of interfaces between highly dissimilar materials", *Physical Review B* **73**, 144301 (2006).

[68] G. T. Hohensee, R. B. Wilson, and D. G. Cahill, "Thermal conductance of metal–diamond interfaces at high pressure", *Nature Communications* **6**, 6578 (2015).

[69] M. L. Huberman and A. W. Overhauser, “Electronic Kapitza conductance at a diamond–Pb interface”, *Physical Review B* **50**, 2865 (1994).

[70] A. V. Sergeev, “Electronic Kapitza conductance due to inelastic electron-boundary scattering”, *Physical Review B* **58**, R10199 (1998).

[71] A. Majumdar and P. Reddy, “Role of electron–phonon coupling in thermal conductance of metal–nonmetal interfaces”, *Applied Physics Letters* **84**, 4768 (2004).

[72] G. D. Mahan, “Kapitza thermal resistance between a metal and a nonmetal”, *Physical Review B* **79**, 075408 (2009).

[73] G. Chen, “Diffusion–transmission interface condition for electron and phonon transport”, *Applied Physics Letters* **82**, 991 (2003).

[74] S. Aubry, C. J. Kimmer, A. Skye, and P. K. Schelling, “Comparison of theoretical and simulation-based predictions of grain-boundary Kapitza conductance in silicon”, *Physical Review B* **78**, 064112 (2008).

[75] E. S. Landry and A. J. H. McGaughey, “Thermal boundary resistance predictions from molecular dynamics simulations and theoretical calculations”, *Physical Review B* **80**, 165304 (2009).

[76] Y. A. Kosevich, “Fluctuation subharmonic and multiharmonic phonon transmission and Kapitza conductance between crystals with very different vibrational spectra”, *Physical Review B* **52**, 1017 (1995).

[77] P. E. Hopkins and P. M. Norris, “Effects of joint vibrational states on thermal boundary conductance”, *Nanoscale and Microscale Thermophysical Engineering* **11**, 247 (2007).

[78] P. E. Hopkins, “Multiple phonon processes contributing to inelastic scattering during thermal boundary conductance at solid interfaces”, *Journal of Applied Physics* **106**, 013528 (2009).

[79] J. C. Duda, P. E. Hopkins, J. L. Smoyer, M. L. Bauer, T. S. English, C. B. Saltonstall, and P. M. Norris, “On the assumption of detailed balance in prediction of diffusive transmission probability during interfacial transport”, *Nanoscale and Microscale Thermophysical Engineering* **14**, 21 (2010).

[80] P. E. Hopkins, J. C. Duda, and P. M. Norris, “Anharmonic phonon interactions at interfaces and contributions to thermal boundary conductance”, *Journal of Heat Transfer* **133**, 062401 (2011).

[81] J. C. Duda, P. M. Norris, and P. E. Hopkins, “On the linear temperature dependence of phonon thermal boundary conductance in the classical limit”, *Journal of Heat Transfer* **133**, 074501 (2011).

[82] R. J. Stevens, L. V. Zhigilei, and P. M. Norris, "Effects of temperature and disorder on thermal boundary conductance at solid–solid interfaces: Nonequilibrium molecular dynamics simulations", *International Journal of Heat and Mass Transfer* **50**, 3977 (2007).

[83] X. Wu and T. Luo, "The importance of anharmonicity in thermal transport across solid–solid interfaces", *Journal of Applied Physics* **115**, 014901 (2014).

[84] T. Murakami, T. Hori, T. Shiga, and J. Shiomi, "Probing and tuning inelastic phonon conductance across finite-thickness interface", *Applied Physics Express* **7**, 121801 (2014).

[85] K. Sääskilahti, J. Oksanen, J. Tulkki, and S. Volz, "Role of anharmonic phonon scattering in the spectrally decomposed thermal conductance at planar interfaces", *Physical Review B* **90**, 134312 (2014).

[86] D. S. Sholl and J. A. Steckel, *Density Functional Theory: A Practical Introduction* (Wiley, 2009).

[87] J. E. Jones, "On the determination of molecular fields. II. From the equation of state of a gas", *Proceedings of the Royal Society of London A* **106**, 463 (1924).

[88] F. H. Stillinger and T. A. Weber, "Computer simulation of local order in condensed phases of silicon", *Physical Review B* **31**, 5262 (1985).

[89] Y. Wang, X. Ruan, and A. K. Roy, "Two-temperature nonequilibrium molecular dynamics simulation of thermal transport across metal-nonmetal interfaces", *Physical Review B* **85**, 205311 (2012).

[90] D. Frenkel and B. Smit, *Understanding Molecular Simulation: From Algorithms to Applications* (Academic Press, 1996).

[91] M. J. Louwerse and E. J. Baerends, "Calculation of pressure in case of periodic boundary conditions", *Chemical Physics Letters* **421**, 138 (2006).

[92] M. Born and T. von Kármán, "Über Schwingungen in Raumgittern", *Physikalische Zeitschrift* **13**, 297 (1912).

[93] M. T. Dove, *Introduction to Lattice Dynamics*, no. 4 in Cambridge Topics in Mineral Physics and Chemistry (Cambridge University Press, Cambridge, England, 1993).

[94] J. D. Gale, "GULP: A computer program for the symmetry-adapted simulation of solids", *Journal of the Chemical Society, Faraday Transactions* **93**, 629 (1997).

[95] R. P. Feynman, "Simulating physics with computers", *International Journal of Theoretical Physics* **21**, 467 (1982).

[96] J. Parker, D. W. Feldman, and M. Ashkin, "Raman scattering by silicon and germanium", *Physical Review* **155**, 712 (1967).

[97] J. Zi, X. Wan, G. Wei, K. Zhang, and X. Xie, "Lattice dynamics of zinc-blende GaN and AlN: I. Bulk phonons", *Journal of Physics: Condensed Matter* **8**, 6323 (1996).

[98] J. M. Ziman, *Electrons and Phonons* (Oxford University Press, 1960).

[99] A. Majumdar, "Microscale heat conduction in dielectric thin films", *Journal of Heat Transfer* **115**, 7 (1993).

[100] G. Chen, *Nanoscale Energy Transport and Conversion: A Parallel Treatment of Electrons, Molecules, Phonons, and Photons* (Oxford University Press, New York, NY, 2005).

[101] A. J. H. McGaughey and M. Kaviany, "Quantitative validation of the Boltzmann transport equation phonon thermal conductivity model under the single-mode relaxation time approximation", *Physical Review B* **69**, 094303 (2004).

[102] A. J. Minnich, "Advances in the measurement and computation of thermal phonon transport properties", *Journal of Physics: Condensed Matter* **27**, 053202 (2015).

[103] A. Ward, D. A. Broido, D. A. Stewart, and G. Deinzer, "*Ab initio* theory of the lattice thermal conductivity in diamond", *Physical Review B* **80**, 125203 (2009).

[104] A. Ward and D. A. Broido, "Intrinsic phonon relaxation times from first-principles studies of the thermal conductivities of Si and Ge", *Physical Review B* **81**, 085205 (2010).

[105] S. Sinha and K. E. Goodson, "Thermal conduction in sub-100 nm transistors", *Microelectronics Journal* **37**, 1148 (2006).

[106] K. C. Collins, A. A. Maznev, Z. Tian, K. Esfarjani, K. A. Nelson, and G. Chen, "Non-diffusive relaxation of a transient thermal grating analyzed with the Boltzmann transport equation", *Journal of Applied Physics* **114**, 104302 (2013).

[107] R. E. Peierls, in *Selected Scientific Papers of Sir Rudolf Peierls*, edited by R. H. Dalitz and R. E. Peierls (Imperial College Press, London, 1997), vol. 19 of *World Scientific Series in 20th Century Physics*, pp. 15–49, originally published in *Ann. d. Physik* **3**, 1055–1101 (1929).

[108] L. Lindsay, D. A. Broido, and N. Mingo, "Lattice thermal conductivity of single-walled carbon nanotubes: Beyond the relaxation time approximation and phonon-phonon scattering selection rules", *Physical Review B* **80**, 125407 (2009).

[109] K. Gordiz and A. Henry, "A new formalism for calculating modal contributions to thermal interface conductance from molecular dynamics simulations", *arXiv* (2014), article 1407.6410, URL `http://arxiv.org/abs/1407.6410`.

[110] R. S. Prasher, X. J. Hu, Y. Chalopin, N. Mingo, K. Lofgreen, S. Volz, F. Cleri, and P. Keblinski, "Turning carbon nanotubes from exceptional heat conductors into insulators", *Physical Review Letters* **102**, 105901 (2009).

[111] B. A. Auld, *Acoustic Fields and Waves in Solids* (John Wiley & Sons, New York, NY, 1973).

[112] T. S. English, J. C. Duda, J. L. Smoyer, D. A. Jordan, P. M. Norris, and L. V. Zhigilei, "Enhancing and tuning phonon transport at vibrationally mismatched solid–solid interfaces", *Physical Review B* **85**, 035438 (2012).

[113] O. G. Peterson, D. N. Batchelder, and R. O. Simmons, "Measurements of X-ray lattice constant, thermal expansivity, and isothermal compressibility of argon crystals", *Physical Review* **150**, 703 (1966).

[114] D. N. Batchelder, M. F. Collins, B. C. G. Haywood, and G. R. Sidey, "Lattice dynamics of argon at 4 degrees K", *Journal of Physics C: Solid State Physics* **3**, 249 (1970).

[115] H. Ness, L. Stella, C. D. Lorenz, and L. Kantorovich, "Applications of the generalized Langevin equation: Towards a realistic description of the baths", *Physical Review B* **91**, 014301 (2015).

[116] P. Jund and R. Jullien, "Molecular-dynamics calculation of the thermal conductivity of vitreous silica", *Physical Review B* **59**, 13707 (1999).

[117] P. K. Schelling, S. R. Phillpot, and P. Keblinski, "Phonon wave-packet dynamics at semiconductor interfaces by molecular-dynamics simulation", *Applied Physics Letters* **80**, 2484 (2002).

[118] Z. Wei, Y. Chen, and C. Dames, "Wave packet simulations of phonon boundary scattering at graphene edges", *Journal of Applied Physics* **112**, 024328 (2012).

[119] B. Deng, A. Chernatynskiy, M. Khafizov, D. H. Hurley, and S. R. Phillpot, "Kapitza resistance of Si/SiO$_2$ interface", *Journal of Applied Physics* **115**, 084910 (2014).

[120] C. B. Saltonstall, C. A. Polanco, J. C. Duda, A. W. Ghosh, P. M. Norris, and P. E. Hopkins, "Effect of interface adhesion and impurity mass on phonon transport at atomic junctions", *Journal of Applied Physics* **113**, 013516 (2013).

[121] C. H. Baker, D. A. Jordan, and P. M. Norris, "Application of the wavelet transform to nanoscale thermal transport", *Physical Review B* **86**, 104306 (2012).

[122] C. H. Baker, Ph.D. thesis, University of Virginia (2015).

[123] A. J. H. McGaughey and J. M. Larkin, "Predicting phonon properties from equilibrium molecular dynamics simulations", *Annual Review of Heat Transfer* **17**, 49 (2014).

[124] J. M. Larkin, Ph.D. thesis, Carnegie Mellon University (2013).

[125] E. Fermi, J. Pasta, and S. Ulam, Tech. Rep. LA-1940, Los Alamos (1955).

[126] D. N. Payton, III, M. Rich, and W. M. Visscher, "Lattice thermal conductivity in disordered harmonic and anharmonic crystal models", *Physical Review* **160**, 706 (1967).

[127] M. Bishop, M. Derosa, and J. Lalli, "Molecular dynamics simulations of one-dimensional Lennard-Jones systems", *Journal of Statistical Physics* **25**, 229 (1981).

[128] S. G. and D. Kumar, "Universality classes for phonon relaxation and thermal conduction in one-dimensional vibrational systems", *Physical Review E* **84**, 041119 (2011).

[129] G. P. Berman and F. M. Izrailev, "The Fermi–Pasta–Ulam problem: Fifty years of progress", *Chaos* **15**, 015104 (2005).

[130] N. Li and B. Li, "Thermal conductivities of one-dimensional anharmonic/nonlinear lattices: renormalized phonons and effective phonon theory", *AIP Advances* **2**, 041408 (2012).

[131] T. Meier, F. Menges, P. Nirmalraj, H. Hölscher, H. Riel, and B. Gotsmann, "Length-dependent thermal transport along molecular chains", *Physical Review Letters* **113**, 060801 (2014).

[132] J. Callaway, "Model for lattice thermal conductivity at low temperatures", *Physical Review* **113**, 1046 (1959).

[133] M. G. Holland, "Analysis of lattice thermal conductivity", *Physical Review* **132**, 2461 (1963).

[134] Z. Liang, K. Sasikumar, and P. Keblinski, "Thermal transport across a substrate–thin-film interface: Effects of film thickness and surface roughness", *Physical Review Letters* **113**, 065901 (2014).

[135] Z. Liang and P. Keblinski, "Finite-size effects on molecular dynamics interfacial thermal-resistance predictions", *Physical Review B* **90**, 075411 (2014).

[136] L. Carroll, *Sylvie and Bruno Concluded* (Macmillan and Co., London, 1893), p. 169.

[137] J. C. Duda, T. S. English, E. S. Piekos, W. A. Soffa, L. V. Zhigilei, and P. E. Hopkins, "Implications of cross-species interactions on the temperature dependence of Kapitza conductance", *Physical Review B* **84**, 193301 (2011).

[138] Z. Tian, K. Esfarjani, and G. Chen, "Enhancing phonon transmission across a Si/Ge interface by atomic roughness: First-principles study with the Green's function method", *Physical Review B* **86**, 235304 (2012).

[139] J. C. Duda, T. S. English, D. A. Jordan, P. M. Norris, and W. A. Soffa, "Controlling thermal conductivity of alloys via atomic ordering", *Journal of Heat Transfer* **134**, 014501 (2012).

[140] P. M. Norris, N. Q. Le, and C. H. Baker, "Tuning phonon transport: From interfaces to nanostructures", *Journal of Heat Transfer* **135**, 061604 (2013).

[141] H. J. C. Berendsen, J. P. M. Postma, W. F. van Gunsteren, A. DiNola, and J. R. Haak, “Molecular dynamics with coupling to an external bath”, *Journal of Chemical Physics* **81**, 3684 (1984).